# Interferons shape the interface between macrophages and *Mycobacterium tuberculosis*: lessons from latency and metabolic mechanisms

Gregory S. Olson

A dissertation

submitted in partial fulfillment of the

requirements for the degree of

Doctor of Philosophy

University of Washington

2021

Reading Committee:

Alan Aderem, Chair

Thomas Hawn

John Aitchison

Program Authorized to Offer Degree:

Molecular and Cellular Biology

University of Washington

# Abstract

## Interferons shape the interface between macrophages and *Mycobacterium tuberculosis*: lessons from latency and metabolic mechanisms

Gregory S. Olson

Chair of the Supervisory Committee:
Alan Aderem
Department of Immunology

Humans and *Mycobacterium tuberculosis* (Mtb) have been co-evolving for tens of thousands of years. Although Mtb remains the deadliest bacterial infection globally, most exposed individuals control the infection either through clearance or containment and never develop disease. While a quarter of the entire human population has been exposed to Mtb, how a contained Mtb infection (CMTB) alters the biology of the host remains poorly understood. The beginning of this dissertation investigates how CMTB alters immune responses in a mouse model. CMTB rapidly and durably reduces tuberculosis disease burden after re-exposure through aerosol challenge and also protects against heterologous challenges with *Listeria monocytogenes* or metastatic melanoma. Protection is associated with activation of alveolar macrophages, the first cells that respond to inhaled Mtb, and accelerated recruitment of Mtb-specific T cells to the lung parenchyma. RNA sequencing, *ex vivo* functional assays, and *in vivo* infections demonstrate that CMTB reconfigures tissue resident alveolar macrophages via exposure to low-grade interferon γ, a type II interferon (IFN). These studies demonstrate that under certain circumstances, the continuous interaction of the immune system with Mtb is beneficial to the host by maintaining elevated innate immune responses.

To better understand the molecular interface between macrophages and Mtb, we turn to a more tractable *in vitro* model of Mtb infection. Metabolic reprogramming powers and polarizes macrophage functions, but the nature and regulation of this response during infection with pathogens remain controversial. We characterize the metabolic and transcriptional responses of murine macrophages to Mtb in order to disentangle the underlying mechanisms. We find that type I IFN signaling correlates with the decreased glycolysis and mitochondrial damage that is induced by live, but not killed, Mtb. Macrophages lacking the type I IFN receptor maintain glycolytic flux and mitochondrial function during Mtb infection *in vitro* and, importantly, *in vivo*. IFNβ itself restrains the glycolytic shift of inflammatory macrophages and initiates mitochondrial stress. We confirm that type I IFN acts upstream of mitochondrial damage using macrophages lacking the protein STING. We suggest that a type I IFN – mitochondrial feedback loop controls macrophage responses to mycobacteria and that this could contribute to pathogenesis across a range of diseases.

Overall, this dissertation provides new insights into the interface between the immune system and Mtb at both the organismal and molecular scales. The evidence of beneficial effects of CMTB on organismal health raises many questions about how the immune system responds to contained or latent Mtb. We posit that extending the molecular mechanisms controlling the macrophage metabolic response described here will be a critical first step in addressing these questions.

# Table of Contents

## List of Figures

# List of Tables

# Acknowledgments and Dedication

I am indebted to many for the contents of this dissertation.

*First and foremost, I would like to dedicate this dissertation to the hundreds of mice that knew only cages and died at my hand or at my command for these pages to be written. The biomedical enterprise may rationalize their deaths as worthwhile in the pursuit of knowledge that might, sometime in the future, save human lives, but I doubt the mice would agree.*

I would also like to thank:

My parents, John and Melissa, and my brother, AJ, for instilling in me a deep wonder of the beauty of the natural world and the confidence and curiosity to constantly question it. For supporting me financially, emotionally, and intellectually along the way.

My research mentors over the years, including Dietmar Kappes, Rachel Altura, Sharon Swartz, Andrew Campbell, and Doug Kwon, for introducing me to the thrills of discovery and the drudgery of science. Doug, especially, for reigniting my passion for research and inspiring me to pursue the path of physician scientist. Maybe more importantly, for allowing me the intellectual freedom and unwavering support to make and learn from my own mistakes.

My PhD mentor, Alan Aderem, for creating an atmosphere of passionate science, for always being ready to defend vigorously the lab and its members, for teaching me the long history of science that has paved the way for this dissertation. For lending me the delicate early edition of Metchnikoff's writing for me to marvel over after the day's experiments were done.

My colleagues in the Aderem lab, for treating me like an equal from the beginning and providing a wonderful scientific home during this journey. Especially to Johannes Nemeth, for being the wrecking ball for barriers big and small, for dreaming up and discussing hundreds of projects with me daily, for reminding me of the importance of the patient. Johannes initiated the project described in Chapter II and led much of the effort. I thank him for allowing me to collaborate with him on this and present it in my dissertation, although it was most certainly a shared venture. Alissa Rothchild, for your encyclopedic knowledge of tuberculosis literature and dramatis personae, for your rigor and logic, for your willingness to help at all stages. Liz Gold, for seeing the heart of all scientific questions and proposing the best experiments to resolve them. Alan Diercks, for your critical insight on experimental plans, hairballs of numbers, data visualization, and computational fluency. Liz and Alan for being paragons of scientific writing and doing your

best to impart the skill to me. Ana for being a joy to share a bench with and for all the stories swapped during the interminable ABSL-3 sojourns. Vincent for welcoming me during my rotation. Dat for being the keystone of the entire lab and the well-timed glucose infusions in the form of café delicacies. Rudy for slogging the good slog with me. Tara for learning so quickly and being so eager to help. Irina for technical assistance. Drew for making it all run as smooth as silk.

The members of collaborating labs, especially Kevin Urdahl and lab members Jared, Sara, and Courtney for their *in vivo* tuberculosis expertise; Rong Tian and lab members Toni Hsu, Bo Zhou, Dennis Wang, and Mingyue Zhao for invaluable assistance in designing and interpreting metabolic assays. John Aitchison and lab members Fred Mast and Thurston Herricks for illuminating the secrets and practices of light microscopy.

My thesis committee, Alan Aderem, Tom Hawn, Rong Tian, John Aitchison, and Joshua Vaughan for scientific support and reminding me to come back out of the clouds and focus at many turns.

The directors and administrators of the UW MSTP and MCB programs for work both on the stage and behind the scenes.

The Office of Animal Care at the Center for Global Infectious Disease Research at Seattle Children's Research Institute, including especially Jessica Spaulding and Roberto Guirnalda for taking care of the mice. The University of Washington Immunohistochemistry core, especially Dr. Piper Treuting and Brian Johnson for histological services. The NIH Tetramer Core Facility (Contract HHSN272201300006C) for providing tetramers. Martina Sanlorenzo and Igor Vujic for help with the melanoma model. My sources of funding, especially the NIH NIAID and ARCS.

My classmates, especially but not exclusively Nick, Sanjay, and Jesse, for making the long hours of study and the longer hours of self-doubt not only tolerable but verging on enjoyable.

My parents-in-law, Cris and Sundee, for always being supportive and curious enough to ask about my research, even when all I wanted was to hide it under a bushel.

My partner, Natalie, for being my rock during the vicissitudes of research. And for everything you are.

My daughter, Ariane, for reminding me how full of wonder the world looks through new eyes.

# Chapter I: Introduction

Sections of text in this chapter have been modified slightly from the following manuscripts:

Nemeth, J., **Olson, G.S.,** Rothchild, A.C., Jahn, A.N., Mai, D., Duffy, F.J., Delahaye, J.L., Srivatsan, S., Plumlee, C.R., Urdahl, K.B., et al. (2020). Contained mycobacterium tuberculosis infection induces concomitant and heterologous protection. PLoS Pathog. *16*, e1008655

**Olson, G.S.,** Murray, A.M., Jahn, A.N., Mai, D., Diercks, A.H., Gold, E.S., Aderem, A. (2021). Type I interferon decreases macrophage energy metabolism during mycobacterial infection. *In preparation*.

## Host-microbe interactions

I am fascinated by the intricate interactions between humans and the teeming myriads of microbial life that lives within and around each and every one of us. The human immune system comprises a collection of physical barriers, chemical signals, humoral antibodies, and cellular networks that coordinates a shifting equilibrium between the host and these resident and visiting microbes. The failure to maintain this equilibrium causes disease, from damage dealt either by microbes directly or by an improperly activated immune system or both.

The current COVID-19 pandemic caused by the virus SARS-CoV-2 has provided a striking global example of the failure of the immune system to maintain organismal health. Our growing understanding of the factors involved in COVID-19 severity includes examples of both direct viral damage and immune-mediated pathology. This pandemic is certainly not the first we have faced nor will it be the last. We have been shaped by our relationships with microbes back through the millennia: by the dramatic explosion of a single disease through a population, by the chronic infections stably passed around for generations, by the colonizing beneficial bacterium, by the fleeting microbial encounters in forests, rivers, houses, farms. To understand ourselves

(and protect ourselves from the next dramatic explosion) we must understand the immune systems that are our microbial voice, our microbial ear, our olive branch, our spear.

The cellular components of the mammalian immune system have classically been classified as either “innate” or “adaptive”. The presence of a rearranged receptor that is highly specific for a very small set of molecular signatures characterizes the adaptive immune cells, named T and B cells. Innate immune cells are less neatly defined and are often characterized by their relatively quick responses to immunological insults and the lack of the highly specific rearranged receptors.

The modern era of the study of innate immune cells began when Elie Metchnikoff first described large, mobile cells that are quickly recruited to the site of tissue damage to engulf foreign material in a process called phagocytosis (Metchnikoff, 1893). These cells, termed macrophages, play critical roles in the immune systems of almost all animals, ranging from invertebrates to humans; macrophages recognize an immunological threat, phagocytose or endocytose the microbe or debris, degrade the internalized material, and orchestrate subsequent immune responses by secreting numerous potent signaling molecules, including cytokines and lipids (Aderem et al., 1986; Cohn, 1981; Gordon and Cohn, 1973; Ravetch and Aderem, 2007).

Charles Janeway revolutionized our understanding of the process of recognition of foreign material, hypothesizing the presence of germ-line encoded receptors that recognize classes of molecules, which he termed pattern recognition receptors (PRRs) (Janeway, 1989; Medzhitov, 2009). Although the Toll-like receptors (TLRs) were the first family of PRRs discovered (Lemaitre et al., 1996; Medzhitov et al., 1997; Poltorak et al., 1998), we now know that many different receptors monitor all cellular locations for a wide variety of molecular patterns.

This exquisite collection of receptors would be useless, however, if macrophages never encountered the problem in the first place. In fact, specific populations of macrophages reside in and monitor every tissue of the body. While the exact details of the ontogeny of these tissue-resident macrophages remain murky, these macrophages distribute throughout the body early during embryogenesis and maintain populations that can be stable for years to decades (Ginhoux and Guilliams, 2016). Each distinct tissue environment shapes the characteristics and functions of the resident macrophage population, creating distinct macrophage subsets throughout the body (Lavin et al., 2014).

After tissue-resident macrophages recognize certain threats within a tissue, they release potent signaling molecules that initiate an inflammatory response. One hallmark of this response is the recruitment of monocytes circulating in blood into the inflamed tissue (Shi and Pamer, 2011). Inflammatory signals within the tissue then push monocytes to differentiate into macrophage or dendritic cell populations, which often help to perpetuate the inflammatory response (Shi and Pamer, 2011).

## Metabolism controls macrophage activation

A growing body of evidence has underscored the functional importance of metabolic changes downstream of pattern recognition receptors or host cytokine receptors in controlling the inflammatory responses of macrophages (van Teijlingen Bakker and Pearce, 2020). Mammalian cells rely on two interconnected metabolic programs to generate energy for cellular functions: cytosolic glycolysis and mitochondrial oxidative phosphorylation (OXPHOS). Preferential reliance on glycolysis generates ATP rapidly, enables carbons in metabolic intermediates to be shunted to macromolecular biosynthesis, and leads to increased export of lactate—measuring the resulting extracellular acidification rate (ECAR) can quantify glycolytic flux (O'Neill et al., 2016) (and see Chapter III methods for further details). Mitochondrial metabolism fully oxidizes carbons and stores the energy in a mitochondrial membrane potential

($\Delta\psi_m$) that can be used to do work, for example in OXPHOS to efficiently generate ATP. This process requires electrons be passed to oxygen—measuring the resulting oxygen consumption rate (OCR) can quantify flux through the electron transport chain (ETC) (O'Neill et al., 2016) (and see Chapter III methods for further details). Low levels of mitochondrial reactive oxygen species (mROS) are an unavoidable byproduct of healthy mitochondrial metabolism as a small fraction of electrons escape the ETC. However, the accumulation of mROS, concomitant with decreased OCR and a dissipated $\Delta\psi_m$, is a hallmark of mitochondrial damage.

ROS, a class of diverse molecules including superoxide ($O_2^-$) and hydrogen peroxide ($H_2O_2$), helps control the balance between tolerance and inflammation across immune systems as divergent as insects and plants (Soto et al., 2009; Zug and Hammerstein, 2015). ROS serves many functions within a cell depending on amount and location. Low levels engage signaling pathways while sustained high levels result in cell death. The NADPH oxidase system and mitochondria produce the majority of intracellular ROS. The NADPH oxidase system concentrates ROS within the phagosome to directly kill bacteria, including Mtb (Deffert et al., 2014). mROS from the mitochondrial electron transport chain (ETC) and other oxidases was long thought to be merely a byproduct of mitochondrial metabolism, but recent research has highlighted that both its production and its function is specifically modulated in many cell types, including macophages. Indeed, mROS has emerged as a key signal transduction molecule downstream of specific receptors and upstream of both transcription factor activation and effector functions (Nathan and Cunningham-Bussel, 2013; Sena and Chandel, 2012; Shadel and Horvath, 2015).

Studies investigating the production of mROS in macrophages upon bacterial infection have broadly invoked two separate explanations: 1) host PRRs (e.g. toll-like receptors; TLRs) or cytokine receptors initiating signal transduction cascades that converge on the mitochondria (Chandel et al., 2001; Garaude et al., 2016; Geng et al., 2015; Roca and Ramakrishnan, 2013;

West et al., 2011) and 2) bacterial factors such as nutrient competition causing metabolic stress or secreted proteins directly interacting with the mitochondria (Lobet et al., 2015). A number of mycobacterial proteins have either been predicted (Moreno-Altamirano et al., 2012) or experimentally shown to localize to the host mitochondria (Cadieux et al., 2011; Duan et al., 2016; Sohn et al., 2011). Although increased mycobacterial virulence correlates with increased mitochondrial damage *in vitro* (Abarca-Rojano et al., 2003; Chen et al., 2006a; Jamwal et al., 2013) and a previous report demonstrated that different lineages of Mtb correlate with different levels of mROS in BMDM independent of bacterial burden (Wiens and Ernst, 2016), a mechanistic understanding of mROS generation during Mtb infection of macrophages remains elusive.

Many macrophage functions integral to Mtb immunity have been correlated with increased mROS levels. A previous study suggested that mROS contributes to direct bactericidal activity after mitochondria are physically recruited to phagosomes containing microbial ligands, but the effect on macrophage activation and other functions went unexplored (West et al., 2011). The consequence of mROS signaling depends on the context, ranging from promoting inflammation (e.g. stimulating inflammatory cytokine production (Bulua et al., 2011; Zhou et al., 2011) and skewing differentiation towards inflammatory subsets (Jin et al., 2014)) to inducing tolerance (e.g. limiting NF-κB activation upon administration of a pulmonary allergen (Khare et al., 2016)). In the setting of altered TNF signaling in the zebrafish model of *Mycobacteria marinum* infection, mROS augmented early bactericidal responses in macrophages, but also induced cell death pathways that increased mycobacterial burden at later time points (Roca and Ramakrishnan, 2013; Roca et al., 2019).

Macrophages differentially engage the central energy-generating pathways glycolysis and OXPHOS during activation to power and polarize subsequent immune responses. Studies using canonical immune stimuli support a model in which inflammatory macrophages rely on

glycolytic metabolism while reparative or tolerogenic macrophages rely on mitochondrial metabolism. For example, TLR4 recognition of lipopolysaccharide (LPS) skews macrophages toward aerobic glycolysis: an increased reliance on glycolytic ATP, a repurposing of the tricarboxylic acid cycle for anabolism, and $\Delta\psi_m$ hyperpolarization as OXPHOS decreases (Buck et al., 2017; Loftus and Finlay, 2016; Weinberg et al., 2015). Conversely, IL-4 (a cytokine involved in tissue repair) increases mitochondrial respiration and OXPHOS at the expense of glycolysis (O'Neill et al., 2016; Pearce and Pearce, 2013).

Not only does immune signaling alter metabolism, but metabolic distress also engages immune signaling. Mitochondria—as endosymbionts carrying vestiges of their bacterial past—release potent immunostimulatory molecules when damaged, including mROS (discussed above) and mitochondrial DNA (mtDNA). mtDNA released from damaged mitochondria activates the nucleic acid sensor cGAS which signals through the adaptor protein STING to induce robust expression of the type I interferon (IFN) family of cytokines (Mills et al., 2017; Weinberg et al., 2015).

Although studies with purified bacterial components support the simplified model that macrophages balance glycolysis and OXPHOS (i.e. when one increases, the other decreases), macrophage metabolism during infections with live pathogens displays much more complex patterns (Ayres, 2020; Eisenreich et al., 2019; Gleeson and Sheedy, 2016; Russell et al., 2019). The mechanisms driving these patterns remain largely uncharacterized, in part because the literature does not always agree on the metabolic responses to pathogens.

Many excellent reviews (Cumming et al., 2020; Howard and Khader, 2020; Sheedy and Divangahi, 2020) have highlighted one of the most pressing examples of these inconsistencies: macrophage infection with *Mycobacterium tuberculosis* (Mtb), arguably the single most important bacteria in human history.

## *Mycobacterium tuberculosis*

Humans have co-evolved with Mtb for at least 70,000 years (Comas et al., 2013). The disease caused by Mtb, Tuberculosis (TB), is estimated to have been responsible for one-fifth of all adult deaths in the western world between 1700 and 1900 (Wilson, 2005). Although many richer countries controlled TB mortality in the 20$^{th}$ century, TB remains the deadliest bacterial disease world-wide, with an estimated 10.0 million cases of active disease and 1.4 million deaths in 2019 (World Health Organization, 2020). The current vaccine, bacille Calmette-Guérin (BCG), provides incomplete protection against disease and transmission in adults and the current treatment regimens require months of multiple drugs with high rates of toxic side effects. These challenges, combined with the increasing prevalence of multi-drug resistant Mtb, has reinvigorated interest in new immunological interventions, whether these be new vaccines (Andersen and Kaufmann, 2014) or host-directed therapies (Hawn et al., 2013; Kaufmann et al., 2014).

Macrophage subsets not only coordinate the earliest immune responses after Mtb transmission but also serve as the preferred intracellular niche for Mtb replication. Mtb first encounters the immune system after an inhaled bacterium is phagocytosed by an alveolar macrophage (AM) (Cohen et al., 2018; North and Jung, 2004; Pai et al., 2016; Rothchild et al., 2019). These lung-resident AMs fail to control bacterial replication and are surprisingly non-reactive to the engulfed bacteria (Rothchild et al., 2019). As Mtb burden grows, AMs finally initiate the recruitment of inflammatory monocyte derived macrophages (MDMs) that more effectively control Mtb (Cohen et al., 2018; Huang et al., 2018; Rothchild et al., 2019).

In humans, the initial macrophage responses and subsequent immune mechanisms that protect against TB are evidently quite powerful: despite an extraordinarily high prevalence of *Mycobacterium tuberculosis* (Mtb) (some estimates suggest that at least 25% of the world's population has been exposed (Houben and Dodd, 2016)), the vast majority (~90%) of

individuals are able to contain and control the infection for their lifetimes with no clinical symptoms (Dutta and Karakousis, 2014; Hernández-Pando et al., 2000; Houben and Dodd, 2016; Lillebaek et al., 2002; Neyrolles et al., 2006; Pai et al., 2016; Wang, 1916), a state termed latent TB infection (LTBI). In fact, it is widely believed that the relationship between humans and Mtb encompasses a spectrum of states including bacterial clearance, persistence of live bacteria contained by the immune system, and sub-clinical and overt disease (Furin et al., 2019). Although the vast majority of Mtb infections do not result in overt disease, how these other states of infection impact the biology of the host remains unknown, partly due to limited small animal models for the full spectrum of Mtb-host interactions.

The failure to identify mechanisms or correlates of immunological protection against TB has hampered the development of vaccines or host-directed therapies to reduce the world-wide disease burden. Several inherent limitations restrict the ability to uncover the correlates of immune protection solely through human investigations: 1) Although natural immunity exists, it is difficult to definitively identify those who are protected. 2) Protective immunity is probably established in the first days to few weeks after aerosol Mtb exposure, but infected individuals are usually not identified until many weeks or months later. 3) Protective immune responses occur at tissue sites of infection which are generally inaccessible. 4) While correlates of protection can be identified, in vivo mechanistic dissection cannot be performed.

The mouse, then, continues to play an essential role as a model organism for the development of TB vaccine strategies due to the extensive availability of molecular reagents, a large body of historical data, and relatively low cost. Much of our current understanding of TB immunology had its origins in the mouse before subsequent validation in humans, for example the critical roles for CD4 T cells (Orme, 1988), IL-12 (Cooper et al., 1997), TNF (Flynn et al., 1995), and interferon γ (Cooper et al., 1993; Flynn et al., 1993).

## Interferons: critical coordinators of Mtb immune responses

The role of interferon γ in protection against TB, initially described in the mouse model (Cooper et al., 1993; Flynn et al., 1993), has been extended to human disease (Fortin et al., 2007; Jouanguy et al., 1999; Newport et al., 1996). In fact, the protective effects of IL-12 and CD4 T cells noted above seem to be mainly through the induction of interferon γ signaling (North and Jung, 2004). Despite the clear detrimental effects of loss of interferon γ signaling, how this cytokine actually mediates protection remains unclear.

The interferon (IFN) family of cytokines can be divided into 3 classes: type I, type II, and type III. Type III IFNs have only recently been described and their roles in TB pathogenesis are actively being investigated by many labs. IFNγ, the sole member of the type II IFN class, signals through the IFNγ receptor (IFNGR), a heterodimer encoded by the genes *Ifngr1* and *Ifngr2*. While IFNγ clearly protects against TB disease, the contributions of type I IFNs to immunity against Mtb remain controversial.

The type I IFN cytokines, including >10 IFNα members and the single IFNβ, signals through the receptor IFNAR to change the expression of hundreds of genes. This response is critical for eliciting an antiviral state, but how type I IFN regulates immune responses to intracellular bacterial pathogens (Decker et al., 2005), including Mtb (Moreira-Teixeira et al., 2018), remains contentious. For example, increasing type I IFN can increase the efficacy of vaccination against Mtb (Giacomini et al., 2009; Grode et al., 2005; Gröschel et al., 2017) while also exacerbating disease progression in animal models (Antonelli et al., 2010). In general, the consensus remains that type I IFNs are detrimental in anti-mycobacterial immunity, but how they impact the response of macrophages to Mtb remains largely uncharacterized.

## Objectives

The lack of insight into mechanisms or correlates of protection remains a major impediment to the design of vaccines or host-directed therapeutics for TB. This dissertation leverages the mouse as a tractable small animal model of Mtb infection in order to investigate the interface between macrophages and Mtb at both the organismal and molecular scales.

Chapter II reports a project to extend an established model of contained MTB infection (CMTB) to identify new mechanisms of protection. This chapter aims to 1) characterize the protection of the CMTB mouse model against secondary Mtb challenge and heterologous infections and 2) identify potential immunological mechanisms that mediate this protection. We hope that this characterization of a new model of protection will reinvigorate the search for immune correlates to advance vaccine development.

Although *in vivo* models of Mtb infection (like the one described in Chapter II) are critical for the understanding of TB pathogenesis, we do not understand enough about the fundamental interactions between macrophages and Mtb to take full advantage of such models. In particular, the literature on the metabolic response of macrophages to Mtb is highly contradictory. In order to disentangle the molecular events that control the macrophage response to Mtb, we employ an *in vitro* model of Mtb infection in murine bone marrow derived macrophages (BMDM). Chapter III seeks to not only resolve the inconsistencies around the nature of macrophage metabolism during Mtb infection but also identify the molecular mechanisms that explain them.

Surprisingly we identify type I IFN as the major modulator of macrophage metabolism during Mtb infection. Even more surprising is that we could not find in the literature a thorough description of how type I IFN affects macrophage energy metabolism. Chapter IV aims to characterize in macrophages the metabolic effects of IFNβ itself and define how IFNβ alters the well-characterized immunometabolic changes downstream of TLR ligation.

# Chapter II: Contained Mycobacterium tuberculosis infection induces concomitant and heterologous protection

As noted in the Acknowledgments, I would like to emphasize that this project was initiated by Johannes Nemeth and he contributed much to the work described here.

Sections of text in this chapter have been modified slightly from the following manuscript:

Nemeth, J., **Olson, G.S.,** Rothchild, A.C., Jahn, A.N., Mai, D., Duffy, F.J., Delahaye, J.L., Srivatsan, S., Plumlee, C.R., Urdahl, K.B., et al. (2020). Contained mycobacterium tuberculosis infection induces concomitant and heterologous protection. PLoS Pathog. *16*, e1008655

## Introduction

Both historical cohort studies and contemporary epidemiological studies demonstrate that prior *Mycobacterium tuberculosis* (Mtb) infection is protective against re-infection (Andrews et al., 2012; Blaser et al., 2016). In a non-human primate model, prior infection with Mtb conferred significant protection against aerosol challenge (Cadena et al., 2018). The phenomenon of a low-grade infection protecting against subsequent infections with the same pathogen has led to the development of almost all live vaccines currently in use, including those based on bacteria (BCG) or experimental vaccines against parasites (*Leishmania*) (Saljoughian et al., 2014). Likewise, continuous exposure to *Plasmodium falciparum*, the causative agent of malaria, and maintenance of low-grade parasitemia provides protection against high-density parasitemia and death in adults (Doolan et al., 2009). This phenomenon is often referred to as “concomitant immunity” (Brown and Grenfell, 2001) or, in the case of malaria, “premunition” (Doolan et al., 2009). Despite the strong indirect evidence that prior infection with Mtb confers

protection against reinfection, the underlying mechanisms have not been defined, in part due to the lack of a suitable small animal model.

Several recent studies have shown that vaccination with live bacteria (BCG) contributes to protection against TB disease, in part, by altering the activation state of the innate immune system. For example, protection against aerosol challenge with Mtb conferred by intravenous BCG vaccination was linked to epigenetic reprogramming of bone marrow derived macrophages in mice (Kaufmann et al., 2018). Additionally, BCG vaccination was able to prevent immune pathology and bacterial dissemination independently of CD4 T cells in a mouse model of TB reactivation (Sathkumara et al., 2019).

Recent work in mice has demonstrated that virulent Mtb which are injected into the dermis of the ear are asymptomatically contained in the draining lymph node for an extended period (Contained MTB infection model, CMTB). This model was used to mimic failure of containment arising from immune suppression and predicted a novel cell type as a niche for Mtb persistence in humans (Kupz et al., 2016; Tornack et al., 2017). In addition, the lymph involvement in this model reflects an important component of natural infection in primates; in both humans (Behr and Waters, 2014) and non-human primates (Ganchua et al., 2018), the lymphatic system plays a key role by providing a reservoir for latent Mtb (Wang, 1916) and coordinating subsequent immune responses.

Because the CMTB mouse model shares many features of asymptomatic Mtb infection in humans, we hypothesized that it reflects a portion of the Mtb-infection spectrum and would provide protection against active TB disease. In this Chapter, we demonstrate that CMTB in mice confers strong protection against both aerosol challenge with Mtb and heterologous challenges and is associated with amplified innate immune activation that is dependent on low levels of circulating interferon γ (IFNγ).

## Methods

### Ethics statement

All animal experiments were approved by the Institutional Animal Care and Use Committee at Seattle Children's Research Institute. Mice were sacrificed by $CO_2$ asphyxiation and/or cervical dislocation.

### Mice

C57BL/6J were purchased from the Jackson Laboratory (Bar Harbor, ME). Mice were housed and maintained in specific pathogen–free conditions at the Seattle Children's Research Institute (SCRI), and experiments were performed in compliance with the Institutional Animal Care and Use Committee. CMTB was established in 6- to 12-week-old male and female mice. Mice infected with Mtb. were housed in a biosafety level 3 facility in an animal biohazard containment suite. Cages of genetically identical mice were randomly assigned to experimental groups.

### Tissue culture

Alveolar macrophages were isolated from bronchoalveolar lavage (BAL) fluid by plate adherence (12 hours) and cultured in complete RPMI [cRPMI; plus 10% (vol/vol) FBS, 2 mM L-glutamine, penicillin, and streptomycin] for 24 hours. In vitro infections were performed in cRPMI without antibiotics in biological triplicate (cells from independent mice). The bacterial load at day 5 was determined by plating serial dilutions of cells lysed in 1% Triton-X and diluted in 0.1% Tween-80 PBS.

### Establishment of CMTB via intradermal infection of the ear, aerosol infections, and quantification of bacterial load

Intradermal infections to establish CMTB were performed as described previously (Kupz et al., 2016) with the following modifications: 10,000 colony forming units (CFU) of Mtb (H37Rv

strain) in logarithmic phase growth in 10 µL PBS were injected intradermally using a 10µL Hamilton Syringe into mice anaesthetized with Ketamine. In some experiments, Mtb Erdman was used with identical results. For aerosol infections, a frozen stock of Kanamycin-resistant Mtb H37Rv was diluted and used to infect mice in an aerosol infection chamber (Glas-Col). For high dose mEmerald infections, a deposition of 3000–5000 CFU was targeted. High dose aerosol infections were performed with a stock of wild-type H37Rv transformed with an mEmerald reporter pMV261 plasmid, generously provided by Dr. Chris Sassetti and Dr. Christina Baer (University of Massachusetts Medical School, Worcester, MA). For Ultra-low-dose (ULD) infections, a deposition of 1–3 CFU was targeted accepting a rate of approximately 30% uninfected animals. Bacterial load was determined independently for the left and right lungs by plating serial dilutions from homogenized tissue. Homogenates were plated on Kanamycin-containing plates and antibiotic-free plates to distinguish the origin of the infection (intradermal or aerosol infection). The percentage of mice infected (in one or more lungs) in each experimental condition was taken as a measure of the susceptibility to infection. This analysis assumes that no mice clear infecting bacteria to below the detection limit. The assumption of no clearance is supported by the observations that for each experimental condition (control or CMTB) there was no difference in the fraction of mice infected between day 42 and day 102 and that the average bacterial load did not decrease over this interval (Figure II.9). The degree of dissemination between lungs in each experimental group was estimated by assuming that dissemination is a Poisson process. For the actual infection rates achieved in the ULD experiments (~50% infected) 1 in 10 mice would be expected to be infected with more than 1 bacterium. In determining the statistical significance of a difference in the frequency of dissemination events between conditions, we make the conservative assumption of ignoring multiple infections (Figure II.10). For Mtb-infection experiments, the group sizes and experimental replication strategies were chosen based on previous experience with the “high-dose” (3000-5000 CFU), “conventional-dose” (50-100 CFU), and “ultra-low dose” (1-3 CFU)

infection models to ensure robust detection of protective effects as large as those observed for BCG vaccination of mice.

**Antibiotic treatment to clear CMTB**

CMTB was established and after 2 weeks mice were treated for 6 weeks with Isoniazid (0.1 mg/mL) and Rifampicin (0.1 mg/mL) in the drinking water. After the end of treatment, mice were switched to untreated water for at least 1 week to allow complete removal of the antibiotics from the system (Isoniazid half-life: 4 hours; Rifampicin half-life RIF: 2.5 hours). Efficacy of treatment was confirmed by plating undiluted tissue homogenates of cervical lymph nodes, lungs, and spleens.

**Heterologous challenges**

For experiments with bacterial burden as the endpoint, $10^5$ Listeria monocytogenes were injected i.v. and CFU in the spleen measured after 48 hours. The B16-F10 melanoma cell line (ATCC CRL-6475) was purchased from ATCC and expanded according to the supplier's instructions. For the melanoma challenges, $10^5$ melanoma cells per mouse were injected i.v. After 10 days, mice were sacrificed, lungs were extracted and bleached in Fekete's solution following a published protocol (Overwijk and Restifo, 2000), and the metastases were counted by an investigator blinded to the identity of each mouse.

**Cell isolation, analysis, and sorting**

For i.v. labeling, a PE labeled anti-CD45.2 antibody was injected i.v. 10 minutes prior to tissue harvest. Single-cell suspensions of lung cells were prepared by Liberase Blendzyme 3 (Roche) digestion of perfused lungs as previously described (Rothchild et al., 2019). Cells from spleens were prepared as previously described (Spleen digestion protocol, Miltenyi Biotec). Fc-receptors were blocked with an anti-CD16/32 antibody (clone 2.4G2). Cells were suspended in PBS (pH 7.4) containing 2.5% FBS and stained in saturating conditions with antibodies against various epitopes (Table II.2). Live cells were identified using Zombie Violet or Zombie Aqua

(BioLegend). Absolute numbers of cells were estimated using CountBright Absolute Counting Beads (Invitrogen) according to the published protocol of the manufacturer. Samples were fixed in 2% (vol/vol) paraformaldehyde and analyzed using a LSRII flow cytometer (BD) and FlowJo software (Tree Star, Inc.). Previously published gating strategies were followed (Misharin et al., 2013; Rose et al., 2012) and are shown in Figures II.30-34. For RNA-seq analyses, live alveolar macrophages were isolated from suspensions of lung cells using a BD Aria II cell sorter. Gating strategies are presented in Figure II.30 (T cells), Figure II.31 (Circulating monocytes), Figure II.32 (Lung myeloid cells), Figure II.33 (Peripheral blood monocytes in WT/Ifngr1-/- mixed bone-marrow chimeras), and Figure II.34 (Alveolar macrophages in WT/Ifngr1-/- mixed bone-marrow chimeras).

**CD11b+ cell enrichment and ex vivo stimulation**

Single cell suspensions prepared as described above from pooled lungs or spleens were positively enriched for CD11b+ using magnetic beads (Miltenyi Biotec). The cells were re-stimulated with TLR-agonists (LPS 10 ng/mL, Pam3CSK4 300 ng/mL, R848 100 ng/mL) and supernatants were collected 6 hours after re-stimulation and assayed by ELISA for TNFα.

**Measurement of cytokines and total protein**

Cytokines were measured by the Cytokine & Chemokine 36-plex Mouse ProcartaPlex panel (with a LEP and IFNB1 assays added, for a total of 38 analytes) using a Luminex Bio-Plex 200 analyzer per the manufacturer's instructions. For spleen and lung tissue, total protein levels were normalized using a commercial BCA assay from Thermo Scientific.

**Detection of Mtb-specific T cells**

For direct detection of Mtb-specific cells, APC-labeled MHC class II tetramers (I-Ab) containing the immunodominant epitope of the ESAT-6 protein of Mtb (ESAT-64–17:I-Ab) were made in house (Moguche et al., 2015). Pacific Blue-labeled MHC class I tetramers containing the stimulatory residues of the TB10.4 protein of Mtb (TB10.4 4–11:Kb) were obtained from the

National Institutes of Health Tetramer Core Facility. Tetramer staining on single-cell preparations was carried out as described previously (Moguche et al., 2015).

**Histology**

Dissected mouse lungs (left lobe) were fixed in 10% neutral-buffered formalin, processed routinely into paraffin, and stained with hematoxylin and eosin (H&E). H&E slides were digitized with an Olympus Nanozoomer and images captured with Nikon Digital Pathology viewing software. Samples were scored on a 0–4 severity scale (0 = normal or none; 1 = minimal; 2 = mild; 3 = moderate; 4 = severe) for the levels of alveolar hyperplasia, necrosis, and edema. Samples were scored on a 0–4 extent scale (0 = normal; 1 = <5%; 2 = 6–30%, 3 = 31–60%, 4 = >60%) for the fraction of the lung affected in any manner (Extent 1) and for the fraction of the lung affected in the worst manner (Extent 2). Samples were scored on a 0–4 scale (0 = none; 1 = few (<5 in focus); 2 = mild numbers (5–10); 3 = moderate numbers (11–20); 4 = marked numbers (>20)) for numbers of mixed granulomas (ill-formed granulomas with a mixture of macrophages and lymphocytes), defined granulomas (well-defined with separation of macrophages, epithelioid, or multinucleated giant cells with lymphoid aggregates), perivascular lymphoid aggregates, peribronchiolar lymphoid aggregates, histocytes (macrophages), foamy macrophages, neutrophils, cholesterol clefts, and acid-fast bacteria. Scoring was performed by a pathologist who was blinded to the experimental condition of each sample. For each condition, tissues from 5 mice were examined to determine a score for each parameter. An overall score was assigned for each condition by summing the scores for each parameter.

**Mixed-bone marrow chimeric mice**

Bone marrow cells were harvested from femurs and tibias. T cells were depleted from bone marrow cell suspensions with an anti-CD3e microbead kit (Miltenyi). CD45.1/2-expressing WT bone marrow (from C57BL/6 × B6.SJL-Ptprca; Jax Stock No. 002014) cells were mixed with an equal number of CD45.2-expressing Ifngr1−/− (B6.129S7-Ifngr1tm1Agt/J; Jax Stock No.

003288). We injected 5–10×$10^6$ total bone marrow cells into sub-lethally irradiated (600 rads) CD45.1-expressing mice (B6.SJL-Ptprca; Jax Stock No. 002014). Mice were allowed to reconstitute for 3 months, were bled, and circulating T cells were stained for CD45.1/CD45.2 to assess chimerism before infection.

**RNA-seq**

RNA isolation was performed using TRIzol (Invitrogen), two sequential chloroform extractions, Glycoblue carrier (Thermo Fisher), isopropanol precipitation, and washes with 75% ethanol. RNA was quantified with the Bioanalyzer RNA 6000 Pico Kit (Agilent). cDNA libraries for alveolar macrophages were constructed and amplified using the SMARTer Stranded Total RNA-Seq Kit v2—Pico Input Mammalian (Clontech) per the manufacturer's instructions. Libraries were amplified and then sequenced on an Illumina NextSeq (2 x 75, paired end). Stranded paired-end reads of length 76 were preprocessed: For the Pico Input prep, the first three nucleotides of R2 (v2 kit) were removed as described in the SMARTer Stranded Total RNA-Seq Kit—Pico Input Mammalian User Manual (v2: 063017); Read ends consisting of 50 or more of the same nucleotide were removed. The remaining read pairs were aligned to the mouse genome (mm10) + Mtb H37Rv genome using the GSNAP aligner (v. 2016-08-24) allowing for novel splicing. Concordantly mapping read pairs (average 10–20 million / sample) that aligned uniquely were assigned to exons using the subRead (v. 1.4.6.p4) program and gene definitions from Ensembl Mus_Musculus GRCm38.78 coding and non-coding genes. Differential expression was calculated using the edgeR package from bioconductor.org. False discovery rate was computed with the Benjamini-Hochberg algorithm. Raw and processed data are deposited in GEO (GSE126355).

**ATAC-seq**

The ATAC-seq protocol with modifications for PFA fixed cells as described by Chen et al. was used (Chen et al., 2016). Libraries were sequenced on a NextSeq 500 (Illumina) using a

150 (paired-end 2x76bp) cycle mid-output kit. Unique sequence read pairs were aligned to the combined Mus musculus (mm10) and Mycobacterium tuberculosis (H37Rv) genomes using the GSNAP aligner (Wu and Nacu, 2010; Wu and Watanabe, 2005) (v. 2016-08-24) after stripping off adapter sequences in a pairwise manner. Only pairs that aligned uniquely and concordantly to non-mitochondrial mouse chromosomes were retained. Start and end positions of the sequences were adjusted to extend 4 and 5 base pairs respectively to account for transposase adapter insertion (see (Buenrostro et al., 2015)). Peak calling was performed with MACS2 (2.1.0) (Zhang et al., 2008) using the start and end locations of the pairs to define fragment lengths. “Blacklisted” regions of known artificially high signal as defined by the ENCODE project were filtered out of peak regions (https://sites.google.com/site/anshulkundaje/projects/blacklists) (Dunham et al., 2012). Bigwig files for each biological group were generated by running MACS2 (Zhang et al., 2008) (https://github.com/taoliu/MACS) peak calling on combined alignments from all samples in the group and outputting a normalized bedgraph file followed by file conversion using the bedGraphToBigWig program (genome.ucsc.edu). The R package DiffBind (http://bioconductor.org/packages/release/bioc/vignettes/DiffBind/inst/doc/DiffBind.pdf) (Ross-Innes et al., 2012) was used to define consensus peak regions across samples and assign counts. Differential peak counts and significance were computed using the R package edgeR (McCarthy et al., 2012; Robinson et al., 2009). Raw and processed data are deposited in GEO (GSE126355).

**Statistical analysis**

Significance was determined using an unpaired two-tailed Student’s t-test unless otherwise specified.

## Results

### Intradermal Mtb-infection of mice recapitulates key aspects of human CMTB and is stable for up to 1 year

To establish a system in which to examine the protective effect of CMTB, we adopted a model that was originally developed to study mechanisms of Mtb containment (Kupz et al., 2016). We infected mice intradermally in the ear with 10,000 CFU of a commonly used virulent strain of Mtb, H37Rv (Kupz et al., 2016). Within 5 days, the bacteria traffic to the ipsilateral superficial cervical lymph nodes which, when extracted, are visibly enlarged. The bacterial burden in the draining lymph node is relatively stable for at least one year (Figure II.1) with minimal dissemination to the spleen (Figure II.2) and no detectable dissemination to the lung (detection limit 10 CFU/lung). We measured the circulating levels of 38 cytokines, and detected low amounts of circulating CXCL10 (mean 67 pg/mL, range 43–98 pg/mL), interferon-γ (IFNG) (mean 5.3 pg/mL, range 0.6–11.2 pg/mL), and IL6 (mean 7.2 pg/mL, range 0–14.4 pg/mL) in the first 6 weeks following the establishment of CMTB (Figure II.3). The serum concentrations of the remaining analytes measured are not substantially affected by CMTB (data not shown). These serum levels of IFNγ are 10 to 100 times lower than those in mouse models of active TB disease (Cheng and Schorey, 2018; Marquis et al., 2009). This cytokine pattern mirrors reported measurements in humans; asymptomatically Mtb-infected individuals typically exhibit circulating IFNγ levels in the low pg range (Huaman et al., 2016) while those with active disease have cytokinemia 10–100 times higher (Vankayalapati et al., 2003).

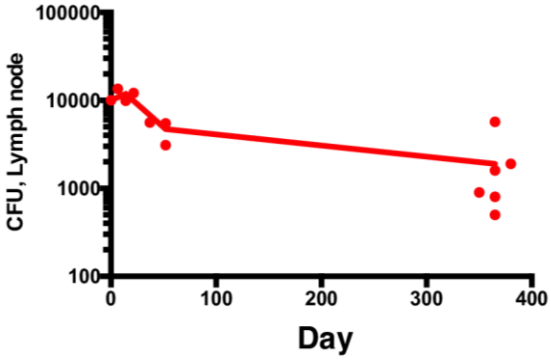


**Figure II.1 Mtb burden remains stable in lymph node**
Mice were inoculated intradermally in the ear with 10,000 CFU of H37Rv Mtb and bacterial burden in the superficial cervical lymph nodes measured 10, 42, and 365 days following infection by CFU assay. Data are a representative experiment of 2 independent experiments with 3–6 mice/timepoint.

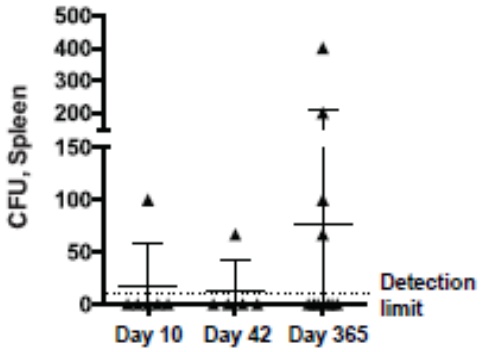


**Figure II.2 Minor dissemination to spleen in CMTB**
Mice were inoculated as in Figure II.1 and the bacterial burdens in the spleen and lung were measured at 10, 42, and 365 days later by CFU assay (4–5 mice/timepoint). No bacteria were detected in the lung in any sample (detection limit 10 CFU / lung).

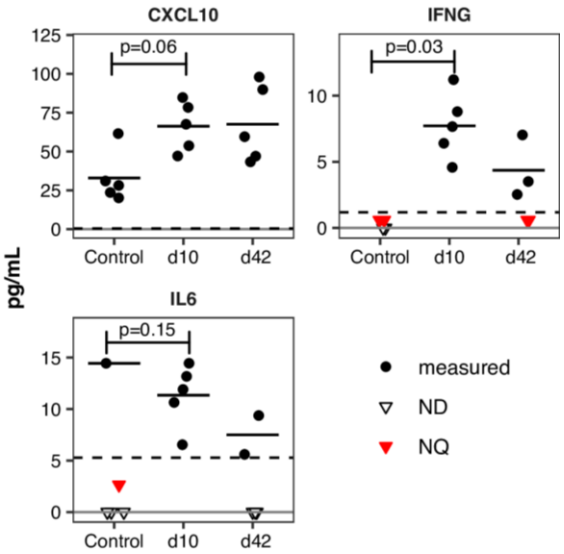


**Figure II.3 CMTB increases circulating cytokines**
CMTB was established and the levels of the indicated cytokines in peripheral blood were measured by multiplexed immunoassay (Luminex) at the indicated time points. ND = below detection limit; NQ = below quantification limit. Dashed line indicates the quantification limit. Out of 38 cytokines/chemokines assayed, only CXCL10, IFNγ, and IL6 exhibited CMTB-induced concentration changes (at Benjamini-Hochberg corrected $p < 0.2$). For statistical calculations, values below the detection limit were set to zero and values below the quantification limit were set to half of the quantification limit.

In humans, asymptomatic Mtb-infection is clinically defined by the presence of an Mtb-specific T cell response in the absence of active disease. In CMTB mice, Mtb-specific CD8 T cells are detectable in the circulation from day 10 onward without recruitment to the lung parenchyma (Figure II.4). However, we were unable to detect ESAT-6 specific CD4 T cells in peripheral blood, lung or spleen. Furthermore, for at least one year, the mice display no overt systemic symptoms (e.g. weight loss or changes in coat or behavior) nor any local symptoms (including visible inflammation or irritation). Taken together, these data indicate that intradermal Mtb-infection of mice recapitulates many key aspects of asymptomatic Mtb-infection in humans, including circulating Mtb-specific T cells in the absence of disease symptoms.

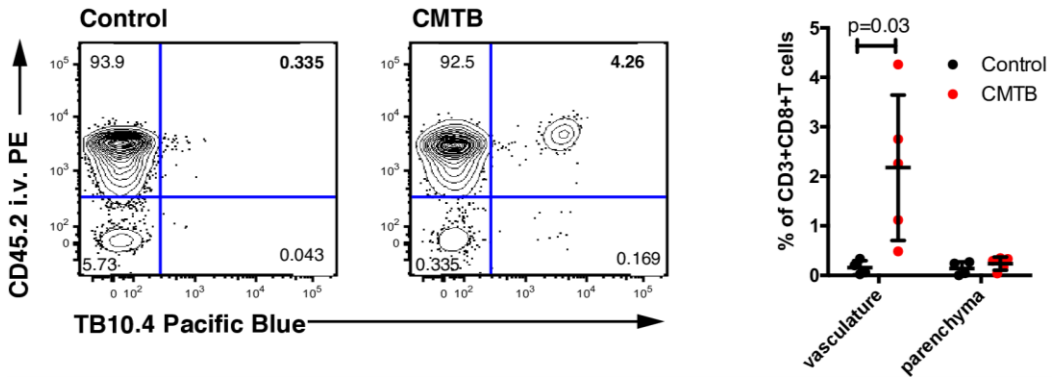


**Figure II.4 Mtb specific T cells detectable in CMTB mice.**
Relative proportions of CD3+CD8+TB10.4-tetramer-positive cells in the lung vasculature (CD45.2+) and parenchyma (CD45.2-) determined 42 days after the establishment of CMTB by flow cytometry. Localization to the vasculature or parenchyma was determined by i.v. labeling with an anti-CD45.2 antibody 10 minutes prior to blood collection. Data are representative of 2 experiments with n = 4–5 mice per experiment. Statistical significance was determined by Student's t-test. Error bars depict the mean and SD. (See Figure II.30 for gating strategy).

## CMTB mice are strongly protected against aerosol infection with Mtb and heterologous challenges

To test the hypothesis that CMTB is protective against aerosol infection, we challenged mice with 50–100 CFU of Mtb H37Rv 8–10 weeks after the establishment of CMTB and measured bacterial burden in the lung and spleen at 14, 42, and 100 days after infection. At each of these time points, the bacterial burden in both tissues is significantly lower in CMTB mice compared to controls (Figure II.5). We obtained similar results when mice were challenged 10 to 14 days after establishment of CMTB (Figure II.6): CMTB mice have on average 18.4-fold (CI: 10.6–26.3) fewer bacteria in the lung as compared to controls measured 6 weeks after aerosol challenge across 6 independent experiments with a total of 60 mice. This level of protection exceeds that observed in the standard model of BCG vaccination in mice (sub-cutaneous delivery of $1\times10^6$ CFU) which induces 10-fold protection at day 42 that wanes by day 100 and has minimal impact on bacterial burden during the first two weeks (Figure II.7).

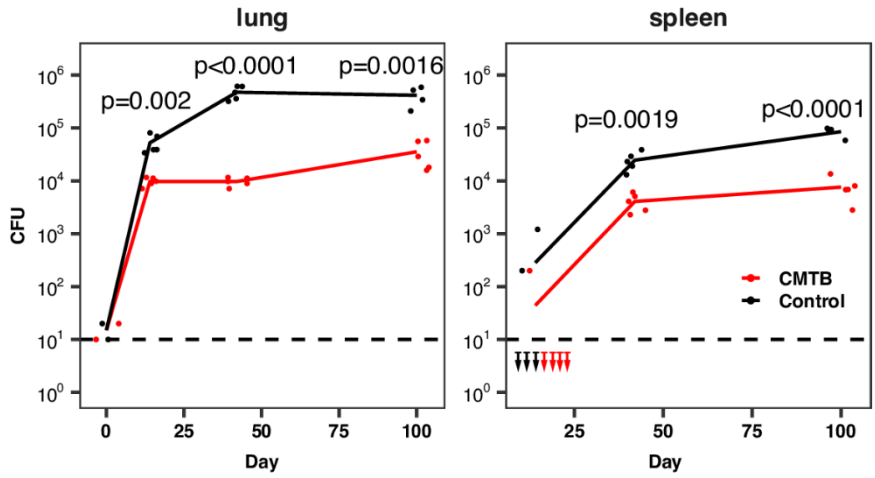


**Figure II.5 CMTB protects against aerosol challenge**
8 weeks after the establishment of CMTB, mice were challenged with 50–100 CFU of Kanamycin-resistant H37Rv via aerosol. Bacterial burdens in the lungs and spleen were measured by CFU at days 14, 42 and 100 following aerosol infection using plates containing Kanamycin. Plot shows representative data from one of two independent experiments (n = 4–5 mice per group). Statistical significance was determined by Student's t-test.

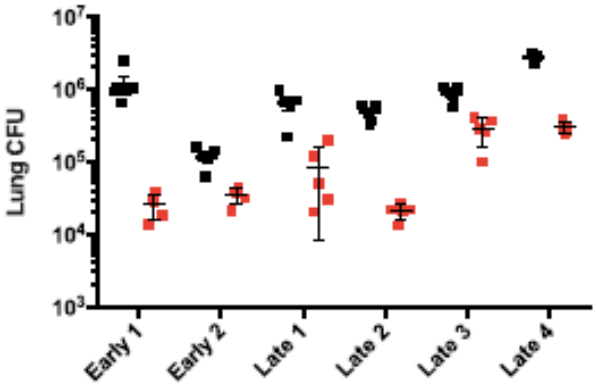


**Figure II.6 Protective effect of CMTB assessed at 6 weeks following aerosol challenge.**
CMTB was established as described in the main text and mice challenged with 50–100 CFU of Mtb H37Rv via aerosol after 10–14 days ("Early", 2 replicates) or after 8–10 weeks ("Late", 4 replicates). Bacterial burden in the lung was measured by CFU assay. CMTB mice had on average 18.4-fold (CI: 10.6–26.3) fewer bacteria in the lung as compared to controls. In each individual experiment, the bacterial burden in CMTB mice was lower than that in control mice as determined by Student's t-test ($p < 0.05$). Error bars depict mean and SEM. (n = 3–5 mice per group).

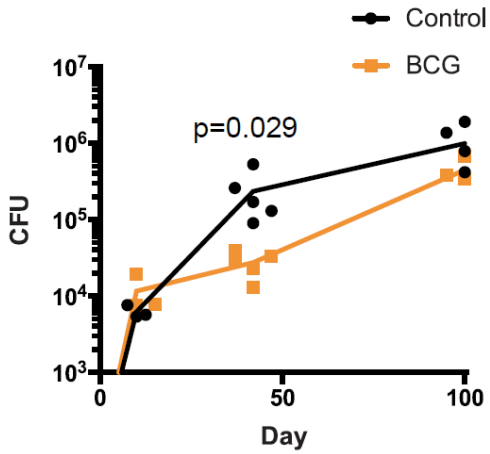


**Figure II.7 Protective efficacy of BCG Pasteur.**
Mice were immunized sub-cutaneously with $1x10^6$ CFU BCG Pasteur and challenged with 100 CFU Mtb H37Rv via aerosol 2 months later. Bacterial burden in the lung was measured by CFU assay at days 10, 42, and 100 following aerosol challenge (n = 4–5 mice per group). Statistical significance was determined by Student's t-test.

We hypothesized that the protective effect of CMTB results in part from the continuous interaction between the immune system and live bacteria and would be diminished by antibiotic treatment. Therefore, we established CMTB and after 2 weeks treated mice for 6 weeks with Isoniazid and Rifampicin. Treatment efficacy was confirmed by culture of lymph node, spleen, and lung lysates from a dedicated set of mice (data not shown). Mice were then challenged via aerosol with 50–100 CFU of H37Rv Mtb and bacterial burden in the lung and spleen was measured at 6 weeks. Antibiotic treatment diminishes the ability of CMTB mice to control bacterial growth in the lung and spleen over the first 6 weeks following aerosol infection (Figure II.8).

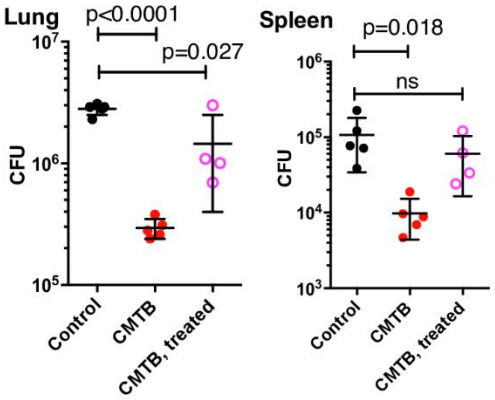


**Figure II.8 Antibiotic treatment reduces CMTB protection**
CMTB was established and after 2 weeks CMTB and control mice were treated for 6 weeks with Isoniazid and Rifampicin. Mice were challenged via aerosol with 50–100 CFU of H37Rv Mtb and bacterial burden in the lung and spleen measured 6 weeks later. Data are representative of 2 independent experiments with 4–5 mice per group. Error bars depict mean and SD.

Several lines of evidence suggest that human TB typically arises from infection with as few as 1–3 bacteria. We therefore examined the protective effect of CMTB against an “ultra-low dose” (ULD) challenge with a targeted average dose of ~1 CFU per mouse (see (Plumlee et al., 2020)). At this dose, 30–50% of mice remain uninfected and infected mice exhibit a wide range of outcomes, especially at later times, with bacterial burdens in the lung ranging over nearly 4 orders of magnitude (Figure II.9). Although CMTB does not affect the likelihood of becoming infected (56.4% (22/39) of control mice infected compared to 52.5% (21/40) of CMTB mice infected, see Chapter II Methods), for those mice that were infected the average bacterial burden in CMTB mice is more than 10-fold lower than in infected control mice (Figure II.9), consistent with the aerosol infections with 50–100 CFU. Furthermore, because most mice are

infected with a single bacterium, the degree of dissemination can be inferred by measuring spread to the contralateral lung lobe. CMTB mice exhibit reduced dissemination in the lung compared to controls at day 42 following ULD aerosol challenge (Figure II.10). Taken together, these data demonstrate that CMTB mice are strongly protected against aerosol challenge with Mtb from as early as day 14 until at least 100 days following infection.

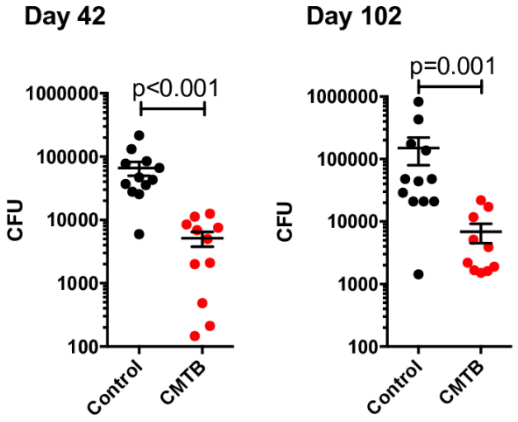


**Figure II.9 CMTB protects against ULD Mtb infection**
CMTB and control mice (20 per group) were infected with an average of 1 CFU of Mtb H37Rv via aerosol. Bacterial burdens in the lung were measured by CFU. Data are representative of two independent experiments. Mice with no detectable bacteria were omitted from the plot. Statistical significance was determined using the Mann-Whitney test. Error bars depict the mean and SEM.

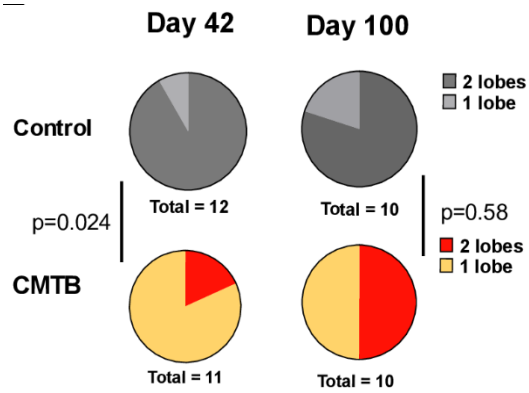


**Figure II.10 CMTB limits Mtb dissemination**
Fractions of control and CMTB mice with detectable bacteria in one or two lobes of the lung in the experiments shown in Figure II.9. Uninfected mice are excluded from the plot. Significance was assessed using the exact test for the difference of means in two Poisson distributions.

Both innate and adaptive immune responses are required for control of Mtb (North and Jung, 2004; Pai et al., 2016). We reasoned that if the protective phenotype of CMTB mice is fully explained by the presence of Mtb-specific T cells (Figure II.4), these mice should be equally susceptible to other immune challenges that do not share specific antigens with Mtb. To test this, we challenged CMTB and control mice intravenously with $10^5$ CFU of the intracellular bacterial pathogen Listeria monocytogenes. CMTB mice are significantly protected, displaying a greater than 100-fold reduction in bacterial burden in the spleen 48 hours following infection (Figure II.11). To confirm and extend these observations to a non-bacterial challenge, we

inoculated CMTB and control mice with B16-F10 melanoma cells which serve as a model of metastatic cancer. Ten days following i.v. injection of B16-F10 cells, CMTB mice have ~10-fold fewer metastases in the lungs than controls (Figure II.12). These results demonstrate that CMTB amplifies innate immune responses and raises the possibility that these responses may contribute to protection against diverse diseases, either directly, or through more robust recruitment of adaptive immunity.

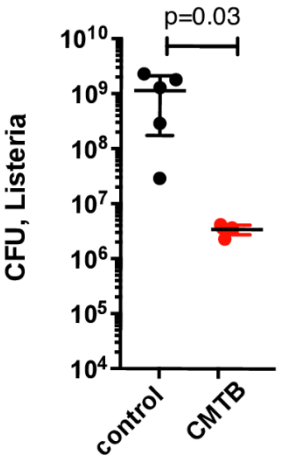


**Figure II.11 CMTB protects against Listeria infection**
CMTB and control mice were challenged i.v. with $10^5$ CFU of *Listeria monocytogenes* and bacterial burden in the spleen measured 48 hours following infection by CFU. Statistical significance was determined by Student's t-test. Data are representative of two independent experiments with 4–5 mice per condition.

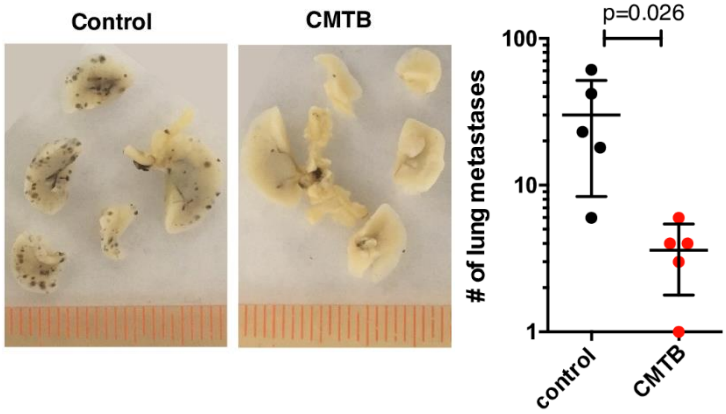


**Figure II.12 CMTB protects against metastatic melanoma**
CMTB and control mice were challenged i.v. with $1x10^5$ B16-F10 melanoma cells. Disease burden was quantified by counting the number of metastases visible in the lung 10 days following challenge (left panel, black spots). Data are representative data of three independent experiments with 4–5 mice per group. Significance was assessed by Student's t-test. Error bars depict the mean and SD.

**The protective phenotype of CMTB mice is associated with modest localized immune activation at baseline and an accelerated immune response**

Based on the heterologous protection induced by CMTB, we hypothesized that it modulates the innate immune system at baseline and in response to subsequent challenge leading to greater restriction of bacterial growth.

Although CMTB only modestly increases peripheral blood cytokines, we hypothesized that it might drive low-level, chronic immune activation in specific tissues. Therefore, we measured cytokine levels in the lungs and spleens of CMTB and control mice prior to aerosol challenge. During the first 6 weeks after the establishment of CMTB, the levels of 8 cytokines and chemokines (of 38 assayed) are significantly (FDR < 0.05) elevated in the lungs of CMTB mice compared to controls and 6 are elevated in the spleen (Figure II.13). The most pronounced changes are increased levels of CCL3, CCL4, and CCL5 in the lung and IFNγ and CCL4 in the spleen (Figure II.13). Relative levels of the detectable cytokines correlate well across tissues (Figure II.14). These results suggest that the localized, contained Mtb-infection induces a mild and selective increase in local tissue immune activation.

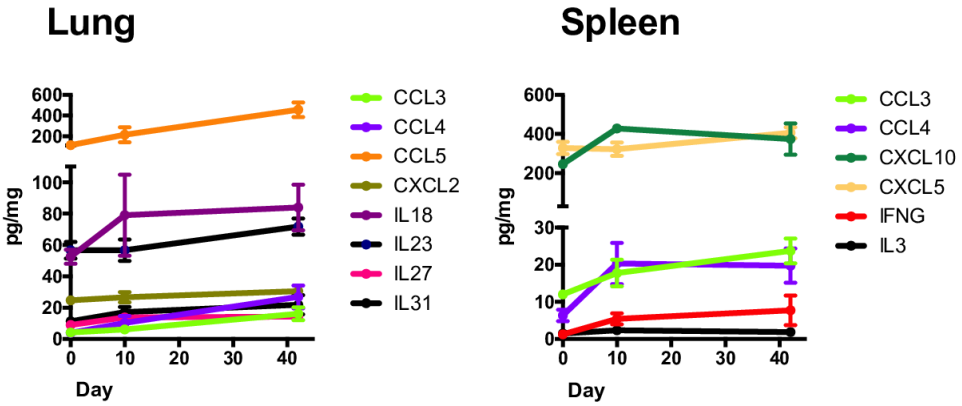


**Figure II.13 CMTB increases cytokines in tissues**
Tissues were isolated 10 or 42 days following the establishment of CMTB or from control mice (plotted at day 0). Absolute levels of cytokines and chemokines significantly altered by CMTB during at least one time-point in the lung or spleen (of 38 assayed) are plotted. Cytokine/chemokine amounts were normalized to total protein (n = 5 mice per time-point). A multiple t-test approach with Benjamini-Hochberg correction was used to test for significance (p < 0.05 for all analytes shown).

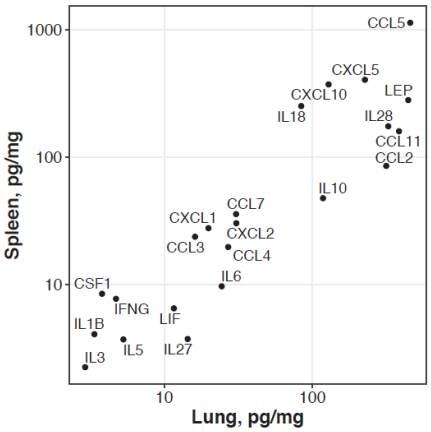


**Figure II.14 Cytokines correlate across tissues of CMTB mice**
CMTB was established and the abundances of selected cytokines and chemokines in the lungs and spleen measured by multiplexed immunoassay at day 42 following inoculation. The plot depicts the levels of analytes that were detected in both tissues. Each point represents the average of 5 mice.

Although the composition of the myeloid cell populations in the lungs of CMTB and control mice is not significantly different (Figure II.15), we hypothesized that the function might be affected by elevated cytokine levels in CMTB mice. Therefore, we assessed the overall responsiveness of myeloid cell populations in the lung by isolating CD11b+ cells from CMTB and control mice and stimulating them for 6 hours with TLR-agonists. Myeloid cells from CMTB mice are more responsive to all stimuli tested as measured by TNF-α secretion (Figure II.16).

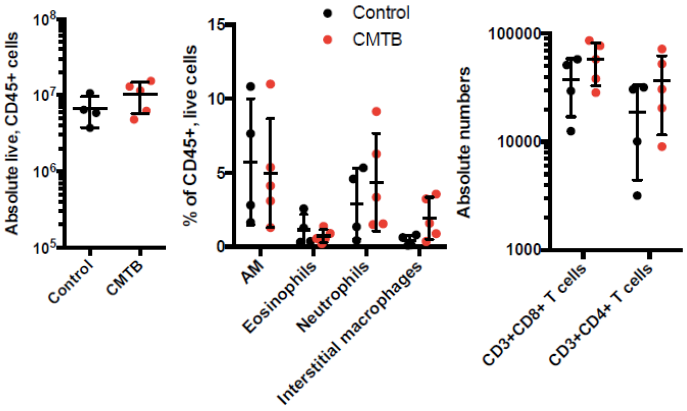


**Figure II.15 CMTB does not alter immune cell composition**
CMTB was established as described in the main text. At 8 weeks, immune cell populations were measured by flow cytometry using counting beads. Left panel: the absolute number of CD45+ cells in whole-lung homogenates. Middle panel: The relative proportions of myeloid cell populations (see Figure II.32 for gating). Right panel: The absolute numbers of CD4+ and CD8+ T cells (see Figure II.30 for gating). Data are representative of two independent experiments with 4–5 mice per condition.

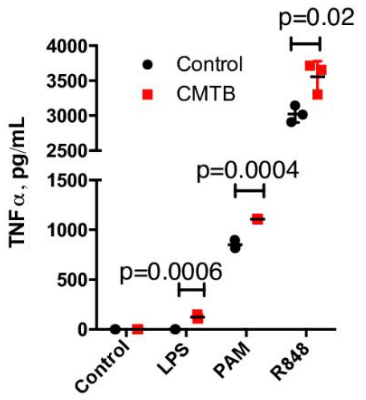


**Figure II.16 Myeloid cells from CMTB mice are more inflammatory**
CD11b+ cells isolated from the lungs of CMTB or control mice were stimulated for 6 hours with the indicated TLR agonists and secreted TNF measured by ELISA (LPS 10 ng/mL, PAM3 300 ng/mL, R848 100 ng/mL). Data are representative of three independent experiments with cells from 3–5 mice pooled per condition. Points indicate technical replicates and significance was assessed by Student's t-test. Error bars depict the mean and SD.

Next, we investigated the immune response after aerosol Mtb-infection (50–100 CFU) by histology of fixed lung sections. In contrast to control mice, which have essentially no histologically detectable immune response to aerosol Mtb-challenge at day 14 following infection, CMTB mice exhibit well-formed pulmonary lesions that remain stable for at least 100 days (Figure II.17). By day 42, control mice have significantly more lesions and pulmonary hemorrhages than CMTB mice and this damage continues to progress through day 100 (Figure II.17, Table II.1).

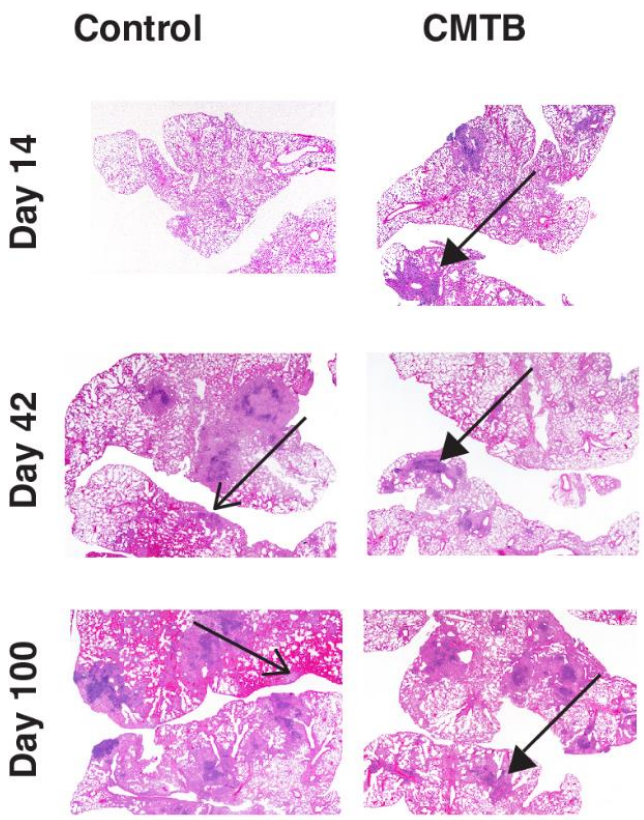


**Figure II.17 CMTB accelerates histological response and limits progression**
Hematoxylin and eosin stained lung sections from control and CMTB mice at the indicated time-points following aerosol challenge. Regions of infiltration by immune cells (filled arrow heads) and intrapulmonary hemorrhages (open arrow heads) are indicated. Representative images from 5 mice per condition are displayed at 2×.

| | Control | | | CMTB | | |
|---|---|---|---|---|---|---|
| **Feature** | day 14 | day 42 | day 100 | day 14 | day 42 | day 100 |
| Extent 1 | 1 | 3 | 3 | 3 | 2 | 2 |
| Extent 2 | 1 | 2 | 3 | 2 | 2 | 2 |
| Granulomas, mixed | 0 | 2 | 3 | 2 | 1 | 1 |
| Granulomas, defined | 0 | 2 | 2 | 2 | 1 | 3 |
| PV LA | 0 | 2 | 2 | 2 | 2 | 3 |
| PB LA | 0 | 2 | 3 | 2 | 1 | 1 |
| Histiocytes | 0 | 3 | 3 | 2 | 2 | 3 |
| Foamy macrophages | 0 | 2 | 3 | 1 | 1 | 3 |
| MNGC | 0 | 0 | 0 | 0 | 0 | 0 |
| Neutrophils | 0 | 2 | 2 | 1 | 0 | 0 |
| Alveolar hyperplasia | 0 | 0 | 0 | 0 | 0 | 0 |
| Necrosis | 0 | 1 | 1 | 0 | 0 | 0 |
| Cholesterol clefts | 0 | 0 | 1 | 0 | 0 | 0 |
| Edema | 0 | 0 | 1 | 0 | 0 | 0 |
| AFB | 1 | 3 | 3 | 1 | 2 | 1 |
| **Total** | **3** | **24** | **30** | **18** | **14** | **19** |

**Table II.1 Quantification of histological pathology**
Additional comments from pathologist: Control d42: moderate acute multifocal hemorrhages; Control d100: moderate acute multifocal to coalescing hemorrhages
PV LA: Perivascular lymphoid aggregates
PB LA: Peribronchial lymphoid aggregates
MNGC: Multi-nucleated giant cells, clearly defined >3 nuclei
AFB: Acid-fast bacilli

To identify the myeloid cells involved in the early response that we observed histologically, we measured the recruitment of immune cells to the lung by flow cytometry at early timepoints (days 10–14) after aerosol infection. More monocyte derived macrophages and Mtb-specific CD8 T cells are recruited to the lung at this early timepoint in CMTB mice compared to controls (Figure II.18). Although the numbers of alveolar macrophages (AMs) do not differ between control and CMTB mice at 10 days following aerosol challenge (data not shown), AMs from CMTB mice are more highly activated as measured by MHC II expression (Figure II.19). While we were unable to detect recruitment of ESAT-6 specific CD4 T cells at early timepoints, we measured an increase in the overall number of CD4 T cells in the parenchyma (Figure II.20). ESAT-6 specific CD4 T cells are only detectable at week 6 after aerosol infection without differences between the groups (Figure II.20).

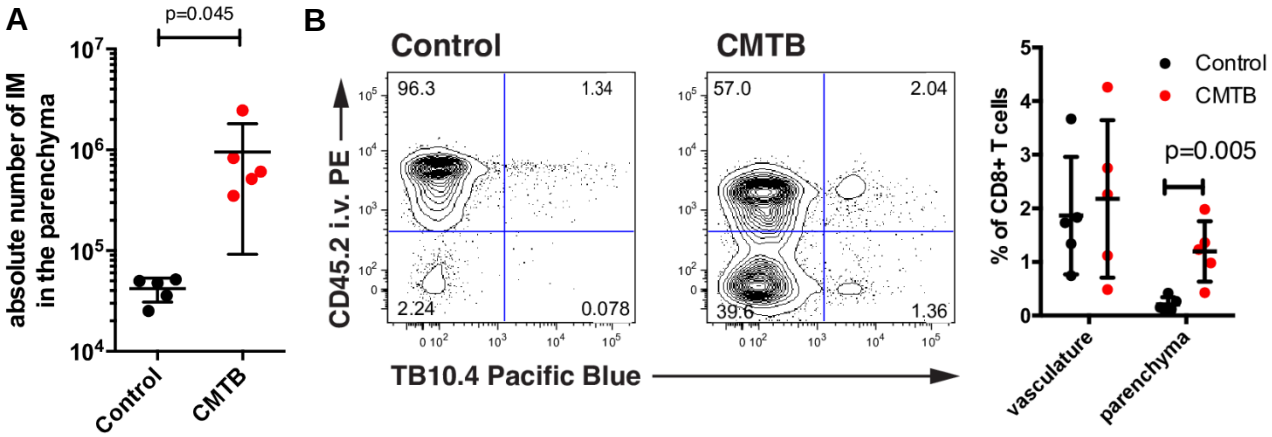


**Figure II.18 CMTB accelerates immune cell recruitment into lung parenchyma**
Immune cells in the lungs of control and CMTB mice were analyzed 14 days following aerosol infection with 100 CFU of Mtb H37Rv.
(A) Quantification of relative number of CD11b+CD11c+CD64+Siglec-F- monocyte derived macrophages in the lung parenchyma. Data are representative of two independent experiments with mice (n = 4–5) per condition (See Figure II.32 for gating strategy). (B) Representative cytometry plot and corresponding quantification of CD3+CD8+TB10.4+ cells in the vasculature (CD45.2-PE+) and lung parenchyma (CD45.2-PE-) (See Figure II.30 for gating strategy). Statistical significance was determined by Student's t-Test. Error bars depict the mean with SD.

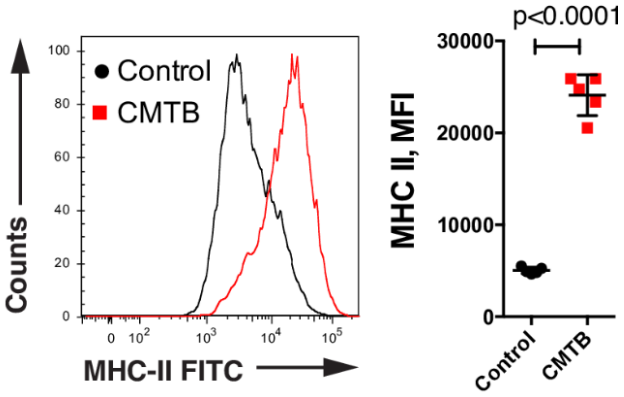


**Figure II.19 CMTB activates AM early after aerosol challenge**
Expression of MHC II on alveolar macrophages (CD11b$^{int}$CD11c+CD64+Siglec-F+) from control and CMTB mice isolated from the lung at 10 days following aerosol challenge (see Figure II.32 for gating). Data are representative of two independent experiments with 5 mice per condition. Statistical significance was determined by Student's t-test. Error bars depict the mean with SD.

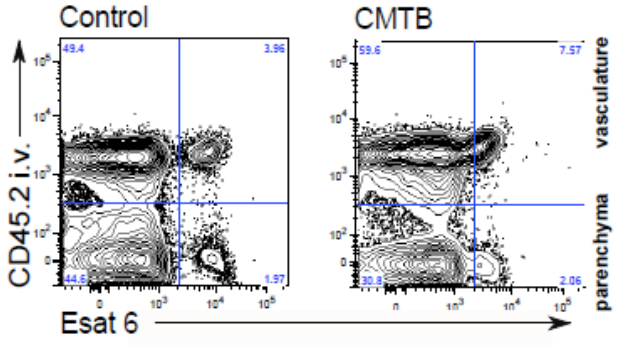


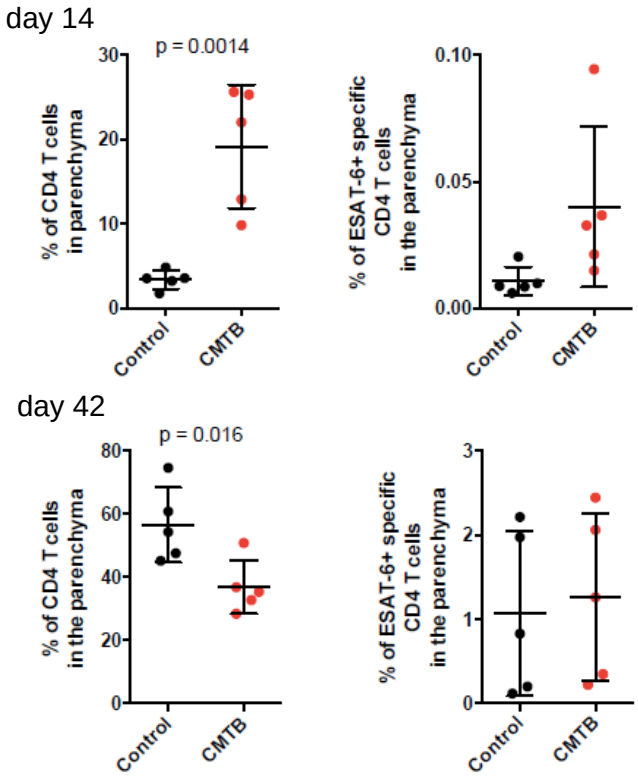


**Figure II.20 CMTB accelerates CD4 T cell recruitment into lung parenchyma**
A representative cytometry plot of CD3+CD4+ cells is shown. Quantification of total and Esat-6-specific CD3+CD4+ cells in the lung parenchyma (CD45.2-PE-) in control and CMTB mice at 14- (top) and 42-days (bottom) following aerosol infection with 100 CFU of Mtb H37Rv. Statistical significance was determined by Student's t-test. Error bars depict the mean and SD. Representative data from one of two independent experiments with 4–5 mice/group/timepoint. (See Figure II.30 for gating strategy.)

Antibiotic treatment to clear the contained infection reverses the accelerated immune response, including a reduction in 1) MHC II expression on AMs (Figure II.21) , 2) CD8 T-cell recruitment to the parenchyma (data not shown), and 3) the expansion of Mtb-specific T cells in response to infection (Figure II.22).

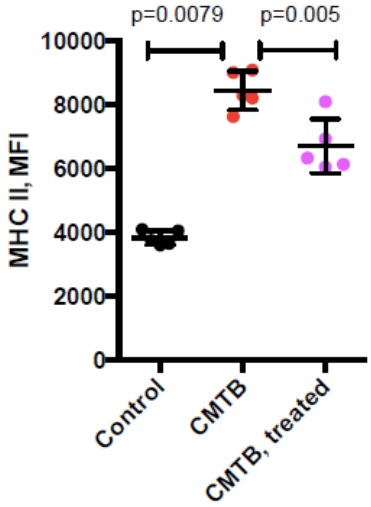


**Figure II.21 Antibiotic treatment decreases AM responsiveness to infection**
Flow cytometry analysis of alveolar macrophages from control, CMTB, and antibiotic-treated CMTB mice isolated 14 days following aerosol challenge with ~100 CFU Mtb H37Rv. AMs were defined as CD11b$^{int}$CD11c+CD64+Siglec-F+ (see Figure II.32 for gating). MHC II expression was quantified by median fluorescence intensity (MFI). Error bars represent the mean and SEM.

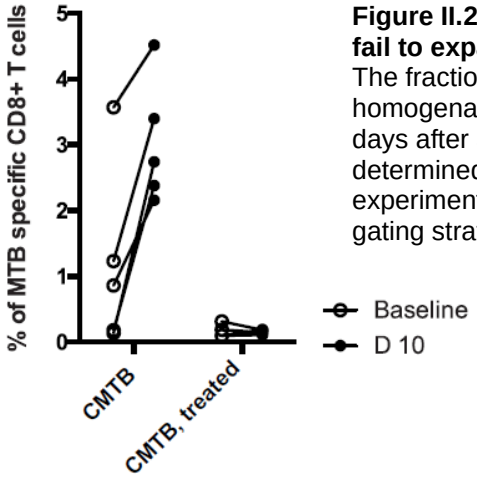


**Figure II.22 Mtb specific T cells in antibiotic treated CMTB mice fail to expand after aerosol infection**
The fraction of CD3+CD8+TB10.4+ T cells in whole lung homogenates of CMTB and control mice prior to (baseline) and 10 days after aerosol challenge with 50–100 CFU of Mtb H37Rv was determined by flow cytometry. Showing one representative experiment of two (n = 3–5 mice per group). (See Figure II.30 for gating strategy.)

These results suggest that a key feature of CMTB is an accelerated, early immune response that recruits effector cells including T cells and bone marrow derived macrophages reducing the time during which Mtb replicates unchallenged. Furthermore, CMTB mice maintain a protective response with minimal progression of immune pathology for a prolonged period. Finally, the early immune response observed in CMTB mice is dependent on live mycobacteria.

**Contained Mtb infection alters the response of alveolar macrophages to aerosol Mtb challenge**

Since the protective phenotype in CMTB mice is strongly associated with early recruitment of inflammatory cells to the site of infection (Figures II.17-20) and there is evidence of low-level tissue inflammation prior to challenge (Figure II.13), we hypothesized that CMTB affects the activation status and initial response of AMs (the lung resident macrophage and the first cells to be infected with Mtb).

Although the total number of CD45+ cells, T cells, and the fractions of various myeloid cell types in the lung are unaffected by CMTB (Figure II.15), we consistently measured elevated expression of MHC II and FcγRI (CD64) on AMs even in the absence of a secondary challenge (Figure II.23), suggesting that their activation state is altered by continuous exposure to low-level inflammation. To investigate the global transcriptional response of these cells, we performed RNA sequencing on AMs isolated from CMTB and control mice. Interestingly, the transcriptomes of AMs from control and CMTB mice do not differ substantially prior to aerosol challenge (Figure II.24).

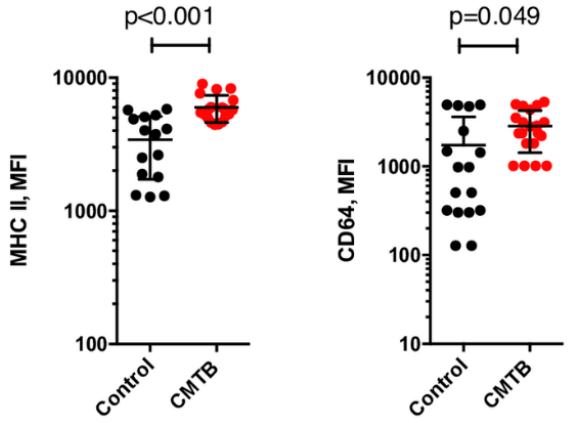


**Figure II.23 AM from CMTB are more activated at baseline**
Flow cytometry analysis of AMs from control and CMTB mice. Significance was determined by Student's t-test. Error bars depict the mean and SEM. (Data are pooled from 4 independent experiments with 3–5 mice per experiment).

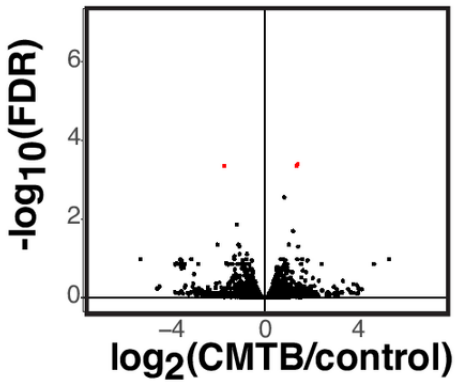


**Figure II.24 CMTB does not alter AM transcriptome at baseline**
AMs were isolated by FACS and the transcriptome assessed by RNA sequencing. The plot shows significance vs. fold-change in transcript expression between CMTB and control AMs. Red dots represent transcripts that were significantly differentially expressed between conditions (|log2(fold-change)| > 1 and FDR < 0.05). Each point represents the average of 3 biological replicates each pooled across the BAL from 10 mice.

To assess the immediate response of AMs to infection with Mtb, we challenged mice with a high dose (~3000 CFU) of mEmerald-expressing bacteria. In concordance with previous studies (Rothchild et al., 2019), at 24 hours following infection the bacteria are predominantly contained within AMs in both control and CMTB mice (data not shown). In other studies, we have shown that Mtb-infected AMs from control mice respond only minimally over the first week following infection and most pro-inflammatory genes are not expressed until approximately day 10 (Rothchild et al., 2019). RNA-seq analysis of AMs isolated from control and CMTB mice 24 hours after aerosol challenge demonstrated that CMTB dramatically alters the AM response to Mtb infection (Figures II.25). Gene Set Enrichment Analysis (GSEA) (Subramanian et al., 2005) of genes differentially expressed following infection showed that, in contrast to AMs from control mice, AMs from CMTB mice upregulate transcripts associated with inflammation and with the Interferon-γ and Interferon-α pathways (Figure II.26).

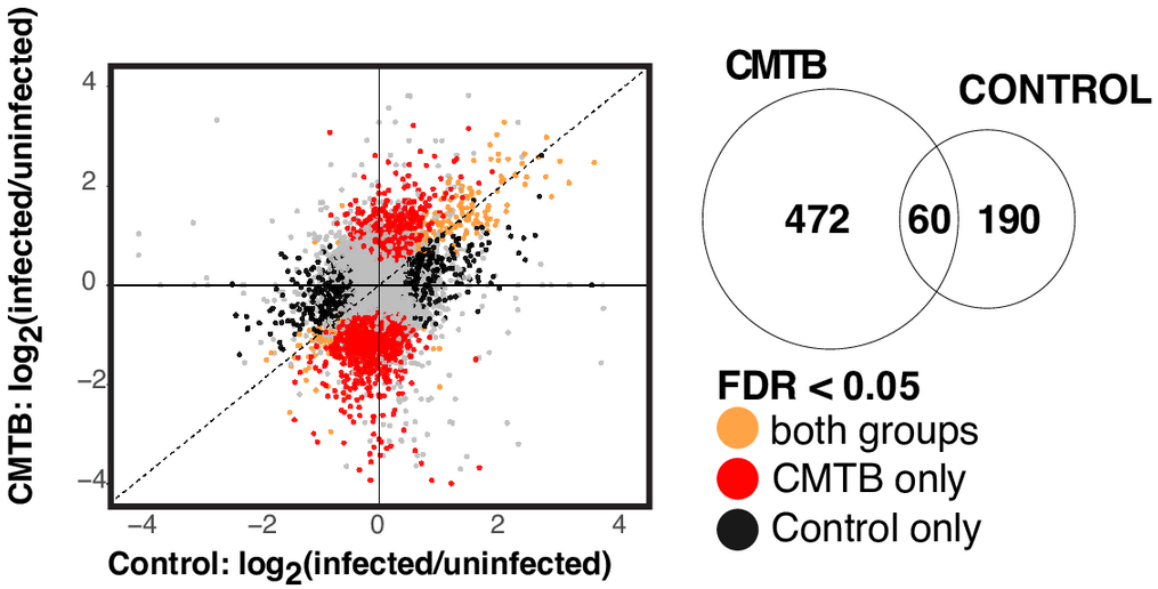


**Figure II.25 CMTB alters the AM response to aerosol Mtb challenge**
(left panel) $Log_2$ fold changes were calculated comparing infected AMs to uninfected AMs from both control and CMTB mice. Transcripts differentially responding to infection (|log2(fold-change)| > 1 and FDR < 0.05) are color-coded by whether they are differentially expressed in: red = CMTB only, black = control only, orange = both conditions. (right panel) VENN diagram showing the number of differentially expressed transcripts in each group.

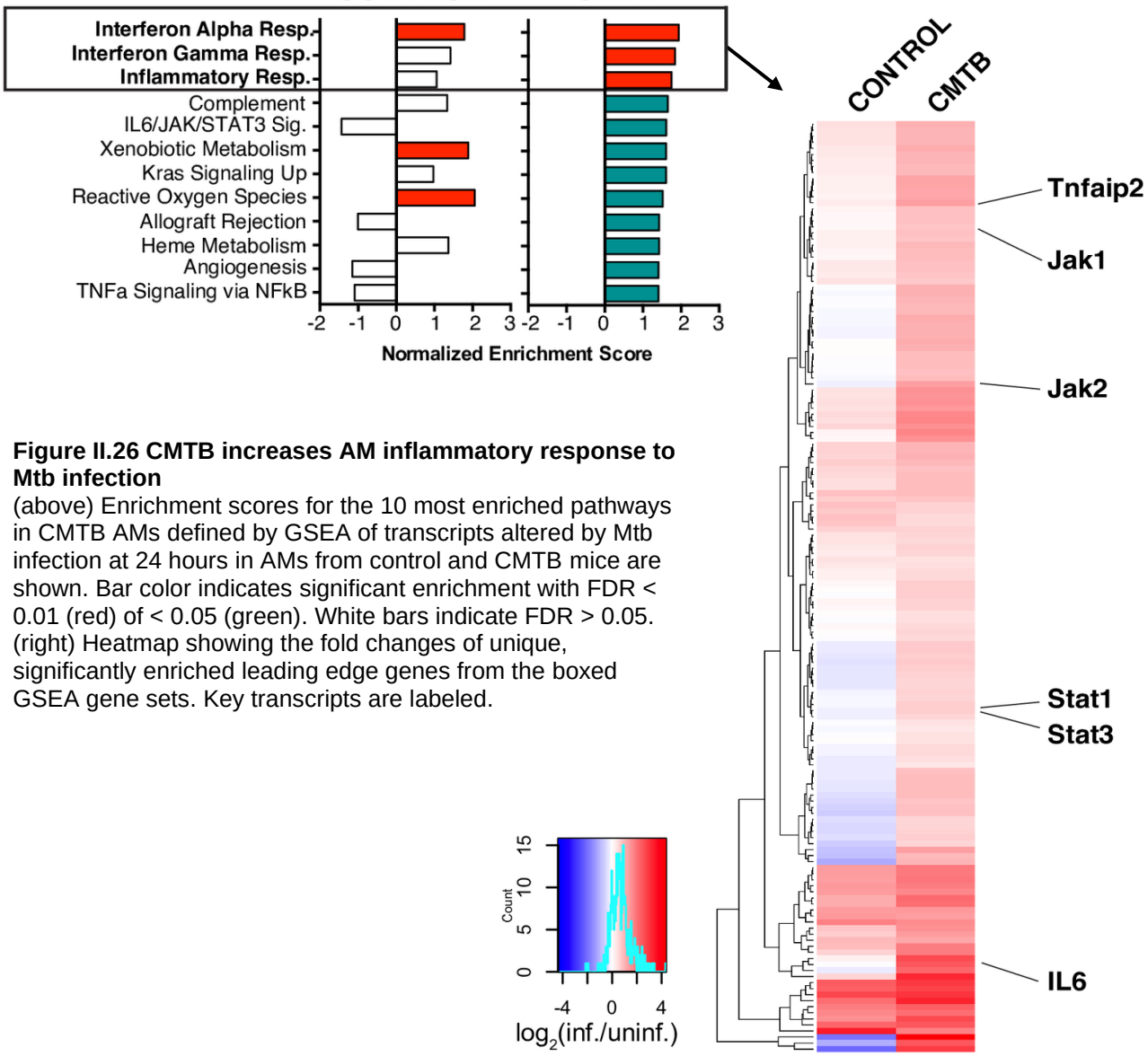


**Figure II.26 CMTB increases AM inflammatory response to Mtb infection**
(above) Enrichment scores for the 10 most enriched pathways in CMTB AMs defined by GSEA of transcripts altered by Mtb infection at 24 hours in AMs from control and CMTB mice are shown. Bar color indicates significant enrichment with FDR < 0.01 (red) of < 0.05 (green). White bars indicate FDR > 0.05. (right) Heatmap showing the fold changes of unique, significantly enriched leading edge genes from the boxed GSEA gene sets. Key transcripts are labeled.

The bacterial burden in CMTB mice at 10 days following high-dose (~3000 CFU) aerosol infection is approximately 3-fold lower than in control mice (Figure II.27). The majority of bacteria are in AMs and significantly fewer AMs are infected in CMTB mice (Figure II.27). We also measured a corresponding increase in the numbers of infected polymorphonuclear leukocytes (PMNs) in CMTB mice, suggesting an accelerated cellular response compared to controls (Figure II.27). AMs isolated by BAL from CMTB mice were better able to control Mtb infection *ex vivo* compared to controls suggesting that the enhanced response of AMs from CMTB mice is at least in part cell-intrinsic (Figure II.27).

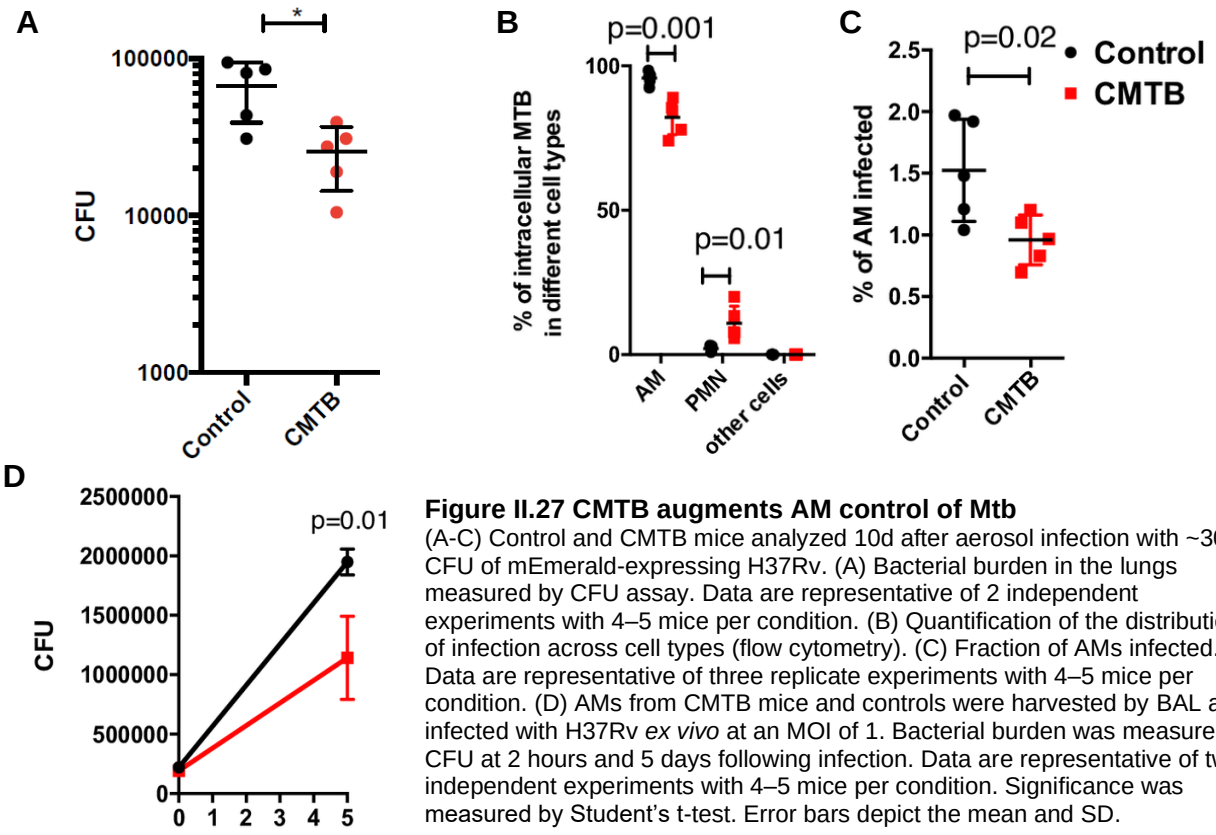


**Figure II.27 CMTB augments AM control of Mtb**
(A-C) Control and CMTB mice analyzed 10d after aerosol infection with ~3000 CFU of mEmerald-expressing H37Rv. (A) Bacterial burden in the lungs measured by CFU assay. Data are representative of 2 independent experiments with 4–5 mice per condition. (B) Quantification of the distribution of infection across cell types (flow cytometry). (C) Fraction of AMs infected. Data are representative of three replicate experiments with 4–5 mice per condition. (D) AMs from CMTB mice and controls were harvested by BAL and infected with H37Rv *ex vivo* at an MOI of 1. Bacterial burden was measured by CFU at 2 hours and 5 days following infection. Data are representative of two independent experiments with 4–5 mice per condition. Significance was measured by Student's t-test. Error bars depict the mean and SD.

Numerous recent studies have suggested that prior or ongoing infection can alter the capacity of innate immune cells to respond to subsequent encounters with pathogens, a phenomenon that has been termed "trained immunity" and has been shown in some cases to be reflected in epigenetic modifications (Netea et al., 2016). Therefore, we used ATAC-seq to measure genome-wide changes in chromatin accessibility induced by CMTB. Surprisingly, we observed only modest changes in chromatin accessibility that did not correlate with differentially expressed genes, suggesting that this mechanism cannot completely account for the enhanced response of AMs to infection (data not shown).

**The elevated immune activation in CMTB mice is dependent on systemic interferon γ**

We analyzed the activation state of mature monocytes in the peripheral blood of CMTB mice and found that a larger fraction expressed MHC II compared to control mice (Figure II.28). Given the slightly elevated levels of circulating IFNγ, the enrichment analyses of transcriptomes

from AMs in CMTB mice suggesting a prominent role of IFNγ signaling, and the known role of IFNγ in the control of both Listeria infections and melanoma (Harty and Bevan, 1995; Sanlorenzo et al., 2017), we hypothesized that low grade peripheral IFNγ cytokinemia increases myeloid activation in CMTB mice. To test this, we established CMTB in WT:Ifngr1-/- mixed bone marrow chimeras. In concordance with our hypothesis, MHC II is upregulated by CMTB in wild type circulating monocytes but not in monocytes lacking Ifngr1 (Figure II.29). The activation of AMs after aerosol Mtb challenge is similarly dependent on Ifngr1 with wild-type cells exhibiting elevated MHC II in CMTB that is not present in Ifngr1-/- cells (Figure II.29). Taken together, these data suggest that a significant portion of the altered activation state of both circulating and lung-resident innate cells in CMTB mice arises from low levels of systemic IFNγ.

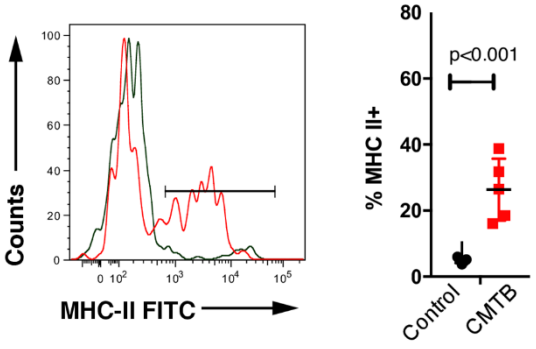


**Figure II.28 CMTB activates circulating monocytes**
MHC II expression on circulating monocytes in control and CMTB mice 6 weeks following the establishment of CMTB. (See Figure II.31 for gating strategy.) Significance was measured by Student's t-test. Error bars depict the mean and SD.

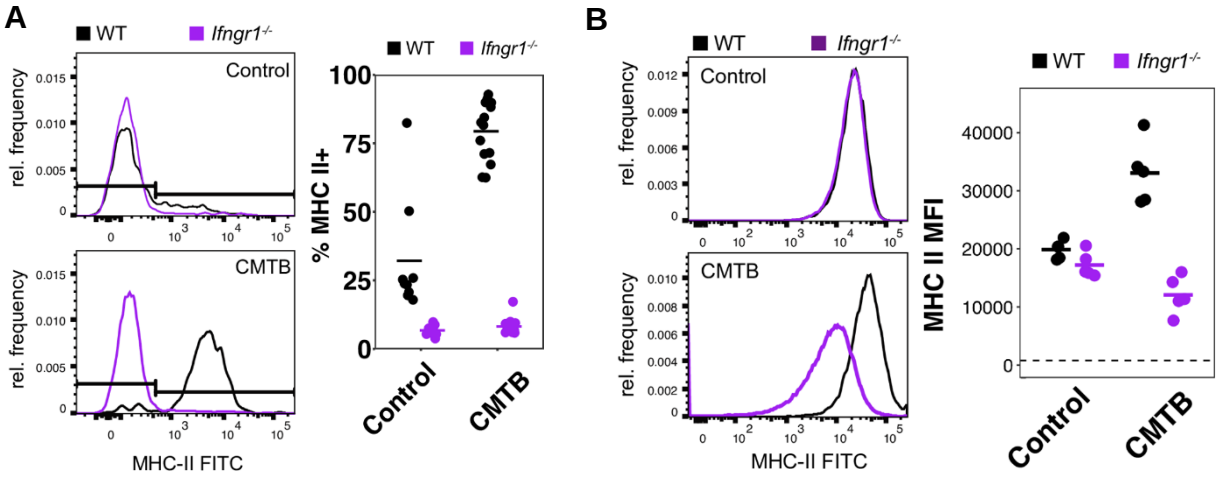


**Figure II.29 Immune activation in CMTB mice is dependent on Ifngr1**
(A) MHC II expression on circulating monocytes in WT:Ifngr1-/- mixed bone marrow chimeras with and without CMTB. (See Figure II.33 for gating strategy.) (B) MHC II expression on alveolar macrophages in WT:Ifngr1-/- mixed bone marrow chimeras with and without CMTB 24 hours after aerosol Mtb infection. Dashed line indicates MFI of MHC II in unlabeled cells. (See Figure II.34 for gating strategy).

## Discussion

In this Chapter, we demonstrate that contained Mtb-infection (CMTB) protects mice against subsequent aerosol challenge. In contrast to BCG, the “gold standard” and most widely studied vaccine in mice, CMTB leads to a reduced bacterial burden as early as 10 days following aerosol challenge which is maintained for at least 3 months. To our knowledge, this protection is as rapidly acting and durable as any that has been demonstrated in the mouse (Aagaard et al., 2011). Both qualities are highly desirable in a candidate vaccine against adult TB. Therefore, we argue that the CMTB mouse model offers an important opportunity to identify and dissect mechanisms of protection against TB through detailed studies comparing CMTB and BCG in order to reveal the correlates that distinguish these protective modalities.

While primed T cell responses undoubtably play a significant role in the protective effect of CMTB, our data suggest that amplified AM responses also contribute. In control mice, tissue resident AMs exhibit a cell-protective antioxidant response and have been shown to be the predominant niche for Mtb growth over the first week following infection (Cohen et al., 2018; Huang et al., 2018; Rothchild et al., 2019). In contrast, myeloid derived macrophages are better able to control bacterial replication. In fact, a recent study raised the possibility that the protection induced by BCG vaccination might be partially explained by an accelerated transfer of Mtb from AMs into bone-marrow-derived, inflammatory macrophages (Delahaye et al., 2019). The *in vivo* transcriptional response of AMs from CMTB mice, as early as 24 hours following infection, is altered towards a proinflammatory phenotype; Mtb-infected AMs from CMTB mice upregulate many of the inflammatory and interferon pathways that are activated in myeloid-derived macrophages but not in Mtb-infected AMs from control mice (Huang et al., 2018; Pisu et al., 2020; Rothchild et al., 2019). In addition to this shift towards a protective transcriptional program, AMs from CMTB mice infected with Mtb *ex vivo* control bacterial growth better than those from control mice. *In vivo*, at 10 days following aerosol challenge, fewer AMs from CMTB

mice are infected compared to controls, suggesting that bacterial spread is more effectively contained.

One outcome of a more robust innate response is an accelerated adaptive immune response. Our data suggest that systemic low-level inflammation changes the local lung environment in a manner that activates resident AMs, including increased MHC II expression, and that a substantial portion of this effect can be attributed to IFNγ. Given that the total number of CD45+ cells in the lung does not change, that we measure elevated levels of inflammatory mediators such as IFNγ, IL6, and CXCL10 in the blood, and that we observe increased activation of circulating innate immune cells, we believe it is likely that the increase in tissue cytokine levels arises from low grade cytokinemia. However, we cannot exclude the possibility of a contribution from immune cells that were activated in the cervical lymph node and subsequently migrate to the lung. Our data demonstrate that CMTB leads to a profound and early influx of both CD4+ and CD8+ T cells into the lung parenchyma after aerosol infection, which likely contributes to the protective effect and the long-term maintenance of protective immunity. Because T cells are critical for maintaining CMTB (Kupz et al., 2016), isolating the contributions of innate and adaptive immune mechanisms to protection is challenging. The IFNγ which drives elevated activation of AMs in CMTB mice most plausibly arises from Mtb-specific T cells, and therefore the distinction between “innate” and “adaptive” mechanisms in this model is somewhat artificial. More detailed studies are required to define the contributions of AM-intrinsic bacterial control, enhanced antigen-presenting cell activity, and memory T cells to the protective effect of CMTB.

Although we easily detect circulating TB10.4-specific CD8+ T cells in CMTB mice prior to aerosol challenge we were unable to detect ESAT-6 specific CD4+T cells in any compartment. In other studies using C57BL/6 mice, much greater numbers of TB10.4-specific CD8+ T cells were detected than ESAT-6-specific CD4+ T cells in both the lung and draining lymph nodes

during the first month following aerosol infection (Shafiani et al., 2010). Given that the bacterial burden in lymph node in the CMTB model is much lower than that in the lung at 30 days following aerosol challenge ($10^4$ CFU vs. $10^5$−$10^6$ CFU) our results are consistent with previous measurements of the relative abundances of these T cell subsets induced by Mtb-infection.

Concomitant immunity, defined as a low-grade infection that protects against subsequent infections with the same pathogen, has been described for several different pathogens, but most commonly for helminths and protozoan parasites (Belkaid et al., 2002; Brown and Grenfell, 2001; North and Kirstein, 1977). For example, in a mouse model of Leishmania infection, sterilizing protection against secondary challenge was dependent on persisting parasites from the first infection (Belkaid et al., 2002). In this Chapter, we show that the protection afforded by CMTB depends on the persistence of live bacteria: Antibiotic treatment of CMTB mice reduces the numbers of Mtb-specific T cells in the circulation and in the lung parenchyma following aerosol challenge and eliminates their expansion following infection. Furthermore, antibiotic treatment partially reverses elevated MHC II expression on tissue-resident AMs.

Several lines of evidence indicate that prior infection with Mtb, and presumed ongoing asymptomatic containment, provides significant protection against reinfection in humans. Studies from the pre-antibiotic era suggest that nursing students who were previously infected with Mtb were less likely to develop TB disease in a high-exposure setting than those who were not (Andrews et al., 2012). On an epidemiological level, it is impossible to accurately model Mtb transmission in highly endemic regions without accounting for the protective effect of prior infection and increased susceptibility after treatment (Blaser et al., 2016). Since a sub-clinical, contained infection is assumed to be occurring in a subset of humans who have been exposed to Mtb (Barry et al., 2009; Pai et al., 2016) and post mortem studies suggest that lymph nodes are a significant reservoir of bacteria (Behr and Waters, 2014; Wang, 1916), we believe that

CMTB in mice reflects a portion of the protective mechanisms of natural immunity against TB in humans and provides a needed model to better understand the underlying mechanisms.

The potential role of CMTB-mediated heterologous protection in humans has not been rigorously assessed. However, beneficial heterologous effects of BCG vaccination have been reported. Overall mortality of BCG-vaccinated newborns is reduced by more than would be expected from the protection afforded by BCG against TB alone (Higgins et al., 2016). The observation that BCG has profound, heterologous beneficial effects in both children and adults provides an additional argument in favor of BCG vaccination (Goodridge et al., 2016; Jensen et al., 2015; Usher et al., 2019). To more directly look at possible CMTB effects in humans, we have extended the findings in this Chapter to individuals infected with HIV; an LTBI diagnosis is associated with lower viral loads and decreased risk of opportunistic infections in this human cohort (Kusejko et al., 2020).

The vast majority of humans with latent TB acquire the bacteria by inhalation whereas CMTB in mice is established by intradermal inoculation, leaving the lung naïve to infection. Nevertheless, the CMTB model shares numerous features with latent tuberculosis in humans including live, contained bacteria, absence of overt symptoms, circulating Mtb-specific T cells, and a requirement for immune modulators such as TNF in maintaining bacterial containment. The current medical standard for patients with latent tuberculosis infection in non-endemic areas is prophylactic antibiotic treatment. Given the non-negligible side-effects of the current antibiotic regimes and the increasing prevalence of antibiotic-resistant Mtb, the appropriate management for latent tuberculosis in high-incidence settings remains a matter of considerable debate. While our work cannot provide a definitive answer to this public health question, it does contribute to our understanding of CMTB and raises important issues that need to be considered when crafting population-level strategies for TB control. A deeper understanding of the protective

mechanisms generated by CMTB, coupled with the development of related biomarkers to risk-stratify patients (Zak et al., 2016), would substantially inform clinical practice.

## Appendix

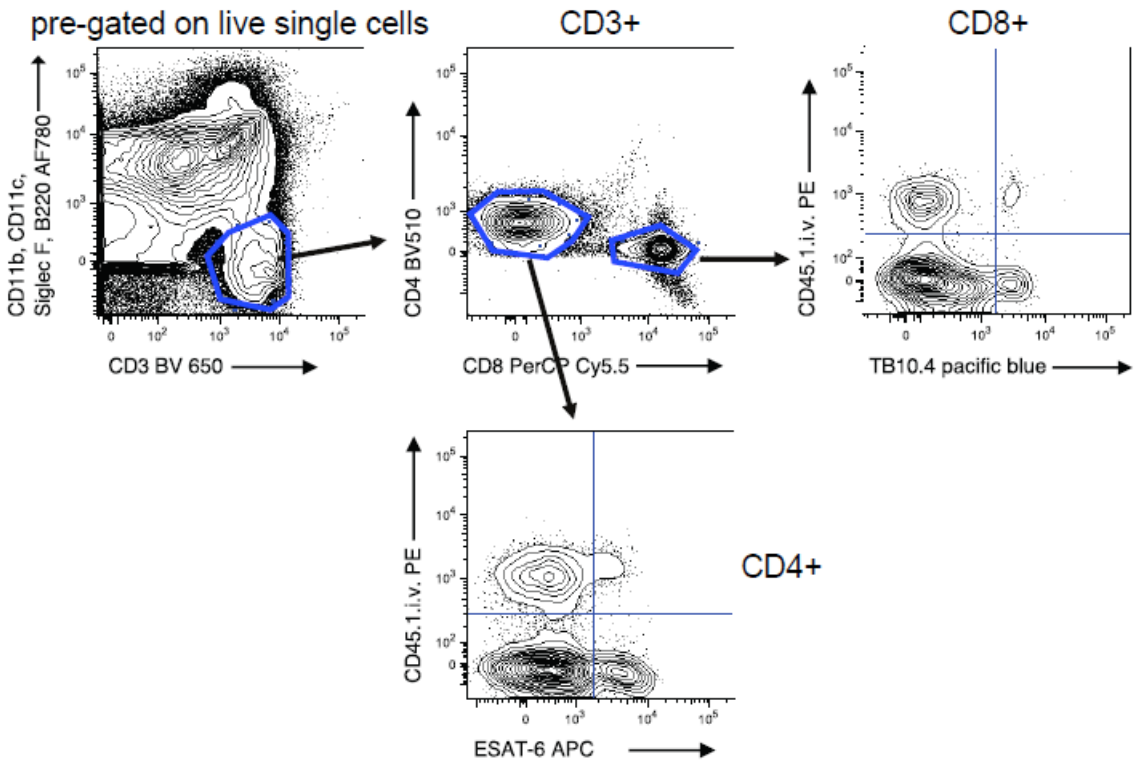


**Figure II.30 Gating strategy for lung and peripheral blood T cells**
Live (Zombie Violet-) single cells were gated on CD3, excluding Siglec-F+ (in lung samples only), CD11b+, CD11c+, and B220+ cells to define T cells. T cells were then gated on CD4 and CD8. For lung samples, localization of T cells to the lung parenchyma or vasculature was determined by i.v. labeling with an anti-CD45.2 PE antibody.

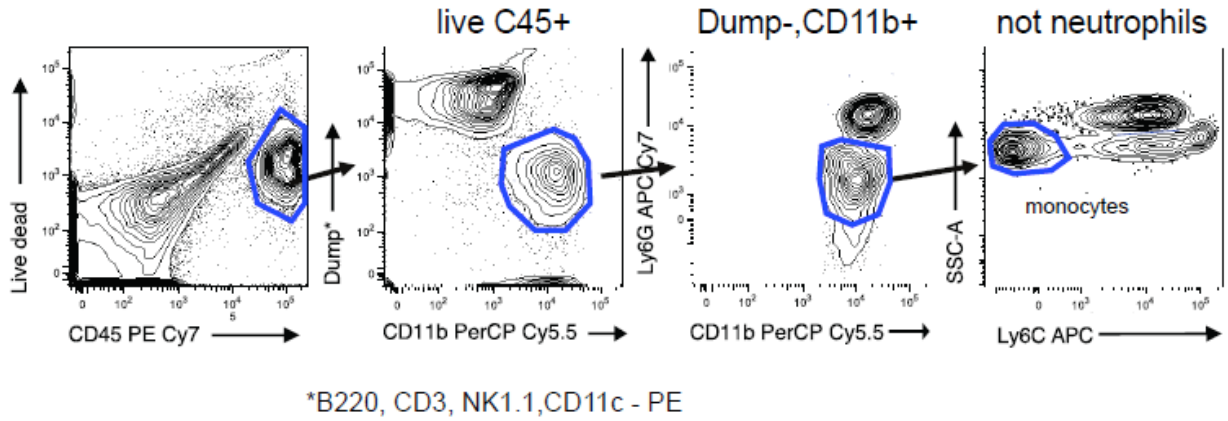


**Figure II.31 Gating strategy for peripheral blood monocytes**
Live (Zombie Violet-) single cells were gated on CD45, excluding B220+, CD3+, NK1.1+. These cells were then gated on CD11b+, followed by exclusion of Ly6G+ and Ly6C+ to define monocytes.

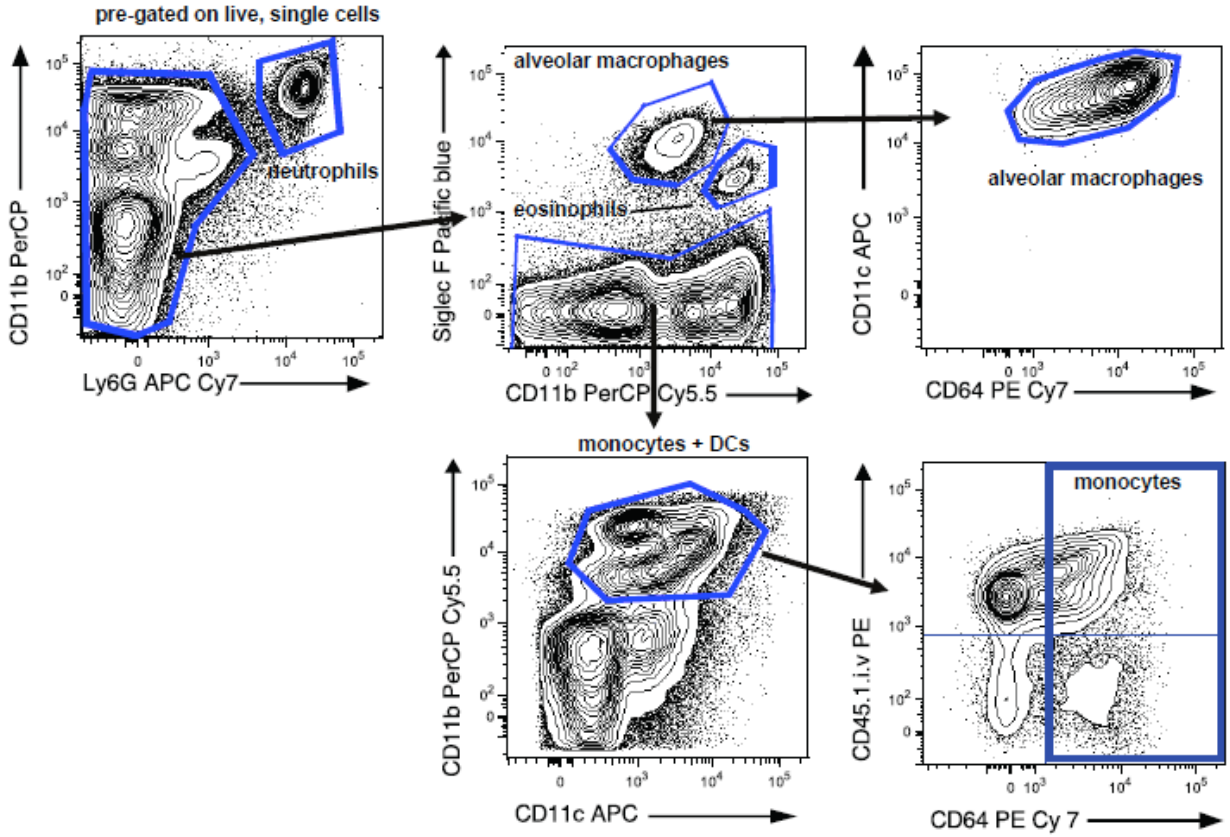


**Figure II.32 Gating strategy for lung myeloid cells**
Live (Zombie Violet-) single cells were gated on CD11b and Ly6G to define neutrophils (CD11b+ Ly6G+). Ly6G- cells were further gated on Siglec-F and CD11b to isolate eosinophils (Siglec-F+ CD11b$^{high}$), alveolar macrophages (Siglec-F+ CD11b$^{mid}$), monocytes/interstitial macrophages and dendritic cells (Siglec-F-). In order to robustly isolate alveolar macrophages in inflamed lungs, Siglec-F+ CD11b$^{mid}$ cells were further gated on CD11c and CD64.

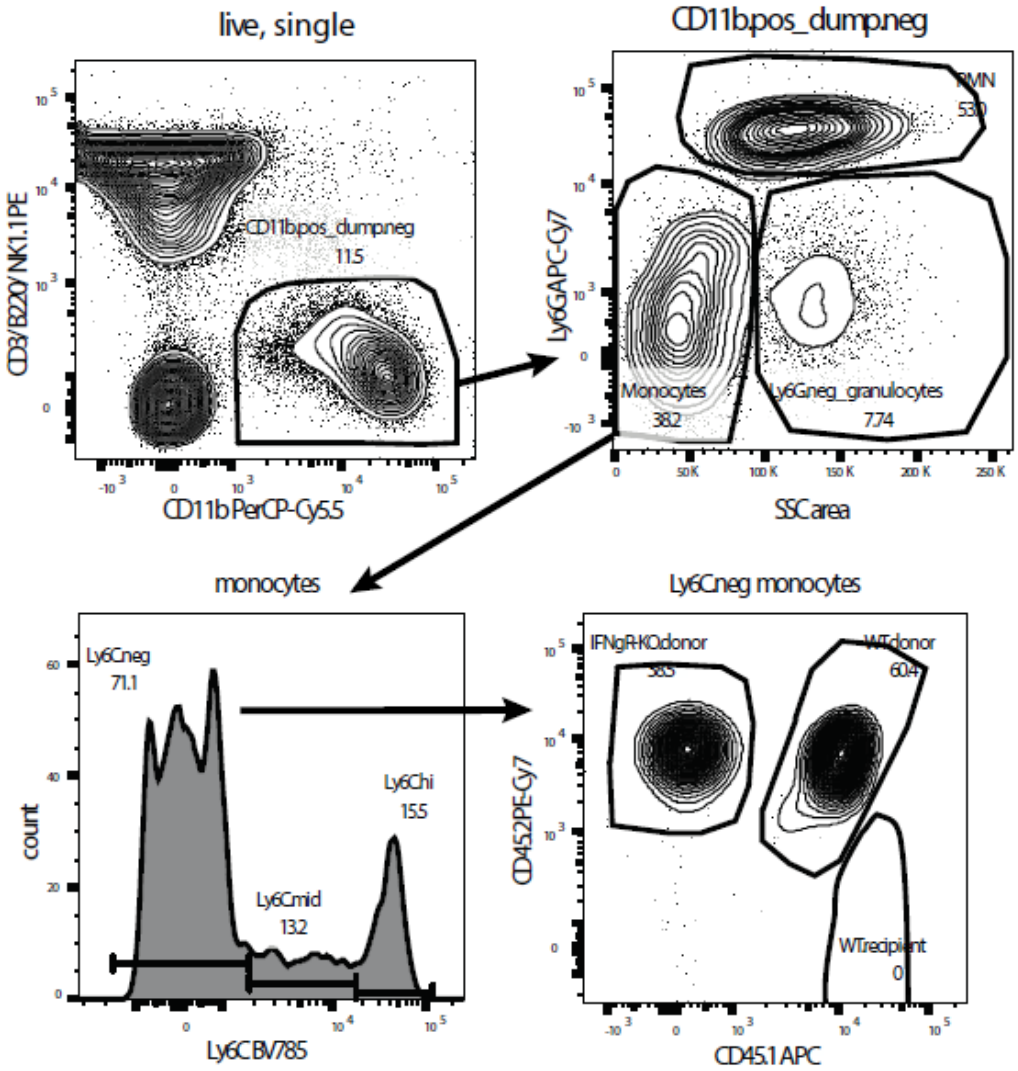


**Figure II.33 Gating strategy for peripheral blood monocytes in WT/Ifngr1-/- mixed bone-marrow chimeras.**
Live (Zombie Violet-) single cells were gated on CD11b+, excluding CD3, B220, and NK1.1. Monocytes were defined from this population as $SSC^{low}$, Ly6G- cells and their genotypes assigned by CD45.1/2 labeling.

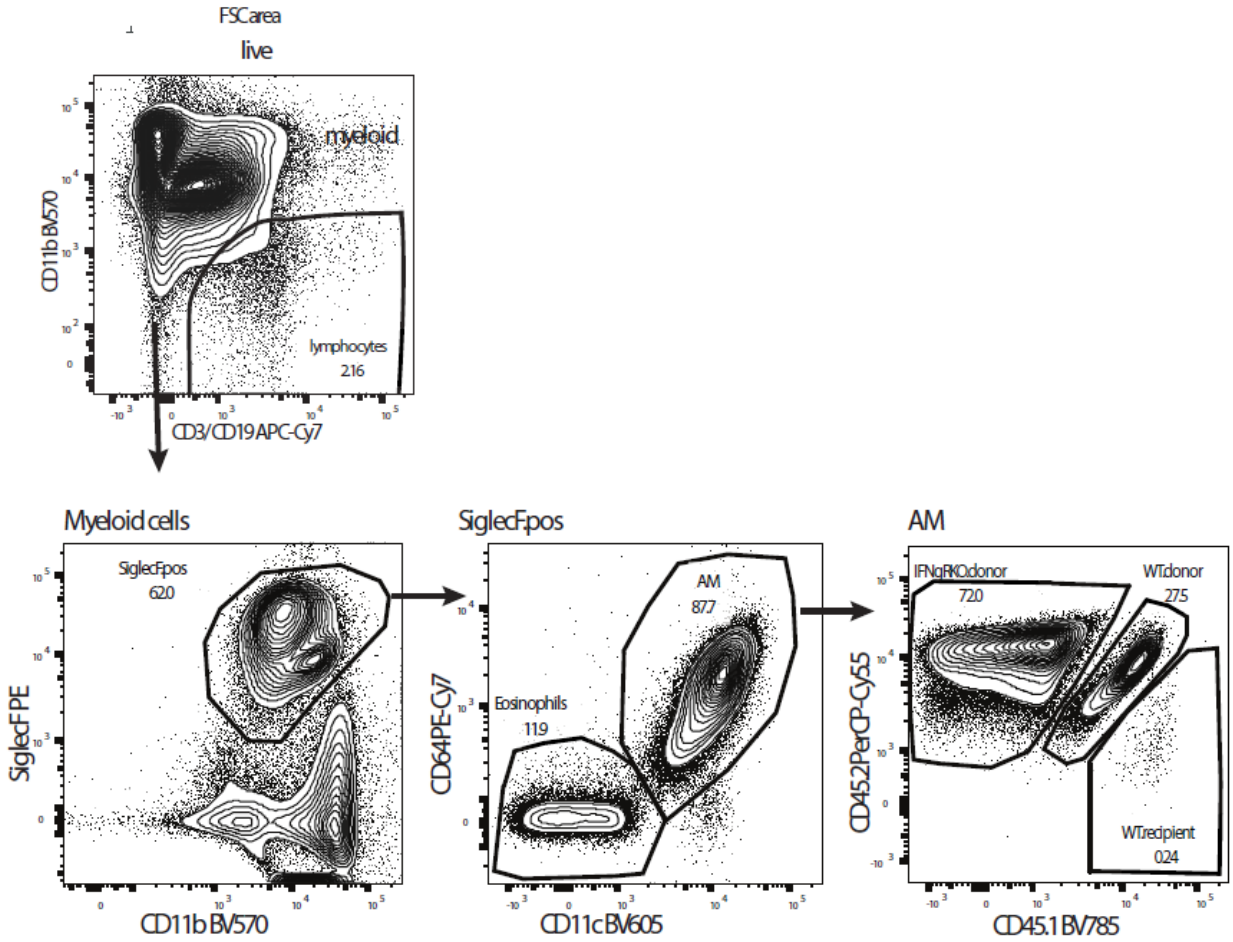


**Figure II.34 Gating strategy for alveolar macrophages in WT/Ifngr1-/- mixed bone-marrow chimeras.**

CD3+ and CD19+ cells were excluded from live, single cells to define the myeloid population. Alveolar macrophages were defined from this population as Siglec-F+, CD11c+, CD64+ cells and their genotypes assigned by CD45.1/2 labeling.

| Vendor | Product_Number | Description |
|---|---|---|
| BioLegend | 103128 | Alexa Fluor 700 anti-mouse CD45 antibody |
| BioLegend | 100729 | Alexa Fluor 700 CD8 antibody anti mouse |
| BioLegend | 117310 | APC anti-mouse CD11c Antibody |
| BioLegend | 100516 | APC anti-mouse CD4 Antibody |
| BioLegend | 103112 | APC anti-mouse CD45 Antibody |
| BioLegend | 100712 | APC anti-mouse CD8a Antibody |
| BioLegend | 128015 | APC anti-mouse Ly-6C Antibody |
| BioLegend | 100221 | APC/Cy7 anti-mouse CD3 Antibody |
| BioLegend | 107627 | APC/Cy7 anti-mouse I-A/I-E Antibody |
| BioLegend | 128026 | APC/Cy7 anti-mouse Ly-6C Antibody |
| BioLegend | 115539 | Brilliant Violet 605, anti-mouse CD19 Antibody |
| BioLegend | 100237 | Brilliant Violet 605, anti-mouse CD3 Antibody |
| BioLegend | 100204 | FITC anti-mouse CD3 Antibody |
| BioLegend | 103108 | FITC anti-mouse CD45 Antibody |
| BioLegend | 137005 | FITC anti-mouse CD68 Antibody |
| BioLegend | 107605 | FITC anti-mouse I-A/I-E Antibody |
| BioLegend | 103006 | FITC anti-mouse/human CD44 Antibody |
| BioLegend | 108905 | FITC CD49b NK cell anti mouse |
| BioLegend | 100534 | Pacific blue CD4 antibody anti mouse |
| BioLegend | 103126 | Pacific Blue, anti-mouse CD45 Antibody |
| BioLegend | 104723 | Pacific Blue, anti-mouse CD80 Antibody |
| BioLegend | 103106 | PE anti-mouse CD45 Antibody |
| BioLegend | 103207 | PE anti-mouse/human CD45R/B220 Antibody |
| BioLegend | 115508 | PE CD19 B cell anti mouse |
| BioLegend | 117317 | PE/Cy7 anti-mouse CD11c Antibody |
| BioLegend | 109109 | PE/Cy7 anti-mouse CD279 (PD-1) Antibody |
| BioLegend | 100219 | PE/Cy7 anti-mouse CD3 Antibody, 25ug |
| BioLegend | 103114 | PE/Cy7 anti-mouse CD45 Antibody |
| BioLegend | 139313 | PE/Cy7 anti-mouse CD64 (FcGRI) Antibody |
| BioLegend | 123113 | PE/Cy7 anti-mouse F4/80 Antibody |
| BioLegend | 100538 | PerCP anti-mouse CD4 Antibody |
| BioLegend | 103130 | PerCP anti-mouse CD45 Antibody |
| BioLegend | 103132 | PerCP/Cy5.5 anti-mouse CD45 Antibody |
| BioLegend | 100733 | PerCP/Cy5.5 anti-mouse CD8a Antibody |
| BioLegend | 103031 | PerCP/Cy5.5 anti-mouse/human CD44 Antibody |
| BioLegend | 101320 | TruStain (anti-mouse CD16/32) Antibody |
| BioLegend | 423102 | Zombie Aqua, Fixable Viability Kit |
| BioLegend | 423114 | Zombie Violet |
| Fisher Scientific L.L.C. | BDB557401 | PE Hamster Anti-Mouse CD11c |
| Fisher Scientific L.L.C. | BDB552126 | PE Rat Anti-Mouse Siglec-F |
| Fisher Scientific L.L.C. | BDB562419 | PE-CF594 Rat Anti-Mouse CD127 |
| Fisher Scientific L.L.C. | BDB550993 | PerCP-Cy,5.5 Rat Anti-CD11b Clone M1/70 (RUO) |
| Thermo Fisher Scientific Life Technologies | 47-0112-80 | CD11b Monoclonal Antibody (M1/70), APC-eFluor 780, eBioscience |
| Thermo Fisher Scientific Life Technologies | 17-0128-42 | CD11c Monoclonal Antibody (BU15), APC |
| Thermo Fisher Scientific Life Technologies | 63-0451-82 | CD45 Monoclonal Antibody (30-F11), Super Bright 600 |
| Thermo Fisher Scientific Life Technologies | MHCD4526 | CD45 Monoclonal Antibody (HI30), Alexa Fluor 405 |
| Thermo Fisher Scientific Life Technologies | MF48005 | F4/80 Monoclonal Antibody (BM8), APC |
| Thermo Fisher Scientific Life Technologies | BDB562681 | BV421 Rat Anti-Mouse Siglec-F Clone E50-2440 (RUO) |
| Thermo Fisher Scientific Life Technologies | L34957 | LIVE/DEAD, Fixable Aqua Dead Cell Stain Kit |
| Thermo Fisher Scientific Life Technologies | 56-5321-80 | MHC Class II (I-A/I-E) Monoclonal Antibody (M5/114.15.2), Alexa Fluor 700, 25ug |

**Table II.2 Antibodies used in Chapter II**

# Chapter III: Type I interferon controls macrophage energy metabolism during mycobacterial infection

Sections of text in this chapter have been modified slightly from the following manuscript: **Olson, G.S.,** Murray, A.M., Jahn, A.N., Mai, D., Diercks, A.H., Gold, E.S., Aderem, A. (2021). Type I interferon controls macrophage metabolism during mycobacterial infection. *In preparation*.

## Introduction

The new model of contained *Mycobacterium tuberculosis* (Mtb) infection described in Chapter II raises many questions about the nature of the immune response that is protective against secondary Mtb challenge and heterologous challenges. Unfortunately, however, our incomplete understanding of the molecular events controlling the macrophage response to Mtb hinders future mechanistic studies. In this Chapter, we employ a more tractable *in vitro* model to address an unresolved question about the macrophage response to Mtb infection: what controls the macrophage metabolic response to Mtb infection?

Although initial studies contended that Mtb infection shifts macrophages towards aerobic glycolysis (Gleeson et al., 2016; Lachmandas et al., 2016a, 2016b) (similar to the purified inflammatory stimuli discussed in Chapter I), recent reports suggest that Mtb infection decreases *both* glycolytic and mitochondrial metabolism in macrophages (Cumming et al., 2018; Hackett et al., 2020; Howard et al., 2018; Rahman et al., 2020). Two variables provide the most likely explanations for the discrepancies: the viability and virulence of the Mtb and the macrophage subset. The initial studies showing a glycolytic shift mainly used Mtb lysates or killed Mtb (Gleeson et al., 2016; Lachmandas et al., 2016a), while live, virulent Mtb decreases both metabolic programs of macrophages (Chen et al., 2006b; Cumming et al., 2018; Hackett et al., 2020; Wiens and Ernst, 2016). Macrophages are a heterogeneous group, and two different macrophage subsets play pivotal roles during early Mtb infection (see Chapters I and II). It has

been proposed that the divergent metabolic responses of alveolar macrophages (AMs) and monocyte derived macrophages (MDMs) contribute to their divergent control of Mtb (possibly by altering nutritional availability to Mtb) (Huang et al., 2018; Pisu et al., 2020), but the signals that control the metabolic responses remain elusive.

In this Chapter, we began with the hypothesis that we could exploit the divergent responses of murine bone marrow-derived macrophages (BMDM) to live and heat killed (HK) H37Rv (a virulent strain of Mtb) to identify mechanisms controlling macrophage metabolism during Mtb infection. Our initial findings support recent studies that live Mtb infection decreases both glycolysis and mitochondrial respiration in BMDM more than HK Mtb. Interestingly, we identified that activation of type I IFN signaling correlates with these differences. Although it is well known that Mtb virulence is required for type I IFN induction in macrophages (Collins et al., 2015; Manzanillo et al., 2012; Wassermann et al., 2015; Watson et al., 2015), how type I IFN shapes the macrophage metabolic or transcriptional response to Mtb is poorly characterized. We then demonstrate that IFNAR knock out (KO) BMDM maintain both glycolytic capacity and mitochondrial health during Mtb infection. Importantly, we confirm that type I IFN decreases macrophage metabolism *in vivo* during an aerosol infection with Mtb. We then substantiate that type I IFN acts *upstream* of mitochondrial health in macrophages by studying the metabolic response of STING KO BMDM to Mtb infection. Consistent with our predictions, STING KO BMDM maintain glycolytic capacity and mitochondrial health upon Mtb infection, while exogenous type I IFN added during Mtb infection in STING KO BMDM recapitulates the decreased metabolism seen in WT macrophages.

## Methods

### Mice

WT (C57BL6/J; RRID:IMSR_JAX:000664), IFNAR KO (B6.129S2-Ifnar1$^{tm1Agt}$/Mmjax, RRID:MGI:3703445), STING KO (B6(Cg)-Sting1$^{tm1.2Camb}$/J, RRID:IMSR_JAX:025805), and IL10

KO (B6.129P2-Il10tm1Cgn/J, RRID: IMSR_JAX:002251) strains of *Mus musculus* were obtained from The Jackson Laboratory. MyD88-TRIF double KO mice were generated from the two strains MyD88 KO (B6.129P2(SJL)-Myd88$^{tm1.1Defr}$/J, RRID: IMSR_JAX:009088) and TRIF KO (C57BL/6J-Ticam1$^{Lps2}$/J, RRID: IMSR_JAX:005037). All KO mouse experiments used only homozygous animals. All mice were housed and maintained in specific pathogen–free conditions at the Seattle Children's Research Institute (SCRI). All experiments were approved by the Institutional Animal Care and Use Committee and then performed in compliance with the relevant protocols. Healthy eight- to 14-week-old female mice without any previous procedure history were used for all experiments and were age-matched within each experiment.

**Bone marrow derived macrophages**

Female mice (see section on Mice for further details) were euthanized with carbon dioxide asphyxiation. Bone marrow was harvested from the femur and tibia by flushing with BMDM media [RPMI 1640 supplemented with recombinant M-CSF (50 ng/mL), L-glutamine (final concentration 4 mM), and 10% fetal bovine serum (FBS)] plus penicillin and streptomycin (p/s). The flushed marrow was homogenized by pipetting and then filtered through a 70 μm filter before being placed at 37 ºC, 5% $CO_2$ in four 15 cm plates. Fresh BMDM media was added on day 3 or 4 and then on day 6 the adherent cells were washed twice and then lifted with PBS + 2mM EDTA. Cells were replated in BMDM media without p/s and rested overnight at 37 ºC, 5% $CO_2$ before treatments or infections were added.

**Sorted macrophage subsets**

WT or IFNAR KO female mice were infected with Mtb by aerosol (see below for infection details) and then group housed, segregated by genotype, in a biosafety level 3 facility in an animal biohazard containment suite. Fifteen days after infection, mice were euthanized by cervical dislocation and the superior, middle, and inferior lobes of the right lung were isolated by dissection. Single-cell suspensions of lung mononuclear cells were prepared by Liberase TM

(70 µg/ml) digestion in 1µM HEPES buffer containing deoxyribonuclease I (DNase I) (30 µg/ml) for 30 min at 37°C and mechanical disruption using a gentleMACS dissociator (Miltenyi Biotec), followed by filtering through a 70 µm cell strainer. Red blood cells were removed by incubating with ACK lysis buffer for 2 minutes before neutralization with FBS. Cells were stained with LIVE/DEAD Fixable Violet Dead Cell kit and anti-CD16/CD32 was added to block Fc receptors to reduce non-specific binding before addition of the antibodies listed in the Key Resources Table. Stained cells were resuspended in PBS + 5% FBS + 10 mM HEPES before sorting with a FACSAria II (BD Biosciences). Alveolar Macrophages (AM) were identified as live singlets that were $CD45^+CD3^-CD19^-Ly6G^-CD11c^+SiglecF^+$ and Monocyte Derived Macrophages (MDM) were identified as live singlets that were $CD45^+CD3^-CD19^-Ly6G^-SiglecF^-MHC\text{-}II^+CD64^+$ (and see Figure III.22 for gating). Sorted AM and MDM were kept on ice in RPMI 1640 + 10% FBS before plating in Agilent XFp miniplates and subsequent XFp Seahorse analysis.

**Infections and stimulations**

*BMDM infection in vitro +/- IFNβ treatment*

An aliquot of H37Rv (a virulent strain of lineage 4 Mtb) was thawed and cultured at 37 ºC in 7H9 media supplemented with 0.2% glycerol, 0.1% tween-80, and 10% OADC at 37ºC and ambient $CO_2$. Cultures were used during log-phase growth, (i.e. when the optical density at 600nm (OD600) was between 0.1 and 0.3). The final concentration of bacteria was calculated using the OD600 and the appropriate number of bacteria was separated from the stock culture and centrifuged at 3000-4000 g for 10 minutes before resuspension in BMDM media at the appropriate concentration for the desired MOI. For some experiments, the resuspended H37Rv was heated to 99 ºC for 10 minutes and then cooled to RT for at least 5 minutes to produce heat killed (HK) H37Rv. Mock infections were performed with fresh BMDM media with no bacteria added. The bacteria were added to the macrophages for 3-4 hours at 37 ºC, 5% $CO_2$ before the macrophages were washed three times with pre-warmed BMDM media to remove extracellular

bacteria and fresh media was added. Antibiotics were not used at any step of this process. In some experiments, 500 U/mL IFNβ was added to BMDM cultures 4 hours before infection and included with the bacteria during the 3-4 hour infection. No IFNβ was added after the wash at the end of the infection incubation.

*TLR ligand stimulation*

Frozen stocks of PAM3Csk4 were thawed and sonicated for 5 minutes before dilution in BMDM media. The diluted stimuli were again sonicated for 5 minutes before addition to BMDM cultures for a final concentration of 300 ng/mL for PAM3Csk4.

*Mouse aerosol infection*

For high-dose (~1000 to 2000 CFU) infections, mice were enclosed in an aerosol infection chamber (Glas-Col) and frozen stocks of bacteria were thawed and placed inside the associated nebulizer. To determine the infectious dose, three mice in each infection were sacrificed after the aerosolization was complete. The whole lung was homogenized in 0.05% Tween-80 in PBS with a gentleMACS Tissue Dissociator (Miltenyi Biotec) and serial dilutions were plated onto 7H10 plates for CFU enumeration, as described previously (Rothchild et al., 2020).

**Lactate dehydrogenase assays**

Cell death was calculated by measuring concentrations of lactate dehydrogenase (LDH) present in the supernatants collected from BMDM cultures. If the experiment included live Mtb, the supernatants were filtered twice through 0.2 μm filters (Pall Corporation) before removal from the BSL-3 suite. LDH concentrations were determined with the CyQUANT LDH Cytotoxicity Assay (Thermo Fisher Scientific) according to manufacturer's instructions. Briefly, samples were mixed with the reconstituted reaction mixture for 30 minutes in the dark at room temperature before the stop solution was added. The absorbance at 750 nm (background) was subtracted from the absorbance at 490 nm (signal) and normalized to the background-

subtracted 490 absorbance of dedicated untreated wells within each experiment that had been lysed at each timepoint with the provided 10X lysis buffer.

**Metabolic Flux Analysis:**

*XFp*

An XFp analyzer (Agilent) was used to determine oxygen consumption rate (OCR) and extracellular acidification rate (ECAR) of macrophages in experiments including live H37Rv Mtb. BMDM were plated at 25,000 cells/well of an XFp miniplate (Agilent) on day 6 of differentiation and rested overnight. After sorting, MDM and AM were plated at 60,000 cells/well and rested overnight. The XFp Mito Stress Test Kit or XFp Glycolysis Stress Test Kit (Agilent) was run according to the manufacturer's instructions. Briefly, the XFp cartridge was hydrated in sterile $H_2O$ overnight and then the $H_2O$ was replaced with XF Calibrant (Agilent) for 1 hour before calibration on the XFp analyzer. Macrophage culture media was removed and replaced with XF RPMI pH 7.4 (Agilent) supplemented with just 2 mM L-glutamine (Glycolysis Stress Test) or an additional 1mM sodium pyruvate and 10 mM glucose (Mito Stress Test) for 1 hour before a second wash with the same media immediately before loading in the analyzer. The kit compounds were resuspended in supplemented XF media and loaded into the cartridge injection ports such that the final concentrations of the compounds in each well were oligomycin 5 μM, FCCP 3 μM, and Rotenone and Antimycin both at 1 μM (Mito Stress Test) or glucose 10 mM, oligomycin 5 μM, 2-deoxyglucose 50 mM (Glycolysis Stress Test).

*Derivation of mitochondrial parameters*

Figure III.1 shows representative OCR measurements from a mitochondrial stress test described above. The non-mitochondrial oxygen consumption (NMOC) is defined as the minimum OCR after Rot/AA injection. Basal mitochondrial respiration is defined as the last measurement before oligomycin injection minus the NMOC. The OCR dedicated to ATP production is defined as the last OCR measured before oligomycin injection minus the minimum

OCR after oligomycin injection. The proton leak is the minimum OCR after oligomycin injection minus the NMOC. Maximal mitochondrial respiration is defined as the maximum OCR after FCCP injection minus the NMOC. The spare respiratory capacity (SRC) is defined as maximal mitochondrial respiration minus basal mitochondrial respiration.

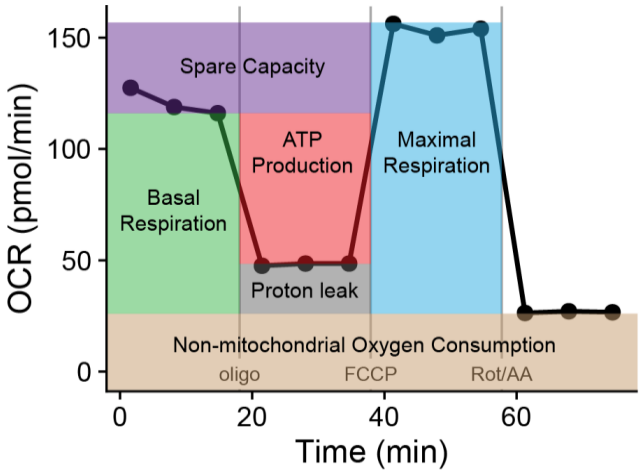


**Figure III.1 Derivation of mitochondrial parameters**

*Derivation of glycolytic parameters*

Figure III.2 shows representative ECAR measurements from a glycolytic stress test described above. Non-glycolytic acidification (NGA) is defined as the last ECAR prior to injection of glucose. Basal glycolysis is defined as the maximum ECAR before oligomycin injection minus NGA. Maximum glycolytic capacity is defined as the maximum rate after oligomycin injection minus NGA. Glycolytic reserve is defined as the glycolytic capacity minus basal glycolysis.

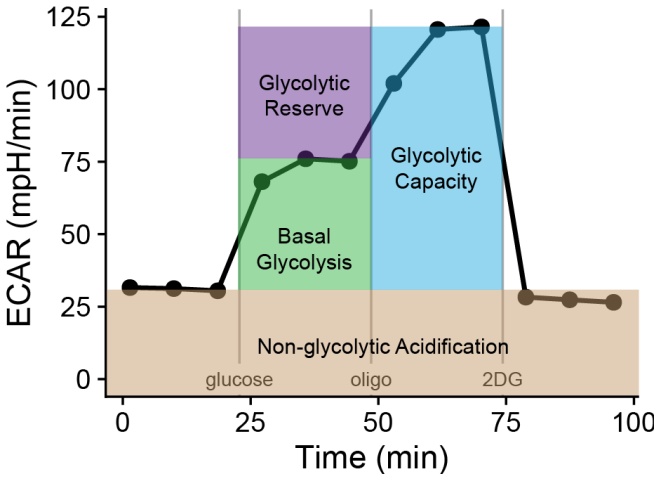


**Figure III.2 Derivation of glycolytic parameters from glycolytic stress test**

Because the initial injections of the mitochondrial stress test match the glycolytic stress test, approximations of glycolytic parameters can be derived from ECAR measurements taken during the mitochondrial stress test (Figure III.3 shows representative ECAR measurements from a mitochondrial stress test). Although the NGA cannot be calculated, basal glycolysis can be defined as the maximum ECAR before addition of oligomycin. Maximal glycolytic capacity is defined as the maximal ECAR after either addition of oligomycin or FCCP. Glycolytic reserve is still defined as maximal glycolytic capacity minus basal glycolysis.

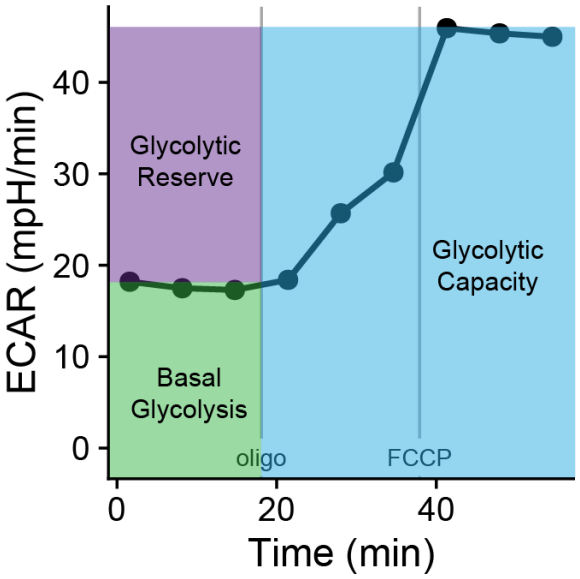


**Figure III.3 Derivation of glycolytic parameters from mitochondrial stress test**

**Mitochondrial Flow Cytometry**

*Mitochondrial membrane potential*

After 6 days of differentiation, BMDM were replated at 400,000 cells/well of a non-TC treated 24 well dish in BMDM media without p/s. The culture media was removed, and macrophages were washed once with pre-warmed staining media (RPMI 1640 without phenol red + 10 mM HEPES buffer) before incubation with 100 nM TMRM and 100 nM MitoTracker Green (MTG) in staining media for 30 minutes at 37 ºC, 5% $CO_2$. The staining media was removed, and macrophages were lifted off the culture plates using gentle pipetting after a 5-

minute incubation at 4 ºC in ice-cold PBS + 2 mM EDTA. The macrophages were centrifuged in 96-well U-bottom plates at 300g for 6 minutes at 4 ºC before staining with the LIVE/DEAD Fixable Violet Dead cell kit for 8 minutes. This was washed off and the cells were resuspended in PBS + 5% FBS before analysis on an LSR II cytometer (BD biosciences) using the following details (excitation laser; emission bandwidth filter): LIVE/DEAD (405 nm; 450/50), MTG (488 nm; 515/20), TMRM (532 nm; 575/25). Events were first gated for constant flow rate using time and then for singlets and FSC/SSC to gate out debris before selecting only live cells based on LIVE/DEAD exclusion. The ratio of TMRM/MTG was calculated for each live cell to account for total mitochondrial content and reported as the mitochondrial membrane potential ($\Delta\psi_m$).

*Mitochondrial reactive oxygen species*

Analysis of mitochondrial reactive oxygen species (mROS) used the above protocol with the following adjustments. Staining was done with 2.5 µM MitoSOX Red (MSR) in staining media for 10 minutes at 37 ºC, 5% $CO_2$. After washing off the LIVE/DEAD stain, the macrophages were fixed with 2% paraformaldehyde in PBS for 1 hour at room temperature before resuspension in PBS + 5% FBS and analysis on an LSR II (BD biosciences) using the following laser;filter combinations: LIVE/DEAD (405 nm; 450/50), MSR (405 nm; 585/42). Live non-debris singlets were analyzed for fluorescence in the MSR channel to quantify mROS. Excitation of MSR at 405 nm more specifically measures mitochondrial superoxide production by reducing the influence of cytosolic hydrogen peroxide (Robinson et al., 2006).

*Cell count*

Since all mitochondrial flow cytometry was acquired at a constant flow rate using a 96-well high-throughput system, relative cell numbers in each sample could be quantified. The number of live singlet cells collected during a stable 10 second flow rate (gating on time) was calculated for each sample and normalized to untreated, mock-infected conditions for each experiment.

**Mitochondrial microscopy**

After 6 days of differentiation, BMDM were replated at 200,000 cells/well of a glass-bottom TC-treated 24 well dish (Greiner Bio-One). After infection, culture media was removed, and the cells were washed with pre-warmed staining media before adding 100 nM TMRM and 100 nM MTG diluted in staining media. After 30 minutes at 37 ºC, 5% $CO_2$, micrographs were taken with a Ti-E inverted microscope (Nikon Instruments Inc.) using a 20X objective and the following filter cubes (excitation bandwidth filter; dichroic mirror; emission filter): TMRM (545/30; 570; 620/60) and MTG (470/40; 500; 535/50). For quantification of TMRM fluorescence, raw images in both channels first had background subtraction done in Fiji (ImageJ) (Schindelin et al., 2012) using the rolling ball algorithm (radius 40 pixels). Background subtracted images were then analyzed using CellProfiler (McQuin et al., 2018): Images were masked based on mitochondria identified using global RobustBackground thresholding in both the TMRM and MTG channels. TMRM fluorescence was quantified in the masked image to quantify $\Delta\psi_m$.

**Gene expression**

*RNA preparation*

After 6 days of differentiation, BMDM were replated at 400,000 cells/well of a TC-treated 24 well dish. After the indicated amount of time of infection or stimulation, culture media was removed, and the cells were washed once with PBS before being lysed in TRIzol for 5 minutes at room temperature and frozen at -80 ºC. TRIzol was thawed and total RNA extracted using Direct-zol-96 extraction kits according to manufacturer's instruction, including an on-column DNase treatment and elution with 25 µL $H_2O$. RNA integrity was confirmed using 260/280 and 260/230 nm ratios measured by a Nanodrop One Microvolume UV-Vis Spectrophotometer (Thermo Fisher Scientific).

*Quantitative reverse transcription PCR*

RNA (500 – 1000 ng) was converted to cDNA using the RNA to cDNA EcoDry™ Premix (Oligo dT) according to manufacturer instructions. RT-qPCR reactions were carried out with 15-20 ng cDNA using TaqMan primer probes and the TaqMan Fast Universal PCR Master Mix (Thermo Fisher Scientific) in the QuantStudio 5 Real-Time PCR System (Applied Biosystems). Data were normalized to *Eef1a1* expression in individual samples.

*RNA-seq*

Two different batches of RNA sequencing were done. The first batch was sent to BGI (bgi.com) for library prep and sequencing. The BV01 protocol was used for library prep and then the libraries were sequenced on a DNBSEQ-G400. The second batch was sent to Psomagen (Psomagen.com) for library preparation and sequencing. The Illumina TruSeq stranded kit was used for library prep and then the libraries were sequenced on an Illumina NovaSeq6000 S4. Both sequencing runs produced 100 bp paired end reads. Fastq files from both batches were processed in parallel (described in section on Quantification). The RNA sequencing data generated during this study are available in GEO accession number GSE162620. Additional data supporting the current study are available from the corresponding author on request.

**RNA-seq analysis**

*Initial processing and differential expression*

Initial quality assessment was performed with FastQC version 0.11.9 before read ends consisting of 50 or more of the same nucleotide were removed. Reads were aligned to the mouse + Mtb genome (NCBI GRCm38 mm10 + H37Rv Mtb) using GSNAP version 2018-07-04 (Wu and Nacu, 2010). Feature counts were extracted using the featureCounts software (Liao et al., 2014), distributed as part of the Subread package v1.5.2. Genes were filtered to only include those detected in at least 2 samples. Normalization (to find counts-per-million (CPM) for each gene) and differential analysis of gene expression was calculated using edgeR version 3.26.8.

The threshold for significance for differential expression was set at as $|\log_2 FC| > 1$ and FDR < 0.001.

*Principal component analysis*

Input genes were restricted to those that were differentially expressed when directly comparing the conditions included in the analysis. Normalized CPM values for these genes were input into the prcomp function in R for visualization and identification of the proportion of variance explained by each principal component.

*Clustering*

The union of the sets of differentially expressed genes in any of the 3 comparisons (HK H37Rv vs Mock, Live H37Rv vs Mock, and IFNβ vs untreated) across the two timepoints (4 and 24 hours post infection) in WT BMDM (a total of 6337 genes) were clustered using the K-means clustering algorithm described in (Hartigan and Wong, 1979) and implemented in R.

*Gene set enrichment*

The 1411 genes in cluster 4 were tested for enrichment in the Hallmark gene sets of the Molecular Signatures Database (MSigDB) (Liberzon et al., 2015) using a hypergeometric test implemented in the hypeR R package (Federico and Monti, 2020) with the number of protein coding genes (22,519) in the GRCm38 genome build as the background set.

**Statistical information**

Data were analyzed using R. Data are either presented as individual technical replicates with a horizonal bar representing the mean, or as a point representing the mean with SEM error bars. Statistical significance was assessed with a Student's t-test. Precise values of n and numbers of independent experiments are indicated in figure legends.

## Results

### Live *Mycobacterium tuberculosis* decreases bone marrow derived macrophage metabolism more than heat killed

Live H37Rv infection dramatically decreases OCR in BMDM 24 hours after infection, while HK H37Rv has little effect at the same multiplicity of infection (MOI) (Figure III.4A,B and see Figure III.1 for derivation of parameters). The decrease in mitochondrial respiration in BMDM is accompanied by hallmarks of mitochondrial stress. After 24 hours of infection, live H37Rv dissipates $\Delta\psi_m$ to a greater extent than HK H37Rv (Figure III.4C,D). In addition, mROS accumulates after infection with live H37Rv more than after HK (Figure III.4E). Accumulation of mROS begins as early as 4 hours after infection and continues to increase over the first 48 hours in BMDM infected with live H37Rv (Figure III.4F). Live H37Rv causes minimal (~10%) cell death after 24 hours (Figure III.4G) (Zhang et al., 2021), indicating that decreased OCR is unlikely to result from increased cytotoxicity. Furthermore, the single-cell measurements of $\Delta\psi_m$ and mROS confirm that live H37Rv specifically alters mitochondrial physiology in viable cells.

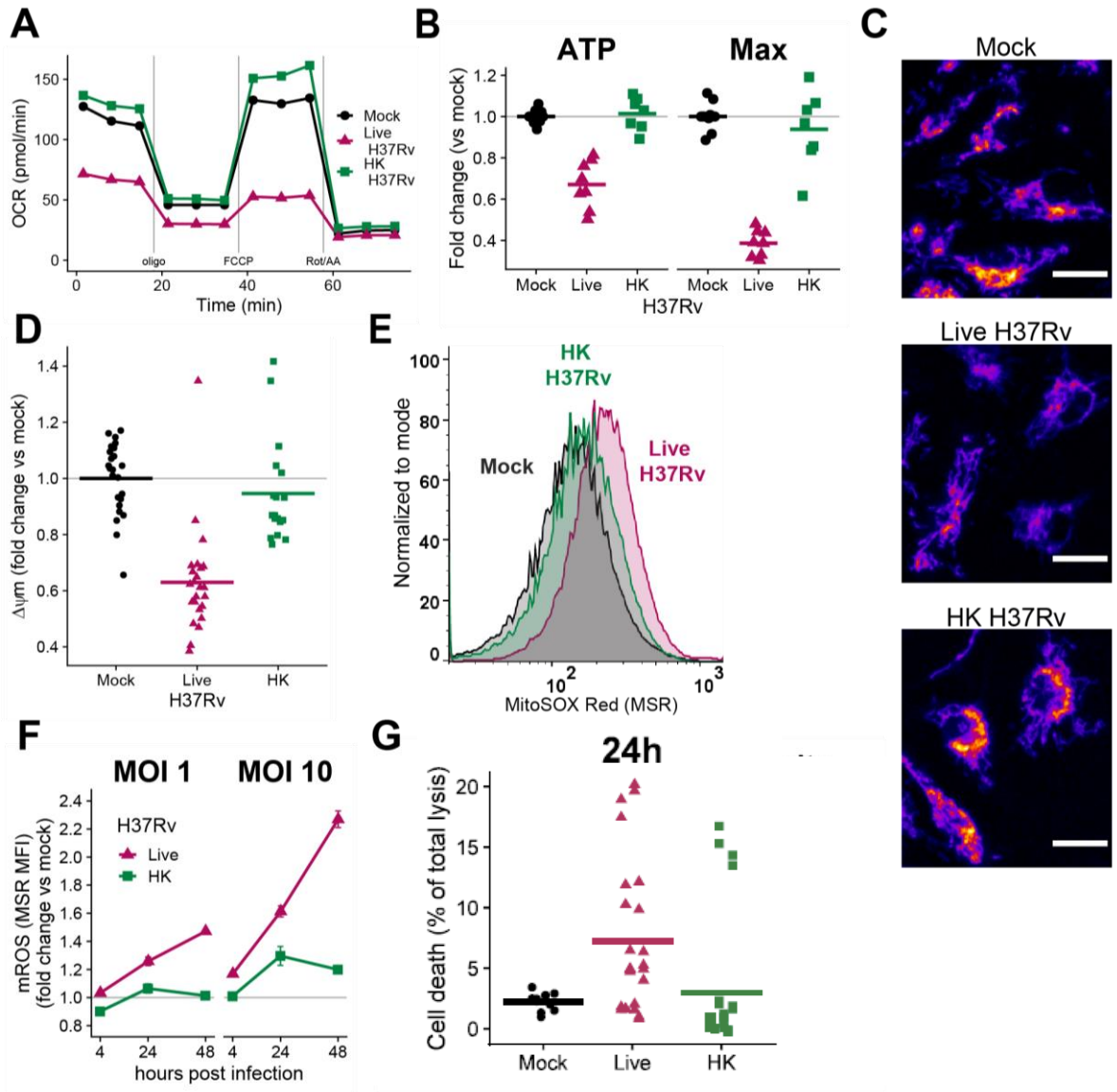


**Figure III.4 Live H37Rv decreases BMDM mitochondrial metabolism more than HK H37Rv**

(A) Oxygen consumption rate (OCR) in WT BMDMs 24 hours after mock infection or infection with live H37Rv or HK H37Rv at an MOI of 10. A single representative plate is shown.

(B) Quantification of mitochondrial parameters derived from (A). The OCR dedicated to ATP production (ATP) or at maximal respiration (Max) was normalized to mock infection controls on each plate. Each dot represents a single well and bars represent the mean. Data from 8 plates across 3 independent experiments.

(C) Representative 20x images of BMDM either mock infected (top) or infected with live (middle) or HK (bottom) H37Rv (MOI 10) and stained 24 hours later with the mitochondrial membrane potential ($\Delta\psi_m$) sensitive dye TMRM. TMRM intensity depicted with the “Fire” LUT from Fiji (Schindelin et al., 2012; Schneider et al., 2012). Scale bar =15 μm.

(D) Quantification of $\Delta\psi_m$ derived from (C). The TMRM median fluorescence intensity (MFI) for each field of view was measured in CellProfiler (McQuin et al., 2018) and normalized to mock infected wells. Each dot represents a single field of view collected across two independent experiments.

(E) Representative histograms of MitoSOX Red (MSR) fluorescence quantified with flow cytometry to measure mROS in BMDM either mock infected or infected with MOI 10 of live H37Rv or HK H37Rv for 24 hours.

(F) Quantification of mROS derived from (E). MSR MFI in each condition was normalized to mock infected controls at each timepoint. Mean for 4 technical replicates ± SEM shown for a representative experiment of 3 independent experiments.

(G) Cell death in WT BMDM either mock infected or infected with live H37Rv or HK H37Rv at an MOI 10 for 24 hours was calculated using an LDH assay on culture supernatants.

Interestingly—and in agreement with more recent reports—BMDM infected with live H37Rv do not increase glycolysis to compensate for the decreased mitochondrial respiration, as seen with classical inflammatory stimuli (e.g. LPS) (O'Neill et al., 2016); live H37Rv infection decreases BMDM glycolysis, especially by limiting glycolytic capacity (Figure III.5).

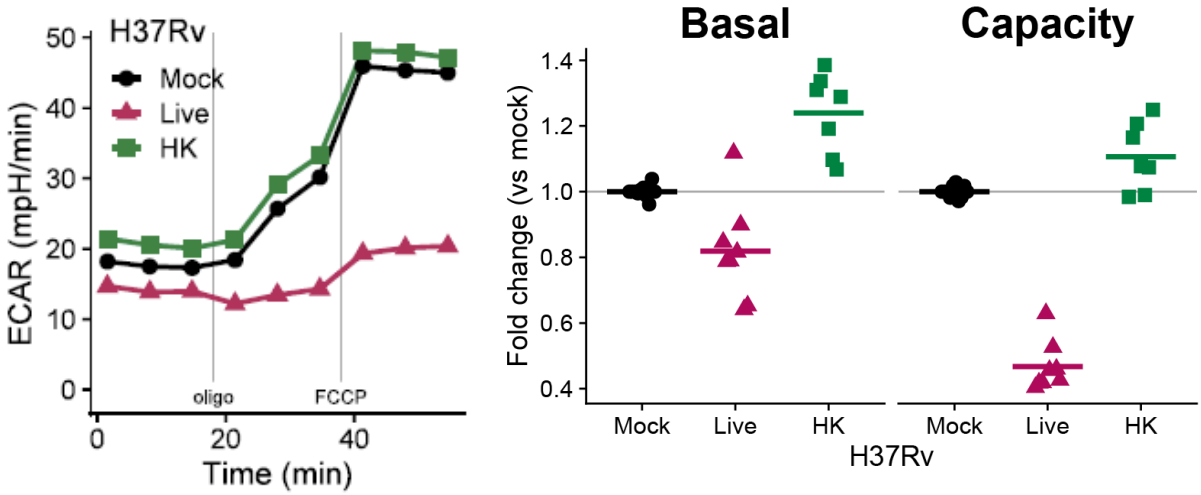


**Figure III.5 Live H37Rv restrains BMDM glycolysis more than HK H37Rv**
(left) ECAR of WT BMDM either mock infected or infected with live H37Rv or HK H37Rv at an MOI 10 for 24 hours for a single representative plate. (right) Fold change in basal glycolysis or glycolytic capacity was calculated relative to mock infected controls on each plate. Each dot represents a well and bars represent the mean from 8 plates across 3 independent experiments.

### Type I interferon signaling dominates the BMDM transcriptional response to live Mtb and correlates with metabolic changes

Live Mtb could rewire macrophage metabolism either indirectly by engaging macrophage signaling pathways distinct from those engaged by HK Mtb or directly by secreting effector molecules that target metabolic pathways. Since TLRs recognize mycobacterial components (Mortaz et al., 2015), drastically alter macrophage metabolism (O'Neill et al., 2016), and induce mROS (Figure III.6) (West et al., 2011), we first tested their involvement by measuring mROS in BMDM lacking key TLR signaling adaptors (MyD88-TRIF double KO). TLR signaling does not explain the induction of mitochondrial stress; mROS accumulation after live H37Rv infection is TLR-independent, and—like in WT BMDM—live H37Rv induces more mROS than HK in MyD88-TRIF double KO BMDM across many MOI (Figure III.6).

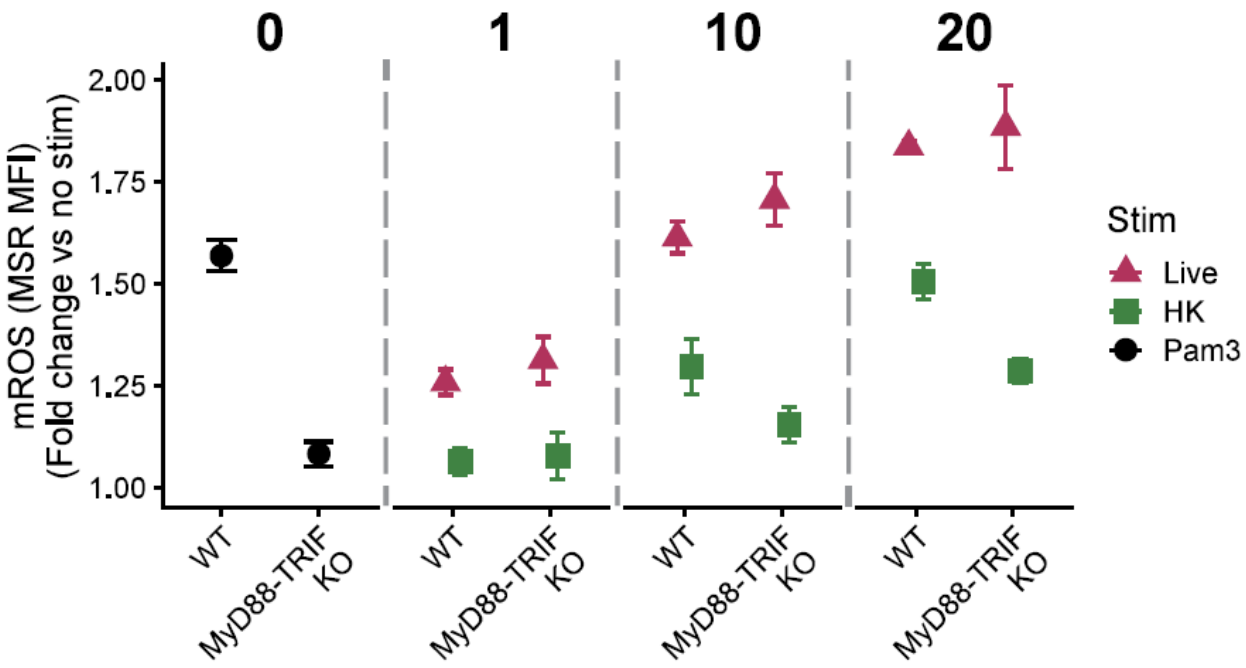


**Figure III.6 Induction of mROS by live H37Rv is independent of TLR signaling**
Mitochondrial reactive oxygen species (mROS) quantified by flow cytometric measurement of MitoSOX Red (MSR) fluorescence. WT or MyD88-Trif double KO BMDM were infected with either live H37Rv or heat killed (HK) H37Rv for 24 hours at the MOI indicated at top of graph. Pam3CSK4 (TLR2/TLR1 ligand; 300 ng/mL) was used as a control for MyD88-TRIF ablation. Points represent the mean for four technical replicates and error bars the SEM for one of two independent experiments.

To interrogate the myriad signaling pathways that could explain the metabolic changes during infection, we performed global RNA sequencing on WT BMDM at an early (4h) and late (24h) timepoint after mock infection or infection with live or HK Mtb. The transcriptional response to live and HK Mtb diverges early: BMDM infected with live H37Rv for 4 hours differentially express (DE) 1717 genes compared to BMDM infected with HK H37Rv ($|\log_2(FC)| > 1$, FDR < 0.001) (Figure III.7). Although canonical inflammatory genes like *Nos2* and *Il12b* are robustly induced by both live and HK H37Rv, a subset of genes are only upregulated by live H37Rv (Figure III.7). Five members of the type I IFN family—including *Ifnb1*, the gene encoding IFNβ—comprise the most differentially expressed genes in this subset (Figure III.7). We validated that live H37Rv induces more *Ifnb1* and downstream IFN signaling (*Isg15* expression) than HK H37Rv using RT-qPCR (Figure III.8).

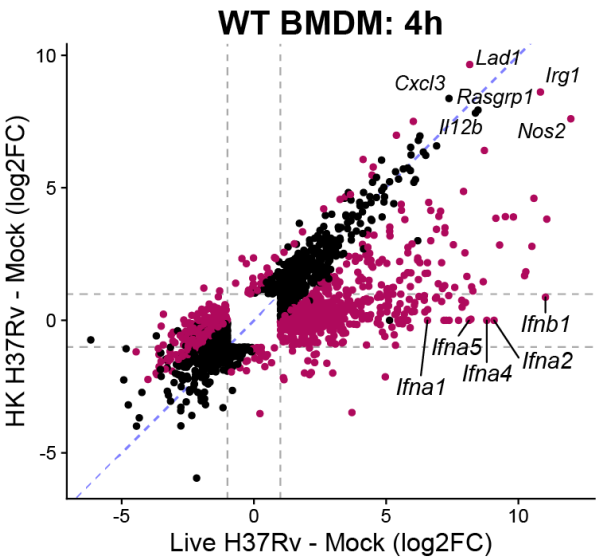


**Figure III.7 The BMDM transcriptional responses to live and HK H37Rv diverge early**
Scatter plot of $log_2$FC values of the 2210 genes differentially expressed (DE) (FDR <0.001, |log2FC| > 1; grey dotted lines) across both comparisons in WT BMDM. Magenta points: genes significantly DE directly comparing the infection conditions (live H37Rv infected vs HK H37Rv infected).

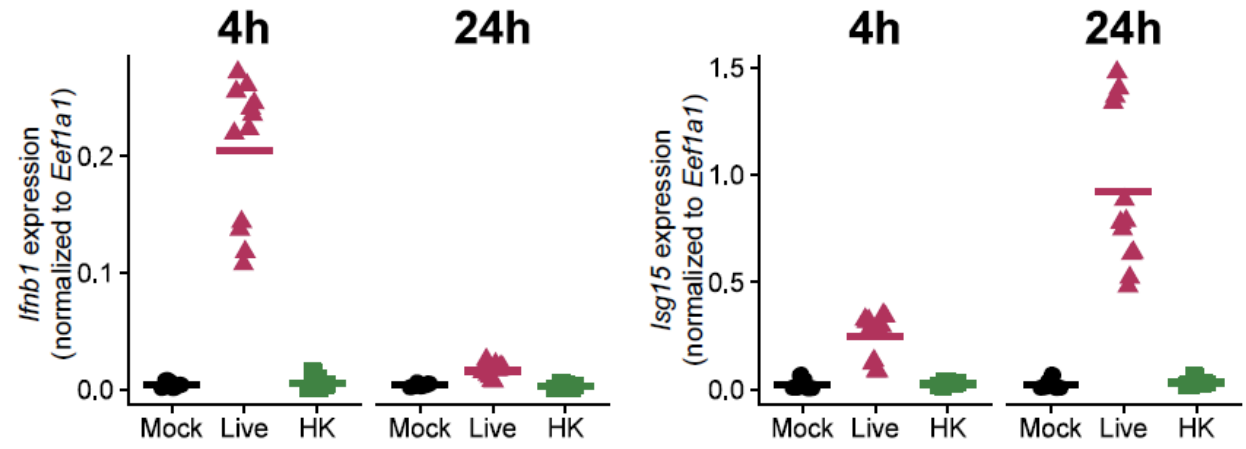


**Figure III.8 Validating differential induction of type I IFN and downstream signaling in BMDM**
Expression of *Ifnb1* (left) and *Isg15* (right) was measured with RT-qPCR in WT BMDM either mock infected or infected with live H37Rv or HK H37Rv at an MOI 10 for the indicated number of hours. Expression was normalized to the housekeeping gene *Eef1a1*.

Although it is known that the induction of type I IFN by Mtb requires active virulence processes (Collins et al., 2015; Manzanillo et al., 2012; Wassermann et al., 2015; Watson et al., 2015), to the best of our knowledge, the transcriptional response in IFNAR KO cells after infection with virulent Mtb has only been characterized in lung homogenates (Dorhoi et al., 2014), obfuscating the response of any single cell type. To assess how the induction of type I IFN contributes to the differential transcriptional response to live and HK Mtb, we repeated the RNA-seq analysis in BMDM generated from mice lacking IFNAR. IFNAR KO BMDM respond

remarkably similarly to live and HK H37Rv: at 24 hours, IFNAR KO BMDM differentially express only 250 genes comparing live H37Rv to HK H37Rv conditions, while WT BMDM differentially express 2554 genes at the same timepoint (Figure III.9). *Ifnb1* itself is still induced in IFNAR KO BMDM, and the remaining most differentially expressed genes are primarily members of the IFIT gene family (Figure III.9), which can be upregulated independently of type I IFN signaling (Diamond and Farzan, 2013).

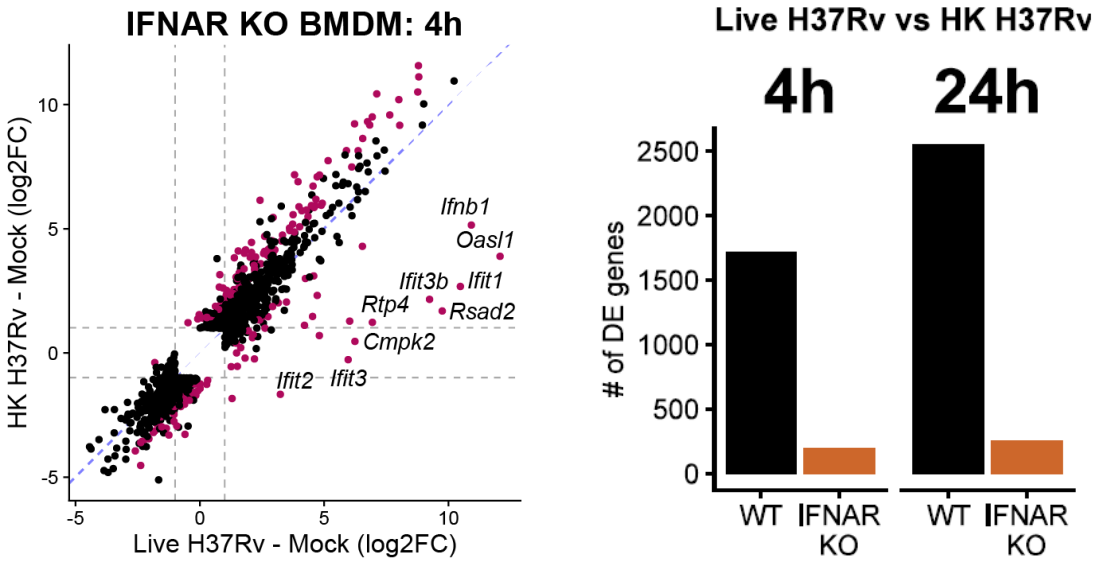


**Figure III.9 Type I IFN signaling required for differential response to live and HK H37Rv**
(left) Scatter plot of log2FC values of the 1712 genes differentially expressed (DE) (FDR <0.001, |log2FC| > 1; grey dotted lines) across both comparisons in IFNAR KO BMDM. Magenta points: genes significantly DE directly comparing the infection conditions (live H37Rv infected vs HK H37Rv infected). (right) The number of DE genes (FDR <0.001, |log2FC| > 1) identified by edgeR analysis of RNA-seq comparing infection conditions (live H37Rv vs HK H37Rv; MOI 10) at 4 or 24 hours post infection in WT or IFNAR KO BMDM.

We next performed dimensionality reduction using principal component analysis (PCA) to confirm that IFNAR KO dampens the response to live H37Rv rather than augmenting the response to HK H37Rv. The transcriptional response of both genotypes to HK H37Rv cluster together (Figure III.10), verifying that IFNAR signaling plays little role in the BMDM response to HK H37Rv. Strikingly, the transcriptional response of IFNAR KO BMDM to live H37Rv clusters together with the HK response (Figure III.10), suggesting that type I IFN signaling dominates the transcriptional response of BMDM to live Mtb. If this is indeed the case, then the addition of exogenous type I IFN should make the transcriptional response to HK H37Rv approximate live

H37Rv. Consistent with a critical role for type I IFN signaling, the transcriptional response of WT BMDM to HK H37Rv in the presence of exogenous IFNβ more closely clusters with the response to live H37Rv than the response to HK H37Rv at 24 hours after stimulation (Figure III.10).

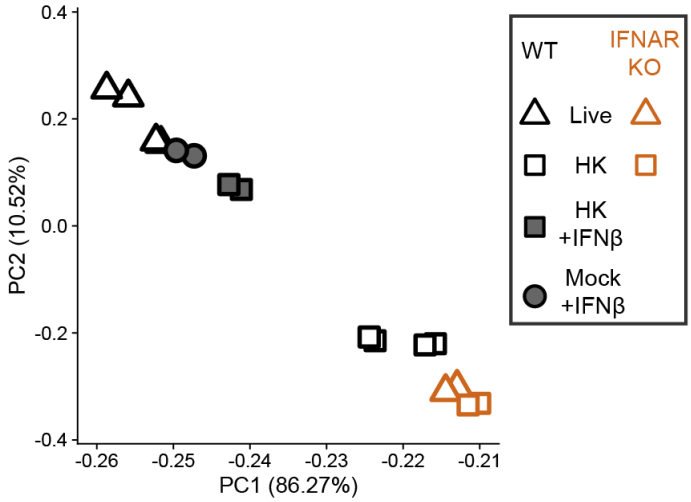


**Figure III.10 Type I IFN signaling is required for robust response to live H37Rv** Principal component analysis of WT or IFNAR KO BMDM at 24 hours post infection with live H37Rv or HK H37Rv at 10 MOI. WT BMDM were either left untreated or treated with 500 U/mL IFNβ. The percent of variance explained by the top two principal components is indicated.

Remarkably, the transcriptional response to IFNβ alone resembles the response to live H37Rv (Figure III.10). To explore this relationship with more granularity, we performed K-means clustering on the union of the sets of genes differentially expressed after stimulation with HK, live H37Rv, or IFNβ alone compared to mock stimulation. Overall, both the qualitative trends and the quantitative fold changes induced by IFNβ and live H37Rv are remarkably similar across the >6000 genes used in the clustering, corroborating the PCA analyses (Figure III.11).

The clustering allowed us to query whether transcriptional regulation correlates with the metabolic changes observed during infection with live H37Rv. The transcriptional pattern of genes in cluster 4 mirrors the metabolic response of BMDM: a robust downregulation at late timepoints after live H37Rv infection but not after HK H37Rv (Figure III.11). To identify the pathways represented by this cluster, we performed hypergeometric enrichment on all Hallmark gene sets from the MSigDB (Liberzon et al., 2015; Subramanian et al., 2005). Five of the top ten gene sets represent nutrient transporters, central carbon metabolism, or ROS metabolism (Figure III.11).

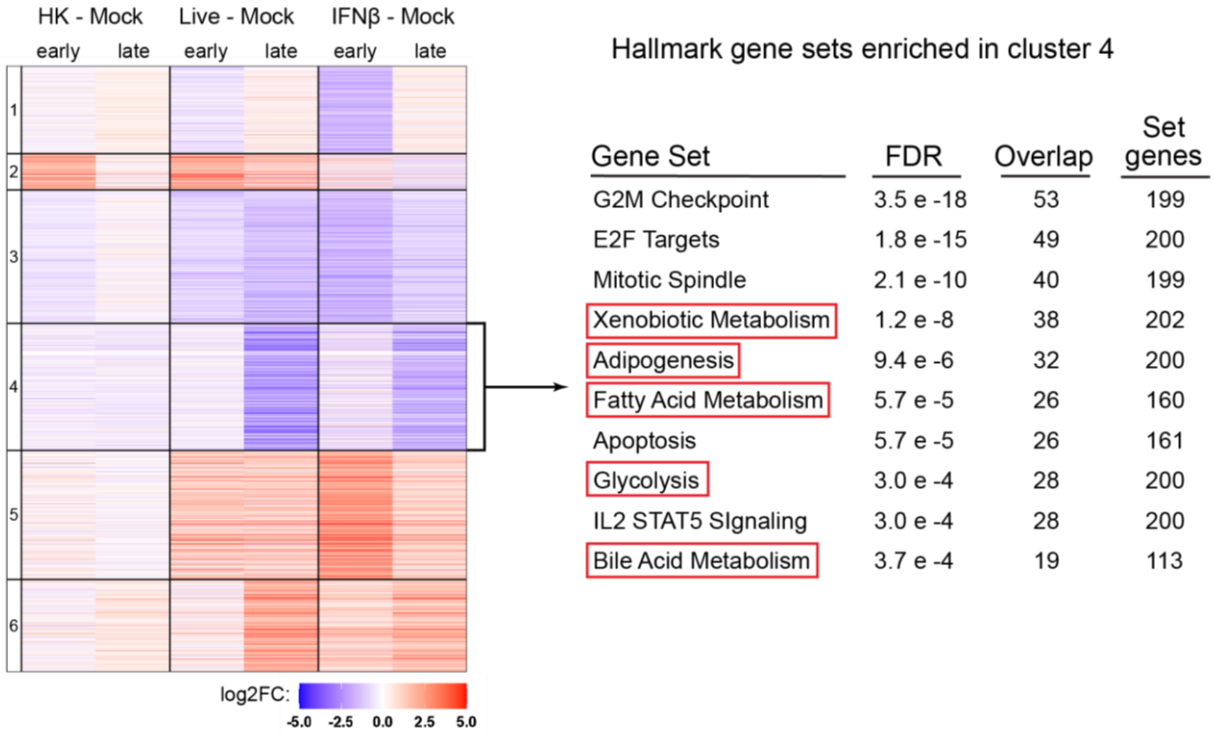


**Figure III.11 Metabolic reprogramming characterizes the response to live H37Rv and IFNβ**
(left) Heatmap showing the cluster number (far left) and $\log_2$FC of the 6337 genes differentially expressed in any of the 6 comparisons in WT BMDMs.
(right) The 1411 genes from cluster 4 were tested for enrichment in the Hallmark gene sets from MSigDB (Liberzon et al., 2015; Subramanian et al., 2005) using a hypergeometric test for overlap. The 10 gene sets with the smallest FDR are shown.

### Type I interferon controls the metabolic response of macrophages to Mycobacterium tuberculosis infection *in vitro* and *in vivo*

Next, we tested the causal role of type I IFN signaling during Mtb infection. We reasoned that if type I IFN directly causes the metabolic changes during infection, IFNAR KO BMDM infected with live H37Rv should maintain the metabolic function of mock infected cells. Indeed, IFNAR KO BMDM infected with two MOIs of live H37Rv consume oxygen at rates indistinguishable from mock infected cells (Figure III.12A,B). This clearly contrasts with the profound reduction in OCR in WT BMDM during infection (especially at higher MOI) (Figure III.12A,B). The reduction in glycolysis during infection with live H37Rv requires IFNAR signaling as well; infected IFNAR KO BMDM actually have slightly increased glycolysis compared to mock infected conditions (Figure III.12C,D).

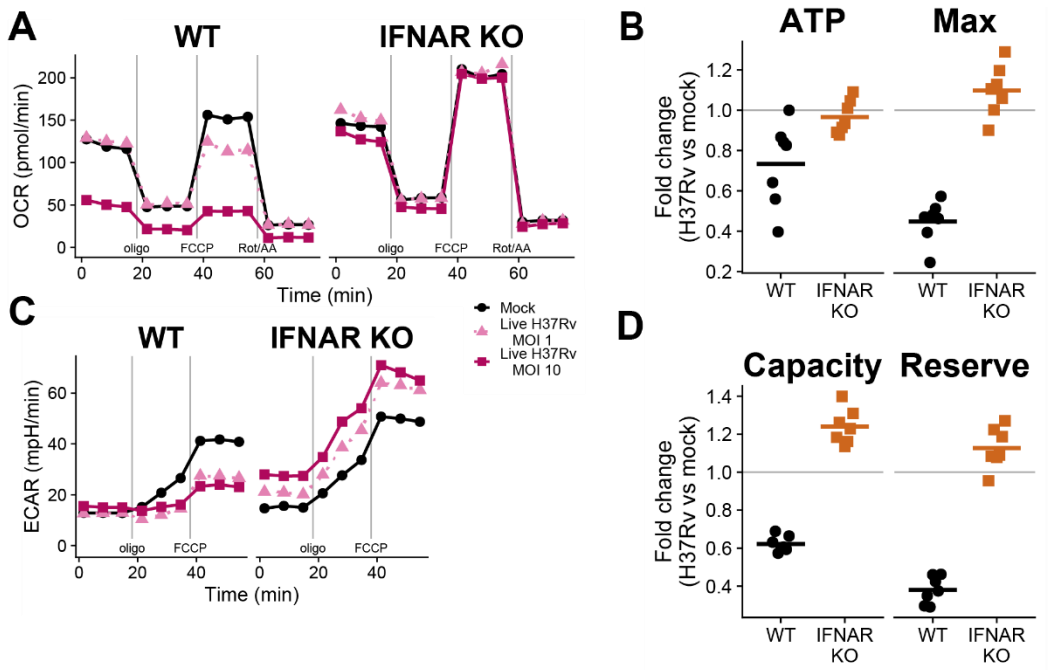


**Figure III.12 Type I IFN signaling controls the metabolic response of BMDM to live H37Rv**
(A) Oxygen consumption rate (OCR) of WT BMDMs (left) or IFNAR KO BMDMs (right) either mock infected or infected with live H37Rv at an MOI of 1 or 10 for 24 hours. A single representative plate is shown.
(B) Quantification of mitochondrial parameters in BMDM infected with live H37Rv (MOI 10) derived from (A). Each point represents a single well and the bar is the mean from 7 plates across two independent experiments.
(C) Extracellular acidification rate (ECAR) from the same conditions as in (A). A single representative plate is shown.
(D) Quantification of glycolytic parameters in BMDM infected with live H37Rv (MOI 10) derived from (C). Each point represents a single well and the bar is the mean from 7 plates across two independent experiments.

Other measures of mitochondrial physiology support the central role of type I IFN signaling. WT BMDM, but not IFNAR KO BMDM, downregulate all protein coding genes encoded on mtDNA after live H37Rv infection (Figure III.13A). Much lower amounts of mROS accumulate during infection with live H37Rv in IFNAR KO BMDM compared to WT (Figure III.13B). Furthermore, BMDM treated with exogenous IFNβ in addition to HK H37Rv accumulate mROS like BMDM infected with live H37Rv, and this requires intact IFNAR signaling, whereas exogenous IFNβ does not change mROS accumulation in WT BMDM infected with live H37Rv (Figure III.13B). Collectively, these data demonstrate that the differential induction of type I IFN by live and HK H37Rv accounts for the observed metabolic differences.

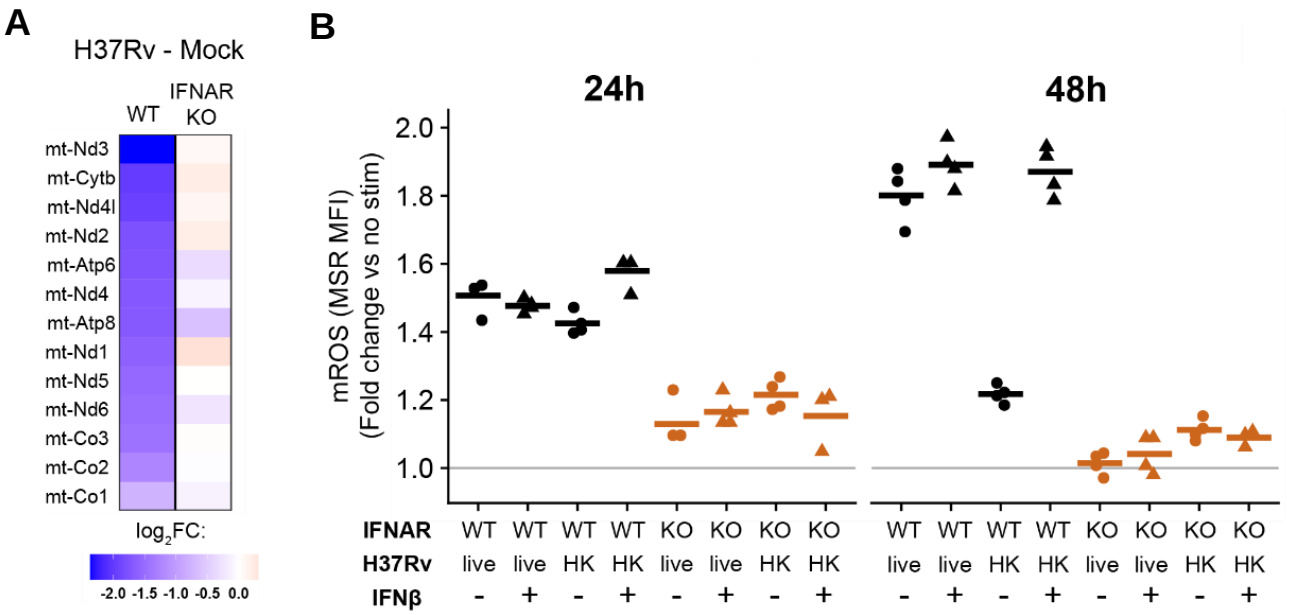


**Figure III.13 Other measures of mitochondrial physiology confirm central role of type I IFN during H37Rv infection**
(A) Log2FC in expression (RNA-seq) of the 13 protein coding genes encoded on mtDNA in WT or IFNAR KO BMDM infected with live H37Rv (MOI 10) for 24 hours compared to mock infected cells of each genotype.
(B) Mitochondrial reactive oxygen species (mROS) in WT or IFNAR KO BMDM infected with MOI 10 live H37Rv or HK H37Rv for either 24 or 48 hours. BMDM were either untreated or treated with 500 U/mL IFNβ. mROS measured with MitoSOX Red (MSR) MFI (flow cytometry) normalized to untreated, mock infected controls at each timepoint. A representative experiment of 2 independent experiments shown.

We next investigated whether type I IFN decreases macrophage metabolism *in vivo* during an Mtb infection. We infected WT and IFNAR KO mice with a high dose (~2000 CFU) of H37Rv via aerosol and 15 days later sorted AM and recruited inflammatory MDM from the lungs (see Figure III.22 for gating scheme) and performed extracellular flux analyses. As predicted from the *in vitro* BMDM data, both AM and MDM from infected IFNAR KO mice have elevated basal glycolysis and glycolytic capacity compared to those from WT mice (Figure III.14). In addition, IFNAR KO AM have modestly higher mitochondrial respiration than WT AM (Figure III.15). Although mitochondrial parameters are not consistently different between genotypes in MDMs (Figure III.15), this could be explained by recent reports (Huang et al., 2018; Pisu et al., 2020) and our own observations (data not shown) that MDM rely very little on OXPHOS,

especially compared to AM. Taken together, these results support a role for type I IFN in restraining macrophage metabolism during Mtb infections both *in vitro* and *in vivo*.

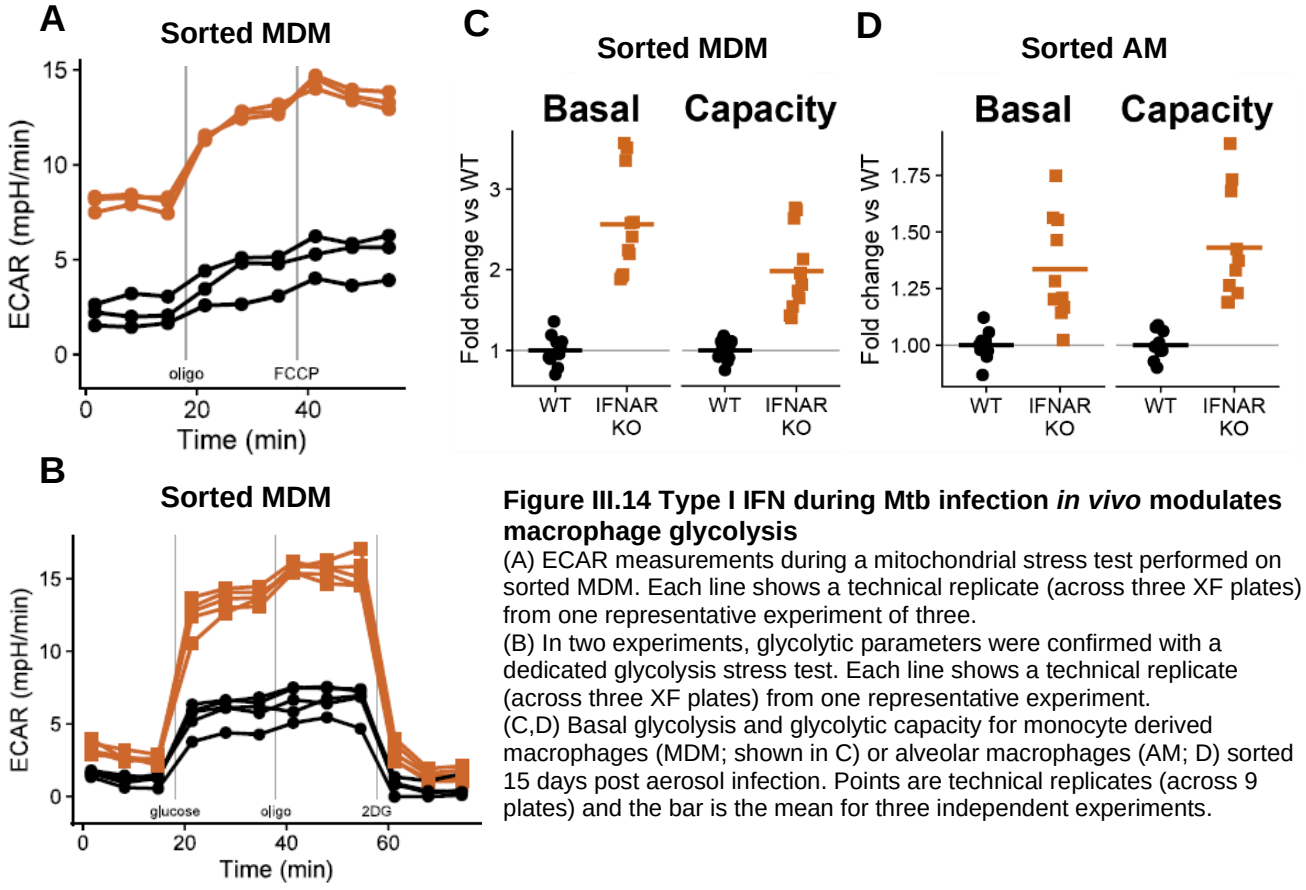


**Figure III.14 Type I IFN during Mtb infection *in vivo* modulates macrophage glycolysis**
(A) ECAR measurements during a mitochondrial stress test performed on sorted MDM. Each line shows a technical replicate (across three XF plates) from one representative experiment of three.
(B) In two experiments, glycolytic parameters were confirmed with a dedicated glycolysis stress test. Each line shows a technical replicate (across three XF plates) from one representative experiment.
(C,D) Basal glycolysis and glycolytic capacity for monocyte derived macrophages (MDM; shown in C) or alveolar macrophages (AM; D) sorted 15 days post aerosol infection. Points are technical replicates (across 9 plates) and the bar is the mean for three independent experiments.

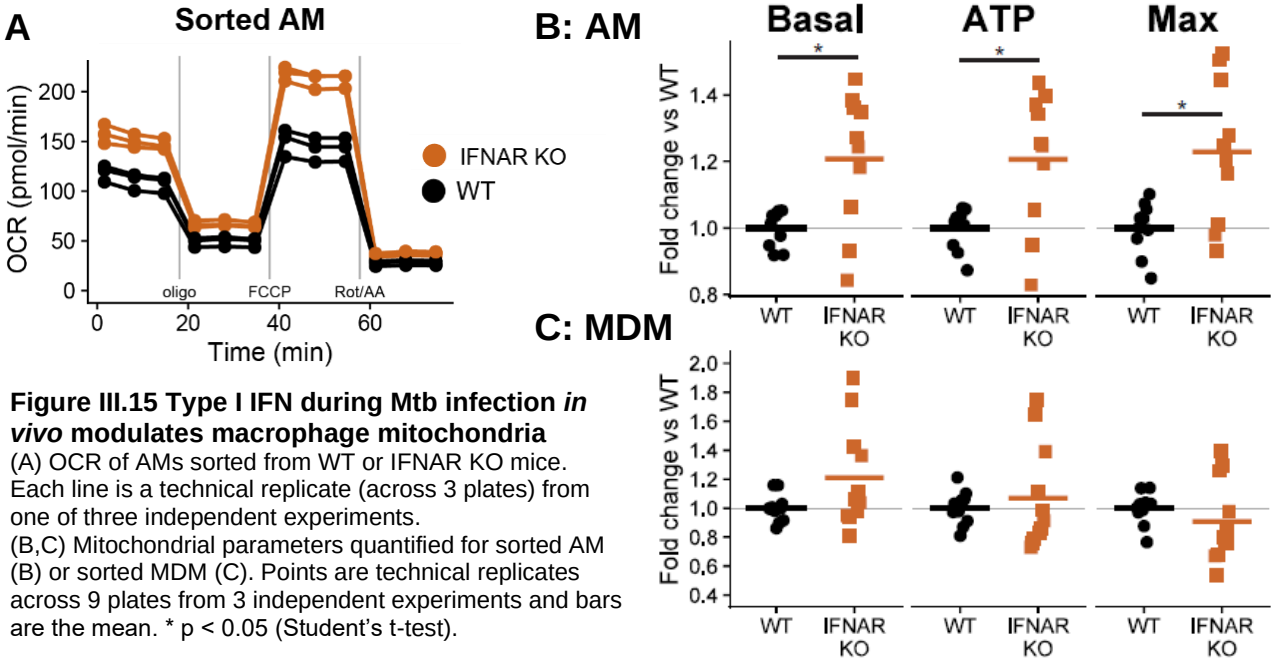


**Figure III.15 Type I IFN during Mtb infection *in vivo* modulates macrophage mitochondria**
(A) OCR of AMs sorted from WT or IFNAR KO mice. Each line is a technical replicate (across 3 plates) from one of three independent experiments.
(B,C) Mitochondrial parameters quantified for sorted AM (B) or sorted MDM (C). Points are technical replicates across 9 plates from 3 independent experiments and bars are the mean. * $p < 0.05$ (Student's t-test).

**STING signaling is upstream of mitochondrial damage during *Mycobacterium tuberculosis* infection**

Following Mtb infection, macrophages require the cytosolic DNA sensor cGAS and subsequent signaling through the protein STING to drive robust type I IFN production. Original models described mycobacterial DNA as the main cGAS ligand during infection (Collins et al., 2015; Wassermann et al., 2015; Watson et al., 2015), but a more recent report suggests that mtDNA released by Mtb-induced mitochondrial damage is the main activator of this pathway (Wiens and Ernst, 2016). The data presented above suggest that type I IFN itself can induce mitochondrial dysfunction in macrophages. This implies the intriguing possibility that during Mtb infection, type I IFN amplifies mitochondrial damage through a positive feedback loop (Figure III.16). We reasoned that BMDM lacking STING would allow us to test this model since they have impaired induction of type I IFN during live Mtb infection but retain the ability to signal through IFNAR. If type I IFN is only downstream of mitochondrial damage (as current models claim (Hopfner and Hornung, 2020; Weinberg et al., 2015; West et al., 2015)), then STING KO BMDM should have mitochondrial damage indistinguishable from WT BMDM during infection with live Mtb. In contrast, our model—with type I IFN being both upstream and downstream of mitochondrial damage (Figure III.16)—predicts STING KO BMDM will have reduced mitochondrial damage during infection. Importantly, exogenous type I IFN added during infection with Mtb in STING KO BMDM should recapitulate the damage seen in WT macrophages.

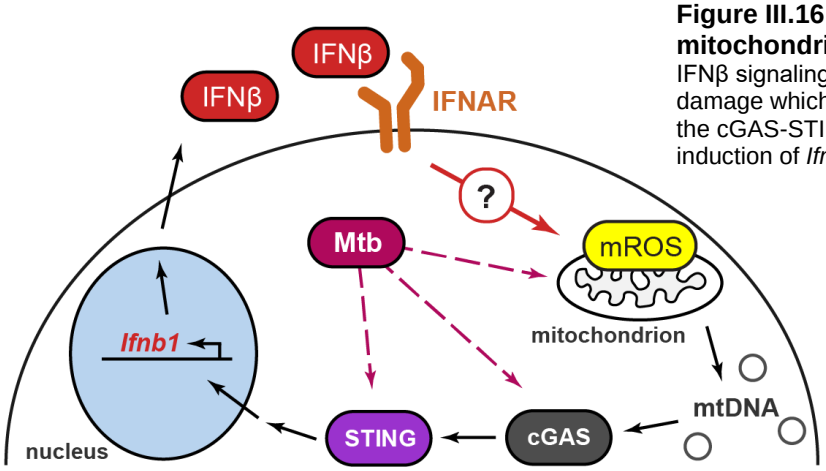


**Figure III.16 Proposed model of Mtb-IFN-mitochondrial feedback loop**
IFNβ signaling through IFNAR causes mitochondrial damage which could release mtDNA to be sensed by the cGAS-STING signaling pathway leading to induction of *Ifnb1* expression and IFNβ secretion.

Repeating the previous metabolic analyses in STING KO BMDM confirms the predictions of our model. Live H37Rv infection in STING KO BMDM does not restrain glycolysis (Figure III.17) and only slightly decreases mitochondrial respiration (Figure III.18). Furthermore, STING KO BMDM accumulate less mROS than WT BMDM after infection (Figure III.19). Consistently, the addition of exogenous IFNβ to infected STING KO BMDM restores the metabolic dysfunction seen in each assay (Figures III.17-19), further validating the causal link between type I IFN and mitochondrial damage in macrophages during Mtb infection.

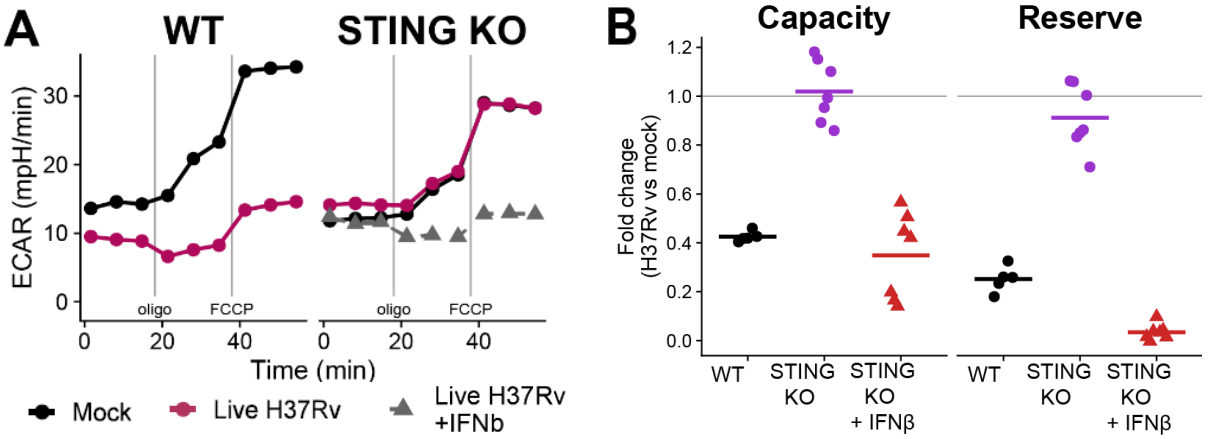


**Figure III.17 STING is required for glycolytic restraint during H37Rv infection**
(A) Extracellular acidification rate (ECAR) of WT or STING KO BMDMs either mock infected or infected with live H37v at an MOI of 10 for 24 hours. Infected STING KO BMDM were either left untreated or treated with 500 U/mL IFNβ. A single representative plate is shown. (B) Quantification of glycolytic parameters from (A). Each point represents a single well and the bars are the mean from 6 plates from two independent experiments.

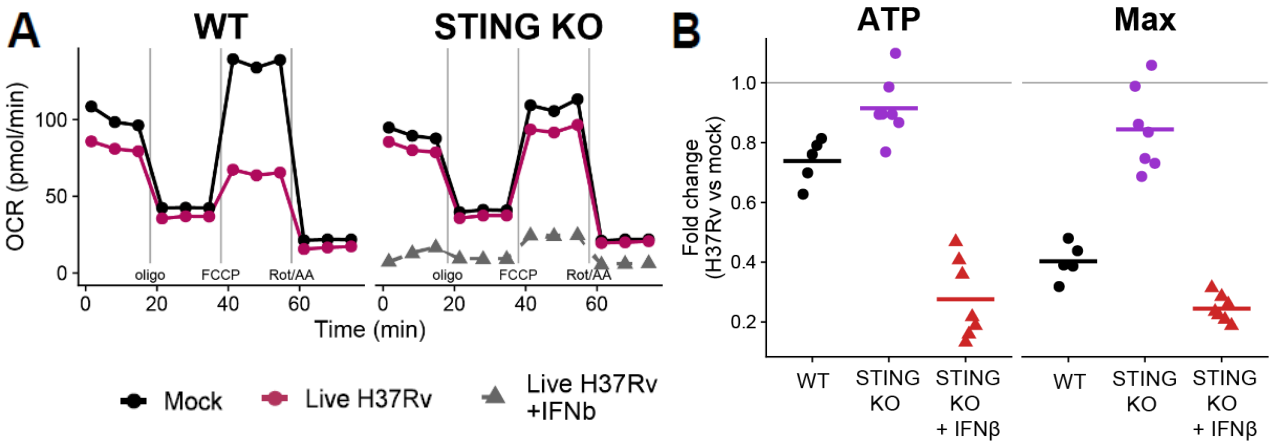


**Figure III.18 STING is required for mitochondrial dysfunction during H37Rv infection**
(A) Oxygen consumption rate (OCR) of WT or STING KO BMDMs either mock infected or infected with live H37Rv at an MOI of 10 for 24 hours. Infected STING KO BMDM were either left untreated or treated with 500 U/mL IFNβ. A single representative plate is shown.
(B) Quantification of mitochondrial parameters from (A). The OCR dedicated to ATP production (ATP) or at maximal respiration (Max) was normalized to mock infected, untreated controls. Each point represents a single well and the bars are the mean from 6 plates from two independent experiments.

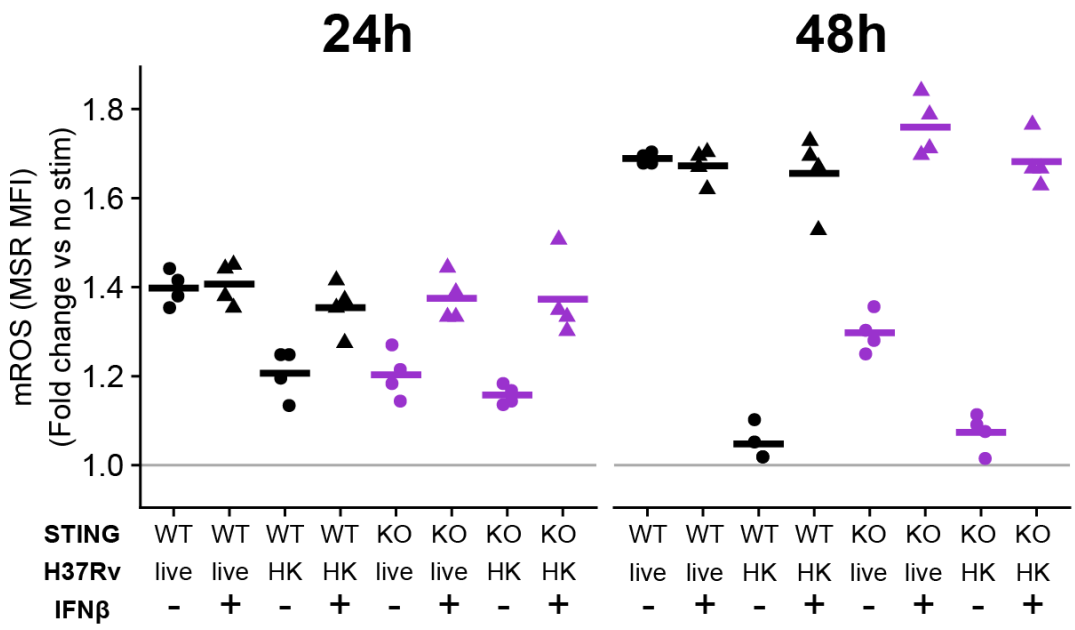


**Figure III.19 STING is required for accumulation of mROS during live H37Rv infection**
Quantification of mROS in WT or STING KO BMDM infected with MOI 10 live H37Rv or heat-killed (HK) H37Rv for indicated time. BMDM were either untreated or treated with 500 U/mL IFNβ. mROS measured with MitoSOX Red (MSR) MFI (flow cytometry) normalized to untreated, mock-infected controls at each timepoint. A representative experiment of 2 independent experiments shown.

We next performed RNA-seq on STING KO BMDM infected with live and HK H37Rv in the absence and presence of exogenous IFNβ. As predicted by our metabolic data, fewer genes are DE when directly comparing infection conditions in STING KO BMDM (Figure III.20A) and the STING KO response to live H37Rv clusters with the WT or STING KO response to HK H37Rv (Figure III.20B). In addition, STING KO BMDM maintain higher expression of genes encoded on mtDNA than WT BMDM upon infection with live H37Rv (Figure III.20C). Exogenous IFNβ added to STING KO BMDM infected with live H37Rv makes the transcriptional response much more closely resemble the WT response to live H37Rv (Figure III.20), confirming that the lack of induction of type I IFN is the main difference in the Mtb response of STING KO BMDM.

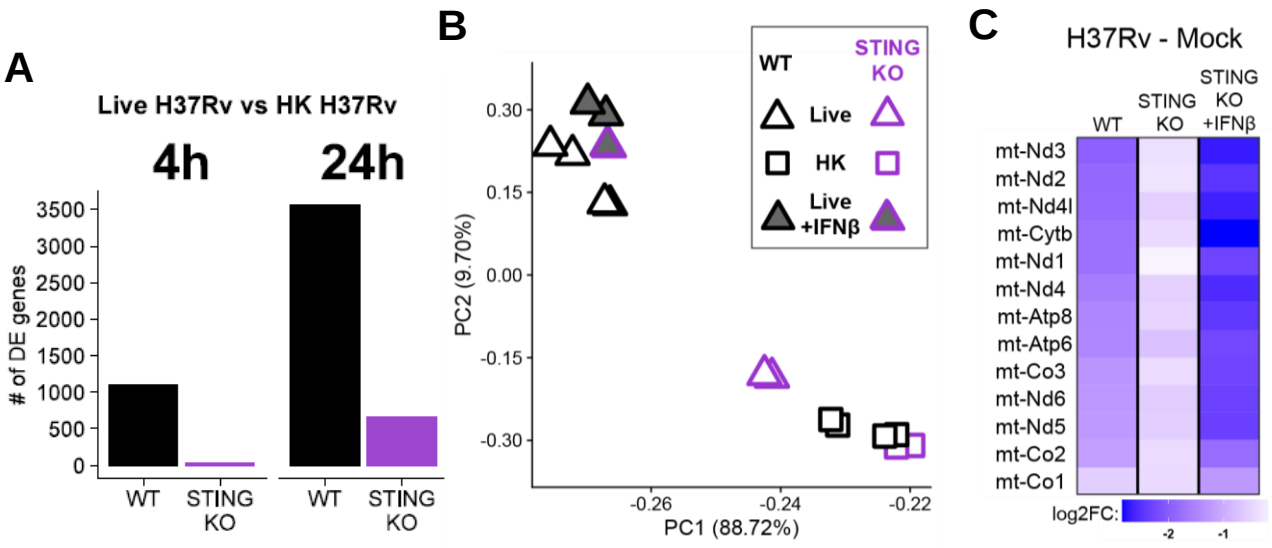


**Figure III.20 STING is required for robust transcriptional response to live H37Rv by induction of type I IFN**
(A) The number of DE genes (FDR <0.001, |log2FC| > 1) comparing infection conditions (live H37Rv vs HK H37Rv; MOI 10) at 4 or 24 hours post infection in WT or STING KO BMDM.
(B) Principal component analysis of WT or STING KO BMDM at 24 hours post infection with MOI 10 live H37Rv or HK H37Rv. BMDM infected with live H37Rv were left untreated or treated with 500 U/mL IFNβ. The percent of variance explained by the top two principal components is indicated.
(C) Log2FC in expression (RNA-seq) of the 13 protein coding genes encoded on mtDNA in BMDM (either WT or STING KO) infected with live H37Rv at an MOI 10 for 24 hours compared to mock infection. STING KO BMDM were either left untreated or treated with 500 U/mL IFNβ in addition to the infection.

An Mtb-initiated, type I IFN-mitochondrial positive feedback loop would be predicted to drive increased *Ifnb1* expression in BMDM with intact type I IFN signaling (Figure III.16). Indeed, WT BMDM expressed greater than three times more *Ifnb1* than IFNAR KO BMDM after 4 hours

of infection with live H37Rv, while expressing similar amounts of *Tnf* and *Il1b* (Figure III.21). Exogenous IFNβ further increases *Ifnb1* expression in WT BMDM. We confirmed that live H37Rv infection of STING KO BMDM does not induce *Ifnb1* expression at this timepoint (Collins et al., 2015; Wassermann et al., 2015; Watson et al., 2015; Wiens and Ernst, 2016) (Figure III.21). Consistent with the positive feedback loop operating through mitochondrial damage and STING activation, exogenous IFNβ in addition to live H37Rv does not rescue full *Ifnb1* expression in STING KO BMDM compared to infected WT BMDM (Figure III.21).

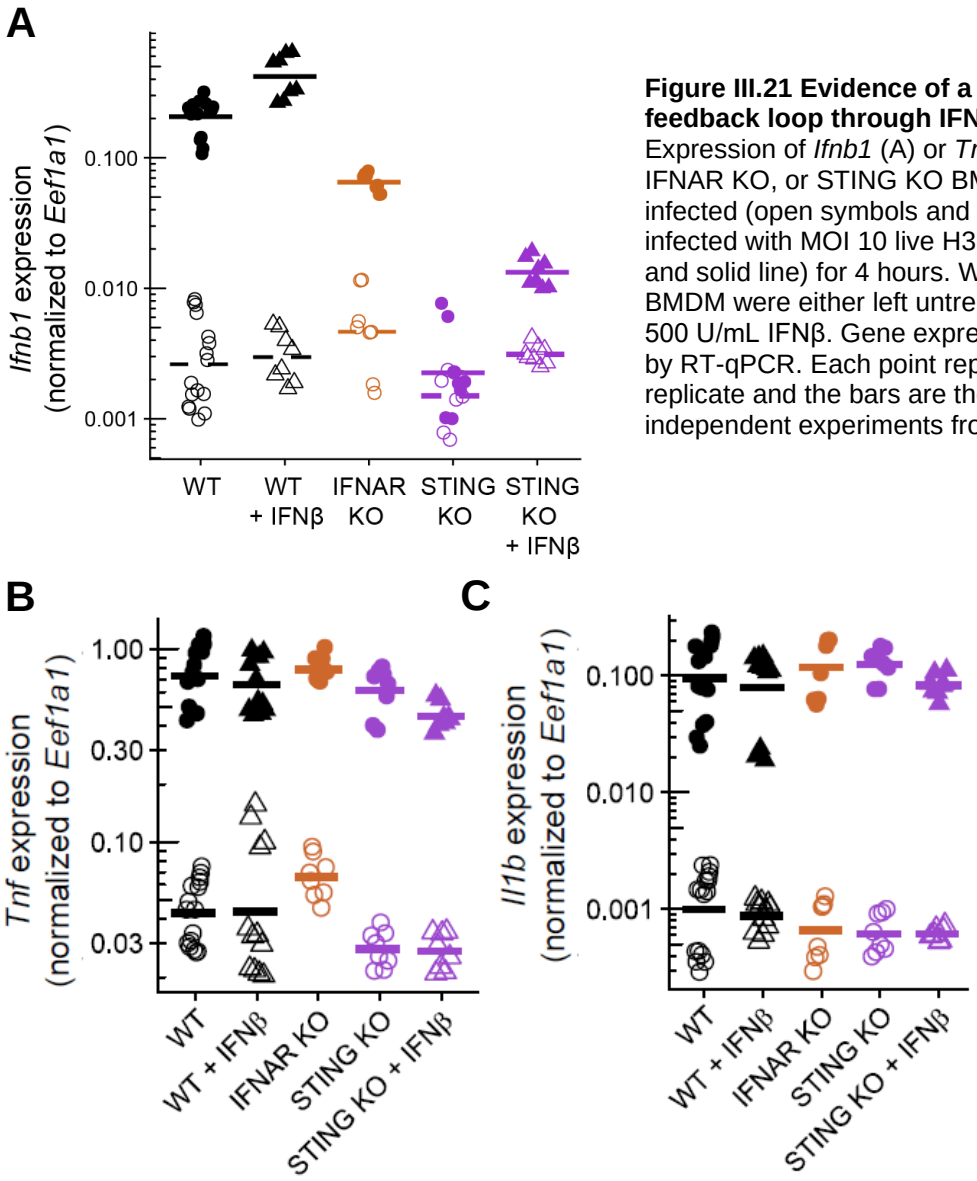


**Figure III.21 Evidence of a type I IFN positive feedback loop through IFNAR and STING**
Expression of *Ifnb1* (A) or *Tnf* and *Il1b* (B,C) in WT, IFNAR KO, or STING KO BMDM either mock infected (open symbols and dashed line) or infected with MOI 10 live H37Rv (filled symbols and solid line) for 4 hours. WT and STING KO BMDM were either left untreated or treated with 500 U/mL IFNβ. Gene expression was quantified by RT-qPCR. Each point represents a technical replicate and the bars are the mean from 2 independent experiments from each KO genotype.

## Discussion

In this Chapter, we describe a role for type I IFN as the main mechanism modulating metabolism during Mtb infection. Live, but not HK, Mtb restrains macrophage glycolysis and induces hallmarks of mitochondrial stress. We show that the differential transcriptional response of WT macrophages to live vs HK Mtb requires type I IFN signaling. We then demonstrate the causal role of type I IFN in the metabolic changes initiated by Mtb infection both *in vitro* and *in vivo*; macrophages lacking type I IFN signaling maintain mitochondrial function and glycolytic capacity after infection with live Mtb. Our conclusions are strengthened by experiments showing that exogenous type I IFN in addition to HK Mtb recapitulates the metabolic restraint observed after live Mtb infection.

The utility of type I IFN signatures for the prediction of TB progression in humans (Berry et al., 2010; Zak et al., 2016) reinvigorated interest in mechanisms linking type I IFN and Mtb pathogenesis. Although the consensus remains that type I IFN worsens disease, inconsistences in this simple interpretation abound—type I IFN treatment benefits patients with multiple drug resistant Mtb (Giosuè et al., 1998; Palmero et al., 1999), most mouse models of impaired type I IFN signaling have only minor differences in disease progression (Moreira-Teixeira et al., 2018), and type I IFN improves Mtb vaccination responses (Giacomini et al., 2009; Grode et al., 2005; Gröschel et al., 2017). The role that we report here for type I IFN in regulating the macrophage response to live Mtb might help explain how type I IFN augments vaccination strategies; type I IFN administration with an attenuated vaccine strain might improve anamnestic responses by making the transcriptional response to the vaccine more closely resemble a virulent infection. Interestingly, there is a growing appreciation that Mtb alters host cell proliferation (Cumming et al., 2017; Huang et al., 2018; Pisu et al., 2020), including modulation of bone marrow stem cell differentiation in a type I IFN-dependent manner (Kaufmann et al., 2018; Khan et al., 2020). The

connection between type I IFN, metabolic modulation, and proliferation shown in this study provides another avenue to explore the controversial role of type I IFN in Mtb pathogenesis.

We show that the metabolic restraint of macrophages during Mtb infection requires STING signaling and that treatment of Mtb infected STING KO macrophages with exogenous type I IFN recapitulates the mitochondrial damage seen in WT macrophages. Current models place type I IFN downstream of mitochondrial damage and subsequent cGAS-STING signaling (Hopfner and Hornung, 2020; Weinberg et al., 2015; West et al., 2015). We suggest that the additional placement of type I IFN *upstream* of mitochondrial dysfunction described in this study creates a positive feedback loop in macrophages. Although we show evidence that type I IFN signaling potentiates type I IFN expression in a STING-dependent manner consistent with a mitochondrial-driven loop, further study is required to rule out other established IFN feedback mechanisms.

Does mitochondrial damage or type I IFN induction initiate the loop during Mtb infection? Studies using recombinant mycobacterial proteins suggest Mtb effector molecules target the mitochondria (Cadieux et al., 2011; Shin et al., 2010; Sohn et al., 2011), but further studies are needed to characterize direct Mtb-mitochondrial interactions in more physiologic settings. It is worth noting, however, that the lack of robust mitochondrial damage in IFNAR and STING KO BMDMs argues against widely held assumptions that direct pathogen effectors are the primary explanation for metabolic changes during infections with intracellular bacteria. Although STING is required for robust type I IFN expression during Mtb infection (Collins et al., 2015; Wassermann et al., 2015; Watson et al., 2015), a recent study suggests the ligands are mitochondrial rather than mycobacterial (Wiens and Ernst, 2016). The model proposed in the current study might help resolve this perceived conflict: early minor activation by mycobacterial ligands might initiate an IFN-mitochondrial-STING loop that is required for robust induction. The minor induction of type I IFN by other recognition receptors (Cheng and Schorey, 2018; Leber et

al., 2008; Pandey et al., 2009; Troegeler et al., 2017) or mitochondrial damage by other host pathways (Weindel et al., 2020) might also contribute to initiation. Consistent with this, STING KO BMDM infected with live H37Rv and WT BMDM only treated with IFNβ had intermediate levels of mROS (i.e. higher than in mock treated cells but lower than WT BMDM infected with live H37Rv).

In summary, we believe this study provides important mechanistic insight into the metabolic response of macrophages to a clinically relevant pathogen. Furthermore, we believe investigating the metabolic effects mediated by type I IFN on macrophages offers many opportunities to disentangle the complex beneficial and detrimental roles that this fundamental cytokine family plays in immunity.

## Appendix

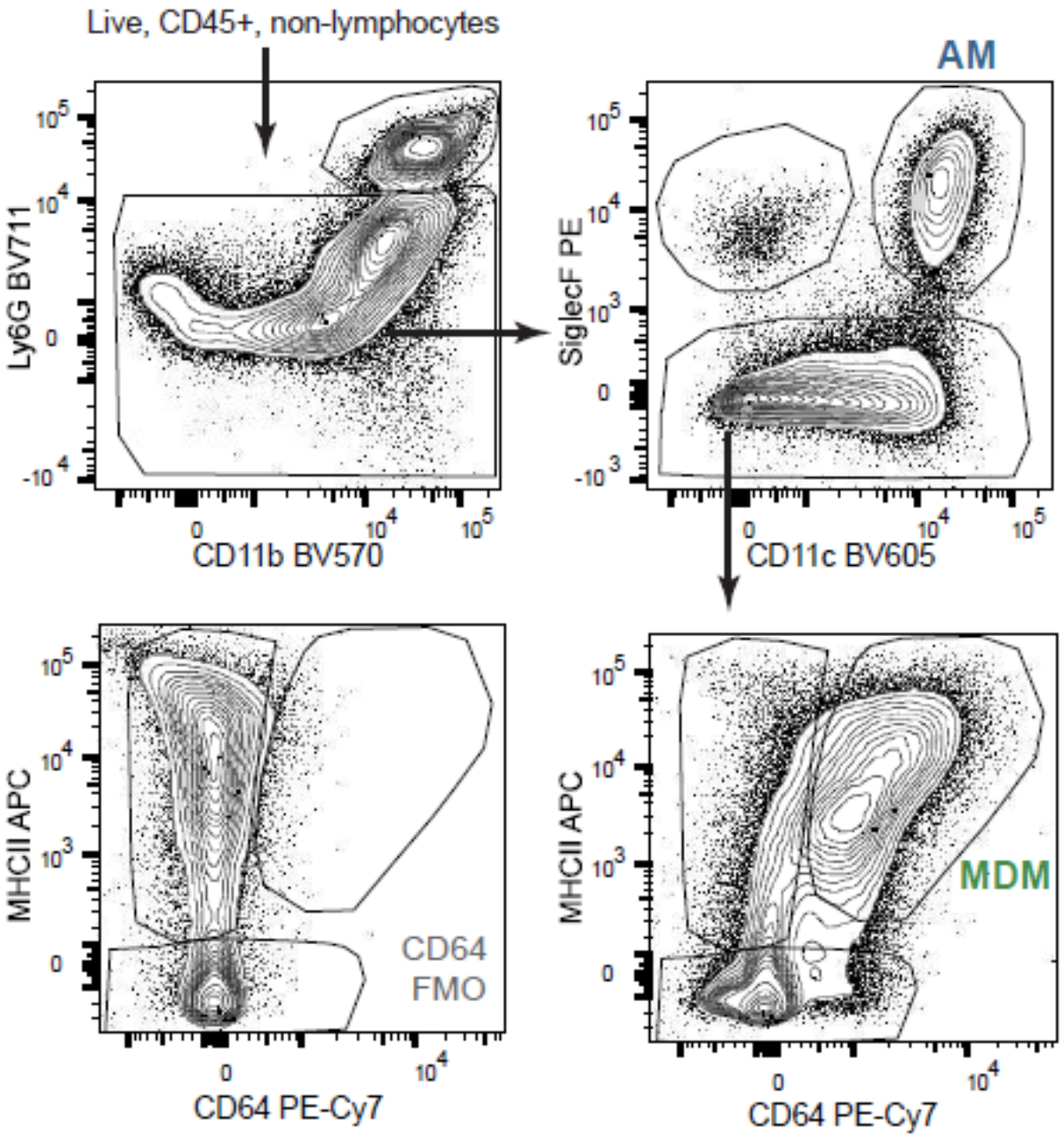


**Figure III.22 Gating strategy for *in vivo* macrophage subsets**
Gating scheme for sorting alveolar macrophages (AM) and monocyte derived macrophages (MDM) from aerosol infected mice. Total events were first gated on singlets, size (forward and side scatter), exclusion of a viability dye, and CD45 positivity before being gated as shown. Gate for MDM was based on fluorescence minus one (FMO) samples for both CD64 and MHC; CD64 FMO is shown in lower left quadrant.

| Mouse Strains | | |
|---|---|---|
| Mouse: STING KO: B6(Cg)-Sting1$^{tm1.2Camb}$/J Mus musculus | The Jackson Laboratory | Cat#025805, RRID:IMSR_JAX:025805 |
| Mouse: IFNAR KO: B6.129S2-Ifnar1$^{tm1Agt}$/Mmjax Mus musculus | The Jackson Laboratory (MMRRC) | Cat#32045-JAX, RRID:MGI:3703445 |
| Mouse: IL10 KO: B6.129P2-Il10$^{tm1Cgn}$/J Mus musculus | The Jackson Laboratory | Cat#002251, RRID:IMSR_JAX:002251 |
| Mouse: MyD88-Trif double KO: B6.129P2(SJL)-Myd88tm1.1Defr/J x C57BL/6J-Ticam1Lps2/J | Aderem lab. Parental strains: The Jackson Laboratory | Parental strains: Cat#009088 (RRID:IMSR_JAX:009088) and Cat#005037 (RRID:IMSR_JAX:005037) |
| Mouse: WT: C57BL/6J Mus musculus | The Jackson Laboratory | Cat#000664, RRID:IMSR_JAX:000664 |

**Table III.1 Mouse strains used in Chapter III**

| Oligonucleotides | | |
|---|---|---|
| *mt-Cytb* TaqMan Gene expression assay | Thermo Fisher Scientific | Cat#4331182, ID#Mm04225271_g1 |
| *mt-Co3* TaqMan Gene expression assay | Thermo Fisher Scientific | Cat#4331182, ID#Mm04225261_g1 |
| *Ifnb1* TaqMan Gene expression assay | Thermo Fisher Scientific | Cat#4331182, ID#Mm00439552_s1 |
| *Isg15* TaqMan Gene expression assay | Thermo Fisher Scientific | Cat#4331182, ID#Mm01705338_s1 |
| *Il1b* Taqman Gene expression assay | Thermo Fisher Scientific | Cat#4331182, ID#Mm01336189_m1 |
| *Tnf* TaqMan Gene expression assay | Thermo Fisher Scientific | Cat#4331182, ID#Mm00443258_m1 |
| *Eef1a1* forward primer for custom TaqMan assay: 5' GCAAAAACGACCCACCAATG 3' | Integrated DNA Technologies | N/A |
| *Eef1a1* reverse primer for custom TaqMan assay: 5' GGCCTGGATGGTTCAGGATA 3' | Integrated DNA Technologies | N/A |
| *Eef1a1* probe for custom TaqMan assay: 5' /56-FAM/CACCTGAGCAGTGAAGCCAG/36-TAMSp/3' | Integrated DNA Technologies | N/A |

**Table III.2 Oligonucleotides used in Chapter III**

| Antibodies | | |
|---|---|---|
| Brilliant Violet 570 Rat monoclonal anti-mouse CD11b (clone M1/70) | Biolegend | Cat# 101233, RRID:AB_10896949 |
| Brilliant Violet 605 Armenian hamster monoclonal anti-mouse CD11c (clone N418) | Biolegend | Cat# 117333, RRID:AB_11204262 |
| Brilliant Violet 711 Rat monoclonal anti-mouse Ly-6G (clone 1A8) | Biolegend | Cat# 127643, RRID:AB_2565971 |
| Briliant Violet 785 Rat monoclonal anti-mouse Ly-6C (clone HK1.4) | Biolegend | Cat# 128041, RRID:AB_2565852 |
| Alexa Fluor 488 Rat monoclonal anti-mouse MERTK (clone DS5MMER) | Thermo Fisher Scientific | Cat# 53-5751-82, RRID:AB_2784751 |
| PerCP Cyanine5.5 Mouse monoclonal anti-mouse CD45.2 (clone 104) | Biolegend | Cat# 109828, RRID:AB_893350 |
| Phycoerythrin Rat monoclonal anti-mouse Siglec-F (clone E50-2440) | BD Biosciences | Cat# 552126, RRID:AB_394341 |
| PE Cyanine7 Mouse monoclonal anti-mouse CD64 (clone X54-5/7.1) | Biolegend | Cat# 139313, RRID:AB_2563903 |
| APC Rat monoclonal anti-mouse I-A/I-E (MHC class II) clone M5/114.15.2) | Biolegend | Cat# 107614, RRID:AB_313329 |
| APC-eFluor 780 Rat monoclonal anti-mouse CD19 (clone eBio1D3(1D3)) | Thermo Fisher Scientific | Cat# 47-0193-82, RRID:AB_10853189 |
| APC-eFluor 780 Rat monoclonal anti-mouse CD3 (clone 17A2) | Thermo Fisher Scientific | Cat# 47-0032-82, RRID:AB_1272181 |
| Unconjugated Rat monoclonal anti-mouse CD16/CD32 (clone 2.4G2) | BD Biosciences | Cat# 553141, RRID:AB_394656 |

**Table III.3 Antibodies used in Chapter III**

| Additional Reagents | | |
|---|---|---|
| **Bacterial Strains** | | |
| Mycobacterium tuberculosis, H37Rv | BEI Resources | Cat#NR-123 |
| Biological Samples | | |
| **Chemicals, Peptides, and Recombinant Proteins** | | |
| Lipopolysaccharide from Salmonella Minnesota | List Labs | Cat#R595 |
| Synthetic triacylated lipopeptide (Pam3CSK4) | Invivogen | Cat#vac-pms |
| Interferon-β Protein, Recombinant mouse | Millipore Sigma | Cat#IF011 |
| Recombinant Human M-CSF | PeproTech | Cat#300-25 |
| Liberase TM Research Grade | Millipore Sigma | Cat#5401127001 |
| DNase I grade II | Millipore Sigma | Cat#10104159001 |
| ACK Lysing Buffer | Thermo Fisher Scientific | Cat#A1049201 |
| 20% Paraformaldehyde aqueous solution | Electron Microscopy Sciences | Cat#15713-S, CAS#50-00-0 |
| TRIzol Reagent | Thermo Fisher Scientific | Cat#15596026 |
| RIPA buffer (10X) | Cell Signaling Technology | Cat#9806 |
| Halt™ Protease Inhibitor Cocktail (100X) | Thermo Fisher Scientific | Cat#78430 |
| Carbonyl cyanide 4-(trifluoromethoxy)phenylhydrazone (FCCP) | Millipore Sigma | Cat#C2920, CAS#370-86-5 |
| Oligomycin A | Millipore Sigma | Cat#75351, CAS#579-13-5 |
| Antimycin A from Streptomyces sp. | Millipore Sigma | Cat#A8674, CAS#1397-94-0 |
| Rotenone | Millipore Sigma | Cat#R8875, CAS#83-79-4 |
| 2-Deoxy-D-glucose | Millipore Sigma | Cat#D8375, CAS#154-17-6 |
| D-(+)-Glucose | Millipore Sigma | Cat#G7528, CAS#50-99-7 |
| Tetramethylrhodamine, Methyl Ester, Perchlorate (TMRM) | Thermo Fisher Scientific | Cat#T668, CAS#115532-50-8 |

**Table III.4 Bacterial strains and chemicals used in Chapter III**

| Critical Commercial Assays | | |
|---|---|---|
| CyQUANT LDH Cytotoxicity Assay | Thermo Fisher Scientific | Cat#C20301 |
| Pierce BCA Protein Assay Kit | Thermo Fisher Scientific | Cat#23225 |
| Direct-zol-96 RNA kits | Zymo Research | Cat#R2056 |
| RNA to cDNA EcoDry™ Premix (Oligo dT) | Takara Bio | Cat#639542 |
| Taqman Fast Universal PCR Master Mix (2x), No AmpErase UNG | Thermo Fisher Scientific | Cat#4364103 |
| LIVE/DEAD Fixable Violet Dead Cell Stain Kit | Thermo Fisher Scientific | Cat#L34964 |
| MitoSOX Red Mitochondrial Superoxide Indicator | Thermo Fisher Scientific | Cat#M36008 |
| MitoTracker Green FM | Thermo Fisher Scientific | Cat#M7514 |
| Seahorse XFp Cell Glycolysis Stress Test Kit | Agilent | Cat#103017-100 |
| Seahorse XFp Cell Mito Stress Test Kit | Agilent | Cat#103010-100 |

**Table III.5 Critical commercial assays used in Chapter III**

| Software and Algorithms | | |
|---|---|---|
| RStudio 1.1.463 | RStudio | http://www.rstudio.com, RRID:SCR_000432 |
| edgeR 3.26.8 | Robinson et al., 2009 | http://bioconductor.org/packages/edgeR/, RRID:SCR_012802 |
| R 3.6.1 | Cran | https://www.r-project.org/, RRID:SCR_001905 |
| FastQC | Babraham Institute | http://www.bioinformatics.babraham.ac.uk/projects/fastqc/, RRID:SCR_014583 |
| GSNAP 2018-07-04 | Wu and Nacu, 2010 | http://research-pub.gene.com/gmap/, RRID:SCR_005483 |
| featureCounts v1.5.2 | Liao et al., 2014 | http://bioinf.wehi.edu.au/featureCounts/, RRID:SCR_012919 |
| CellProfiler Image Analysis Software 3.1.9 | McQuin et al., 2018 | http://cellprofiler.org, RRID:SCR_007358 |
| (Fiji is just) ImageJ 1.53c | Schindelin et al., 2012 | http://fiji.sc, RRID:SCR_002285 |
| Molecular Signatures Database (MSigDB) v7.2 | Subramanian et al, 2005 | http://software.broadinstitute.org/gsea/msigdb/index.jsp, RRID:SCR_016863 |
| Seahorse Wave 2.6.1.53 | Agilent | http://www.agilent.com/en-us/products/cell-analysis-(seahorse)/software-download-for-wave-desktop, RRID:SCR_014526 |
| FlowJo 10.5.3 | Becton, Dickinson and Company | https://www.flowjo.com/solutions/flowjo, RRID:SCR_008520 |
| Pathview 1.24.0 | Luo and Brouwer, 2013 | http://bioconductor.org/packages/release/bioc/html/pathview.html, RRID:SCR_002732 |
| HypeR 1.3.1 | Federico and Monti, 2020 | https://www.bioconductor.org/packages/release/bioc/html/hypeR.html |

**Table III.6 Software used in Chapter III**

# Chapter IV: Type I interferon restrains macrophage metabolism by itself and during Toll-like receptor stimulation

Sections of text in this chapter have been modified slightly from the following manuscript: **Olson, G.S.,** Murray, A.M., Jahn, A.N., Mai, D., Diercks, A.H., Gold, E.S., Aderem, A. (2021). Type I interferon controls macrophage metabolism during mycobacterial infection. *In preparation*.

## Introduction

Chapter III proposes that induction of type I IFN fully explains the metabolic response of BMDMs to live Mtb but did not formally show that type I IFN by itself modulates macrophage metabolism. Although earlier transcriptional analyses suggest metabolic rewiring by type I IFN (Ahmed et al., 2018), functional changes to energy metabolism downstream of this cytokine family have not been thoroughly investigated in macrophages. Moreover, the metabolic pattern observed in BMDM infected with live H37Rv (i.e. mitochondrial dysfunction and decreased glycolytic capacity (Figure III.4)) does not agree with published reports of the metabolic impact of type I IFN in other innate immune cells (Everts et al., 2014; Pantel et al., 2014; Wu et al., 2016). For instance, recent reports suggest that type I IFN modulates dendritic cell (DC) metabolism in a subset-dependent manner (increasing glycolysis in conventional DC (Everts et al., 2014) or increasing oxidative phosphorylation (OXPHOS) in plasmacytoid DC (Wu et al., 2016)).

In this Chapter, we explore whether IFNβ alone induces metabolic changes in BMDM that could explain those seen upon live H37Rv infection. In doing so, we hope to solidify the causal relationship between type I IFN and macrophage metabolism in the context of Mtb infection. To contextualize our findings in the broader field of TLR-induced metabolic changes,

we compare the metabolic response following IFNβ treatment to the well characterized shift to aerobic glycolysis described for stimulation with TLR ligands.

## Methods

Most methods used in this Chapter are shared with those described in detail in Chapter III. Modifications or additions are noted below:

### Metabolic flux analysis: XFe24

An Agilent XFe24 analyzer was used to compare the effects of IFNβ and/or LPS treatment on BMDM. BMDM were plated at 100,000 cells/well of an XFe24 miniplate (Agilent) on day 6 of differentiation and rested overnight. The XFe24 cartridge was hydrated in Agilent XF Calibrant overnight. BMDM culture media was removed and the cells were washed twice with appropriately supplemented XF RPMI pH 7.4 (Agilent) media 1 hour before loading in the analyzer. The same final concentrations of compounds as for the XFp analyzer were used (see Chapter III), although the compounds were obtained independently rather than from the pre-formulated Agilent kits.

### TLR ligand stimulation

Frozen stocks of LPS or PAM3Csk4 were thawed and sonicated for 5 minutes before dilution in BMDM media. The diluted stimuli were again sonicated for 5 minutes before addition to BMDM cultures for a final concentration of 10 ng/mL for LPS and 300 ng/mL for PAM3Csk4. In some experiments, 500 U/mL IFNβ was added at the same time as LPS stimulation.

### Bicinchoninic acid assays

The total protein present in adherent cultures was measured using bicinchoninic acid assays for Seahorse experiments to control for changes in cell number. After the Seahorse analyzer experiment finished, the plate was immediately removed from the machine, the media was removed from the cells, and ice-cold 1X RIPA buffer (10X buffer diluted in $H_2O$) + 1X Halt™

protease inhibitor cocktail was added to the cells. Cells were kept on ice for at least 5 minutes and then the lysate was homogenized by pipetting and diluted 1:4 with PBS before quantifying total protein with the Pierce™ BCA Protein Assay Kit according to manufacturer's instructions. Briefly, the working reagent was added to diluted samples in duplicate and albumin standard curves in triplicate for 30 minutes at 37 ºC and the protein concentration was calculated according to a 4-parameter logistic regression based on absorbance at 540 nm.

**RNA-seq gene set enrichment analysis and pathway visualization**

A self-contained rotational gene set tests (Wu et al., 2010), implemented in the edgeR package in R (McCarthy et al., 2012; Robinson et al., 2009), was used to directly test the directional regulation of the Hallmark Glycolysis pathway. The visualization of the $\log_2$FC (IFNβ treated vs untreated at 28 hours after treatment) of enzymes in the KEGG Glycolysis/Gluconeogenesis pathway (mmu00010) was adapted from the pathview R package (Luo and Brouwer, 2013). Because multiple genes can catalyze each enzymatic step, the labels on each set were generalized to represent the gene family. The method for summarizing expression changes across multiple genes was set to sum (node.sum = "sum").

**Statistical information**

Data were analyzed using R. Data are either presented as individual technical replicates with a horizonal bar representing the mean, or as a point representing the mean with SEM error bars. Statistical significance for more than two groups was calculated with a one-way ANOVA followed by Tukey's honestly significant difference (HSD) tests on pairwise comparisons. Precise values of n and numbers of independent experiments are indicated in figure legends.

## Results

### Interferon β restrains bone marrow derived macrophage glycolytic machinery

As expected, LPS stimulation for 24 hours shifts BMDM towards aerobic glycolysis which increases the extracellular acidification rate in the presence of glucose (Figure IV.1). In contrast, IFNβ treatment decreases basal glycolysis and dramatically reduces the capacity to increase glycolysis upon mitochondrial inhibition (Figure IV.1). The reduction in glycolytic capacity occurs at two different doses and begins as early as four hours after treatment (Figure IV.2). Although the glycolytic capacity is decreased early, acute treatment of BMDM with IFNβ does not change the basal ECAR in the presence of glucose for the first 12 hours of observation (Figure IV.3). This agrees with the preserved basal glycolysis observed in the glycolytic stress test after only 4 hours of treatment (Figure IV.2).

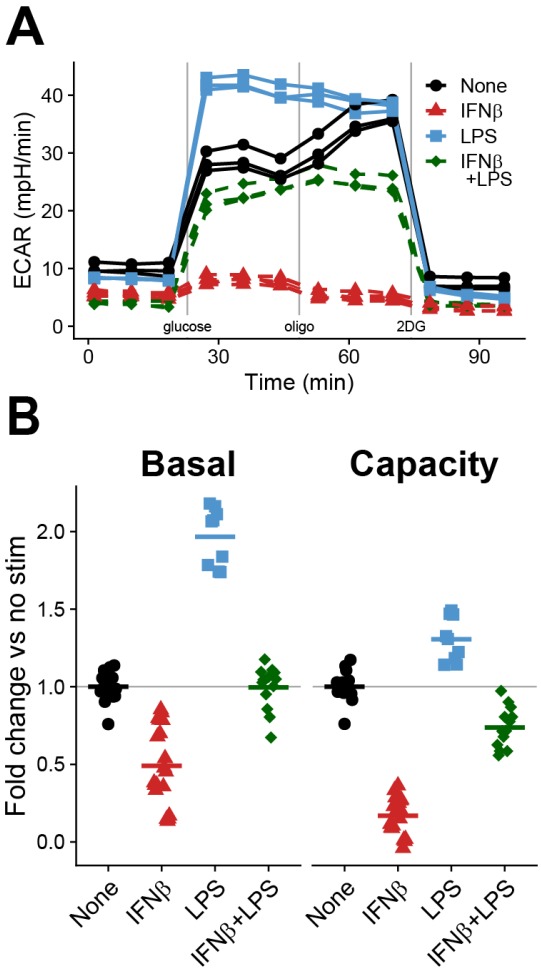


**Figure IV.1 IFNβ restrains macrophage glycolysis**
(A) Extracellular acidification rate (ECAR) of WT BMDMs either untreated or treated with 500 U/mL IFNβ, 10 ng/mL LPS, or both for 24 hours. A single representative plate is shown.
(B) Quantification of glycolytic parameters derived from (A). Each dot represents a single well and the bar is the mean from 3 (LPS alone), 5 (IFNβ), or 4 (both) independent experiments.

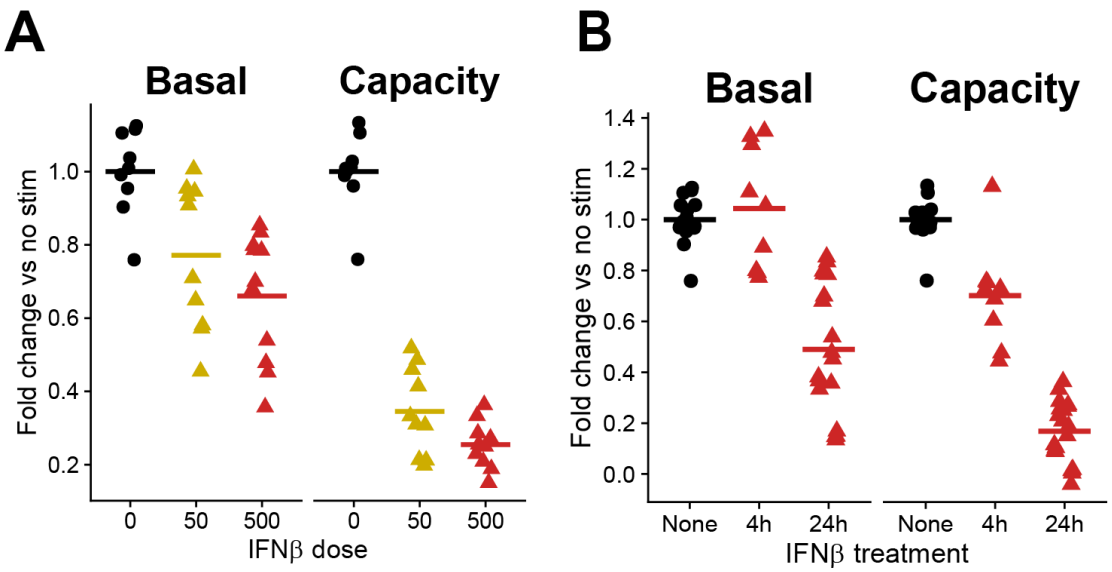


**Figure IV.2 IFNβ decreases macrophage glycolysis at two doses and as early as 4 hours**
A) The extracellular acidification rate (ECAR) after addition of glucose (Basal glycolysis) or at maximum glycolysis (Capacity) in WT BMDM treated with either 50 or 500 U/mL IFNβ for 24 hours. 500 U/mL IFN treated data shown for comparison (appears in Figure IV.1). Data for 50 U/mL shown for three independent experiments.
(B) Basal glycolysis and glycolytic capacity in WT BMDM treated with 500 U/mL IFNβ for either 4 or 24 hours. 24h IFN treated data shown for comparison (appears in Figure IV.1). Data shown for 4h treatment from 3 independent experiments.

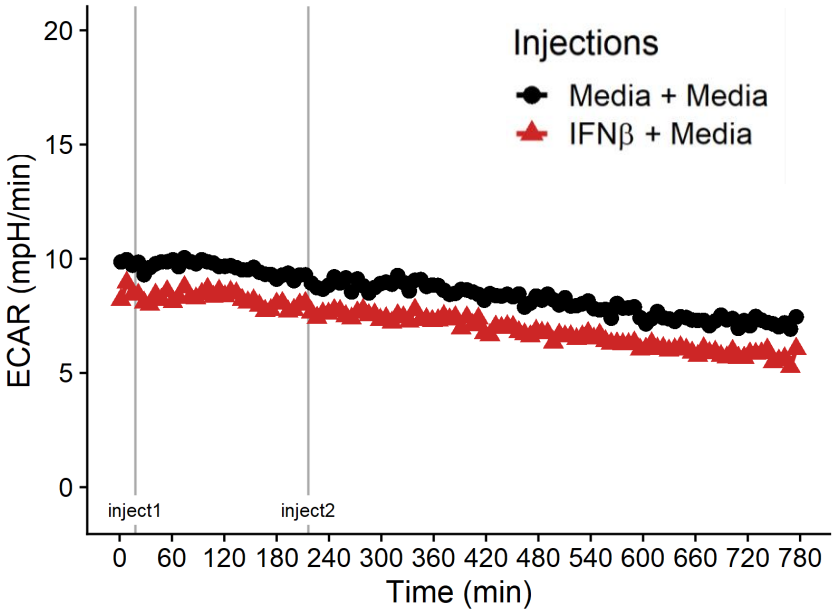


**Figure IV.3 IFNβ does not change ECAR acutely**
The extracellular acidification rate (ECAR) in WT BMDM was measured continually for ~13 hours. After three measurements (~15 minutes) of baseline monitoring, either media or IFNβ (for a final concentration of 500 U/mL) was added and ECAR measured for another ~3 hours before another injection (in this figure, media was added to both conditions). The ECAR was then measured for an additional ~10 hours. A single plate from a single experiment is shown.

We observed that IFNβ treatment decreases BMDM proliferation, evidenced by less total protein and fewer cells without an increase in cell death (Figure IV.4). However, the changes in glycolytic parameters remained statistically significant after we normalized bulk measurements of ECAR to total protein in each well (Figure IV.5), supporting a cell-intrinsic effect on glycolysis.

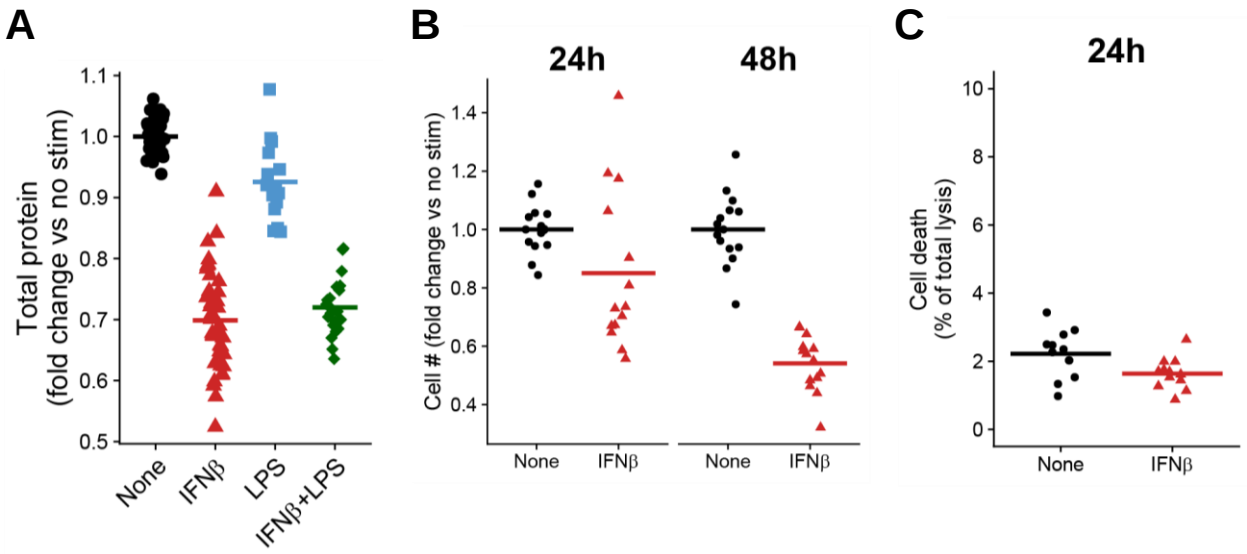


**Figure IV.4 IFNβ treatment reduces BMDM proliferation**
(A) WT BMDMs either untreated or treated with 500 U/mL IFNβ, 10 ng/mL LPS, or both for 24 hours were lysed, and total protein was measured by a BCA assay. Fold change was calculated compared to untreated controls.
(B) Flow cytometric counts (# live cells counted in 10 seconds during constant flow rate) for WT BMDM with no treatment or treatment with 500 U/mL IFNβ for the indicated time.
(C) Cell death in WT BMDM either untreated or treated with 500 U/mL IFNβ for 24 hours. Percent death was calculated by normalizing LDH content in supernatants to LDH content after total lysis.

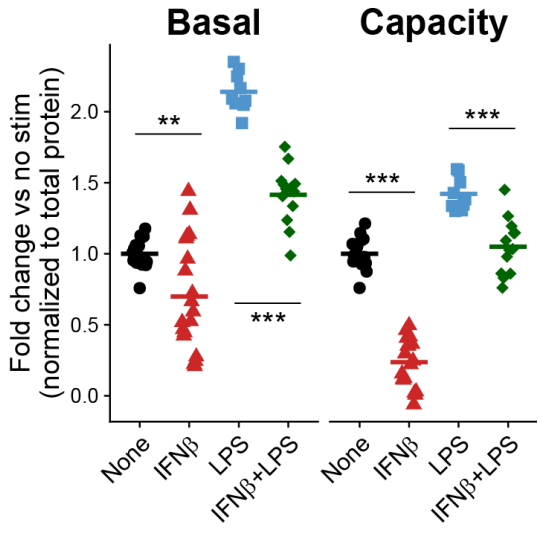


**Figure IV.5 Changes in cell number do not fully explain glycolytic changes**
Glycolytic parameters normalized to total protein in WT BMDM treated as in Figure IV.1. Basal glycolysis and glycolytic capacity were normalized per well to total protein shown in Figure IV.4. Each dot represents a single well and the bar is the mean from 3 (LPS alone), 5 (IFNβ), or 4 (both) independent experiments. Tukey Honest Significant Difference test for multiple comparisons used to test IFNβ vs no stim and IFNβ + LPS vs LPS. Adjusted p values: * (< 0.01), ** (<0.001), *** (<0.0001).

Transcriptional upregulation of glycolytic machinery contributes to the shift towards aerobic glycolysis in LPS-stimulated BMDM (Cheng et al., 2014; O'Neill et al., 2016). Although the Hallmark Glycolysis gene set is enriched in a cluster of genes downregulated by IFNβ (Figure III.11), the hypergeometric test used is agnostic to the direction of gene regulation. We therefore performed a self-contained rotational gene set test (Wu et al., 2010) which confirmed IFNβ leads to a significant transcriptional downregulation of the Hallmark Glycolysis pathway after 28 hours (FDR 4.94E-4). Mapping these transcriptional changes onto the KEGG Glycolysis pathway shows downregulation of genes at multiple steps (Figure IV.6). Interestingly, the first step of the pathway (phosphorylation of glucose) is upregulated, suggesting that glucose-6-phosphate might be shunted to non-glycolytic uses through the pentose phosphate pathway in IFNβ treated BMDM (Figure IV.6). We reasoned that the transcriptional downregulation of glycolytic enzymes by IFNβ might restrain the LPS-driven glycolytic shift. Indeed, IFNβ-treatment prevents BMDM from increasing glycolysis after 24 hours of LPS stimulation (Figure IV.1). We confirmed that IFNβ restrains other TLRs by using Pam3CSK4, a ligand for TLR2/TLR1 heterodimers (Figure IV.7).

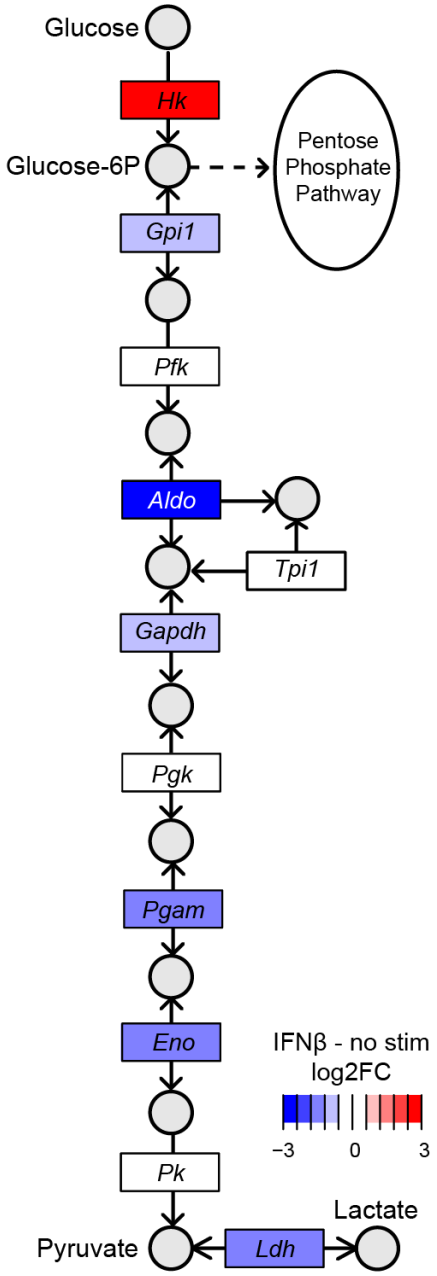


**Figure IV.6 IFNβ decreases transcription of many downstream glycolytic enzymes**
Log2FC (RNA-seq) in expression of gene families (rectangles) involved in the KEGG Glycolysis pathway comparing WT BMDM treated with 500 U/mL IFNβ for 28 hours to untreated BMDM. Key metabolites (circles) are labeled.

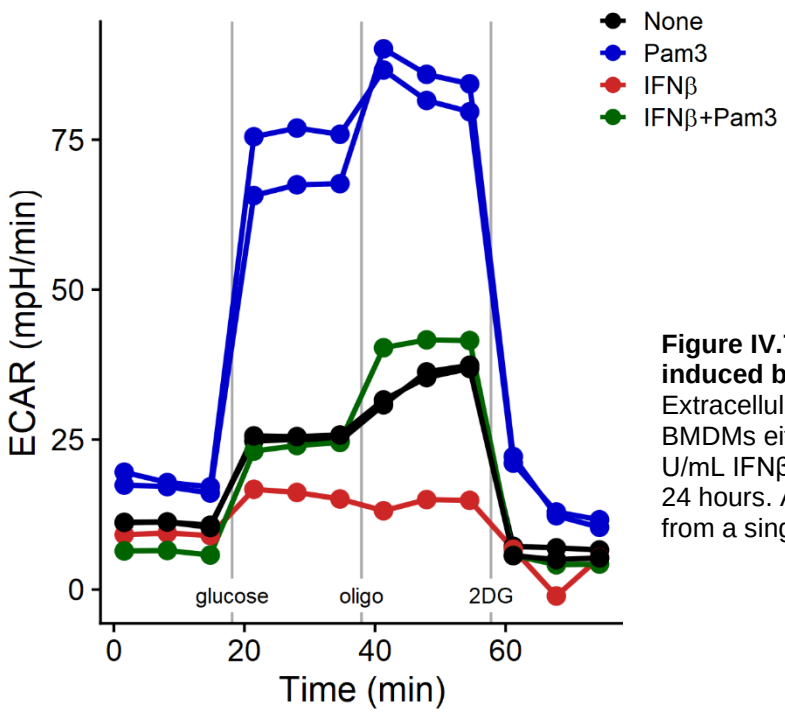


**Figure IV.7 IFNβ restrains the glycolytic shift induced by Pam3CSK4**
Extracellular acidification rate (ECAR) of WT BMDMs either untreated or treated with 500 U/mL IFNβ, 300 ng/mL Pam3CSK4, or both for 24 hours. A single representative plate of two from a single experiment is shown.

We next interrogated the ability of IFNβ to restrain the glycolytic shift of inflammatory macrophages at timepoints earlier than 24 hours. IFNβ treatment also restrains the early shift towards glycolysis, as evidenced by decreased basal glycolysis and glycolytic capacity at only 4 and 7 hours after stimulation (Figure IV.8). Furthermore, acute treatment of BMDM with IFNβ for only 3 hours prior to addition to LPS restrains the immediate glycolytic shift induced by TLR ligation (Figure IV.9). We therefore conclude that treatment of BMDM with IFNβ not only reduces glycolysis itself but also restrains the metabolic reprogramming that powers inflammatory macrophages.

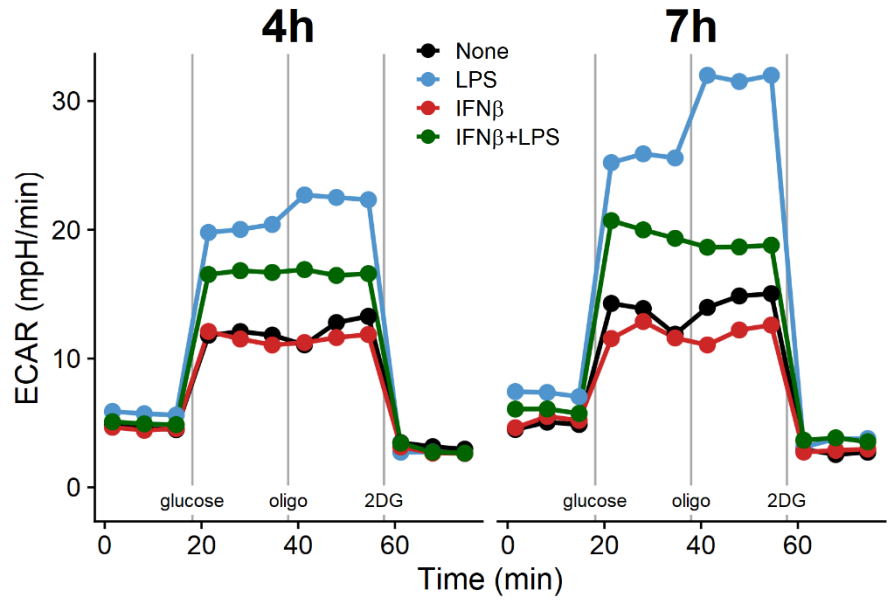


**Figure IV.8 IFNβ restrains the glycolytic shift at early timepoints**
Extracellular acidification rate (ECAR) of WT BMDMs either untreated or treated with 500 U/mL IFNβ, 10 ng/mL LPS, or both for 4 (left) or 7 (right) hours. A single representative plate of two from a single experiment is shown.

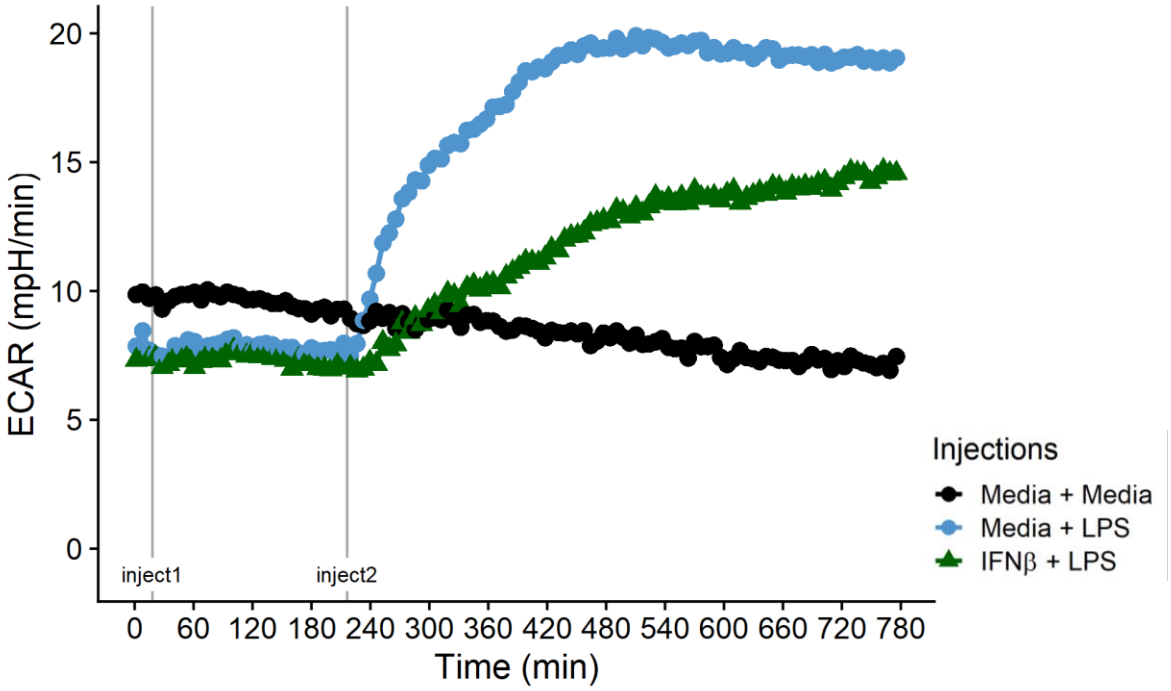


**Figure IV.9 IFNβ treatment restrains the immediate glycolytic shift upon LPS stimulation**
The extracellular acidification rate (ECAR) in WT BMDM was measured continually for ~13 hours. After three measurements (~15 minutes) of baseline monitoring, either media or IFNβ (for a final concentration of 500 U/mL) was added and ECAR measured for another ~3 hours before another injection (either media or LPS for a final concentration of 10 ng/mL). ECAR was then measured for an additional ~10 hours. A single plate from a single experiment is shown, and the control is shared with Figure IV.3.

**Interferon β impairs bone marrow derived macrophage mitochondrial metabolism**

We next investigated the effects of IFNβ treatment on mitochondria. BMDMs treated with IFNβ dramatically decrease their OCR, indicative of decreased mitochondrial respiration (Figure IV.10). In fact, IFNβ decreases the basal respiratory rate, the rate of ATP generation, and the maximum capacity for electron flux through the mitochondrial ETC (Figure IV.10). As expected, BMDMs stimulated with LPS for 24 hours shift away from mitochondrial metabolism and display a similar reduction in many aspects of mitochondrial function (Figure IV.10). Although the changes in OCR measurements decrease in magnitude after normalizing for total protein, they remain statistically significant (Figure IV.10C).

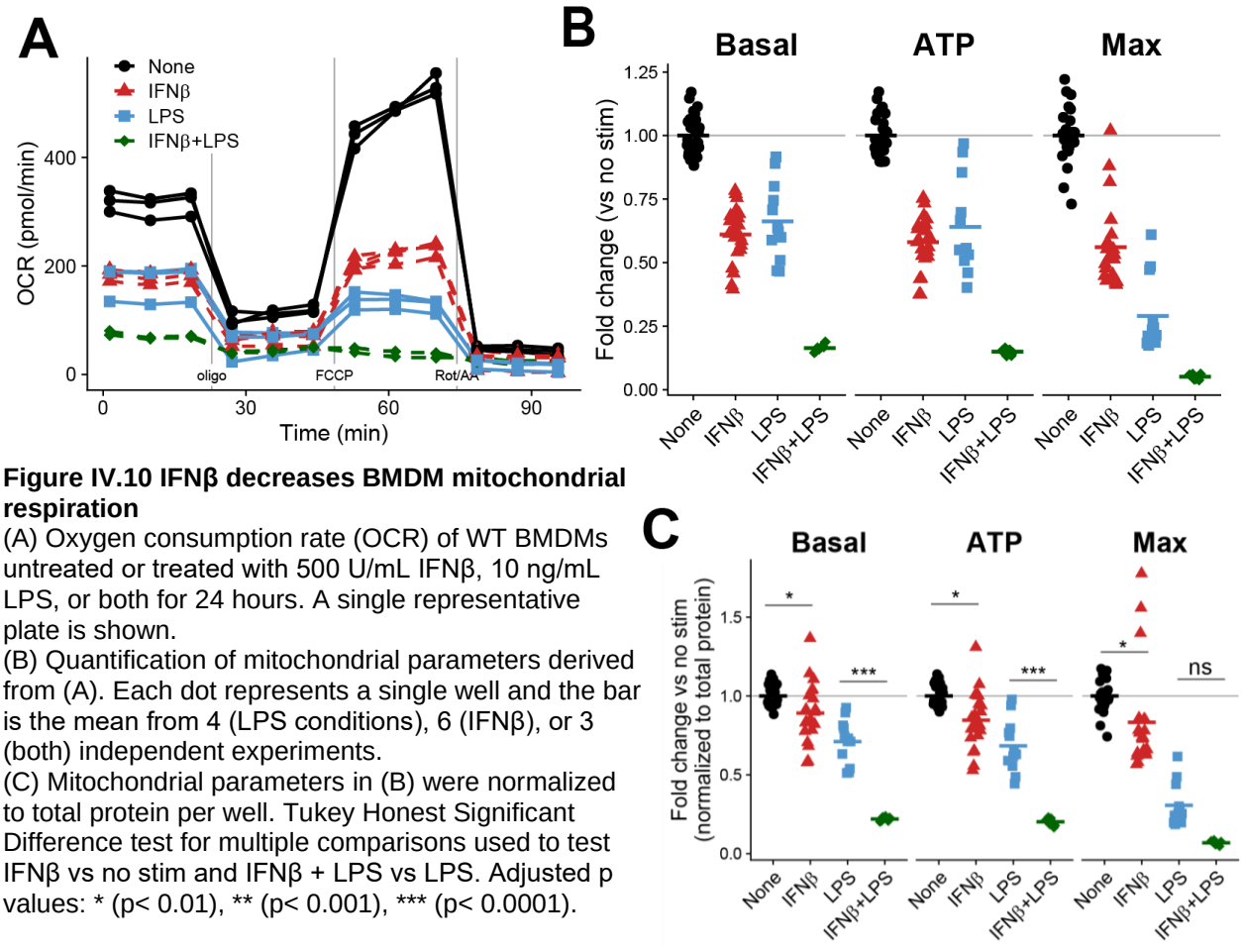


**Figure IV.10 IFNβ decreases BMDM mitochondrial respiration**
(A) Oxygen consumption rate (OCR) of WT BMDMs untreated or treated with 500 U/mL IFNβ, 10 ng/mL LPS, or both for 24 hours. A single representative plate is shown.
(B) Quantification of mitochondrial parameters derived from (A). Each dot represents a single well and the bar is the mean from 4 (LPS conditions), 6 (IFNβ), or 3 (both) independent experiments.
(C) Mitochondrial parameters in (B) were normalized to total protein per well. Tukey Honest Significant Difference test for multiple comparisons used to test IFNβ vs no stim and IFNβ + LPS vs LPS. Adjusted p values: * (p< 0.01), ** (p< 0.001), *** (p< 0.0001).

Since both LPS and type I IFN induce the cytokine IL-10, which plays a critical role in mitochondrial homeostasis (Ip et al., 2017), we investigated whether IL-10 mediates the IFNβ driven mitochondrial changes by repeating the OCR measurements in IL-10 KO BMDM; IFNβ decreases mitochondrial respiration in IL-10 KO cells to the same extent as in WT, suggesting the observed changes are IL-10 independent (Figure IV.11).

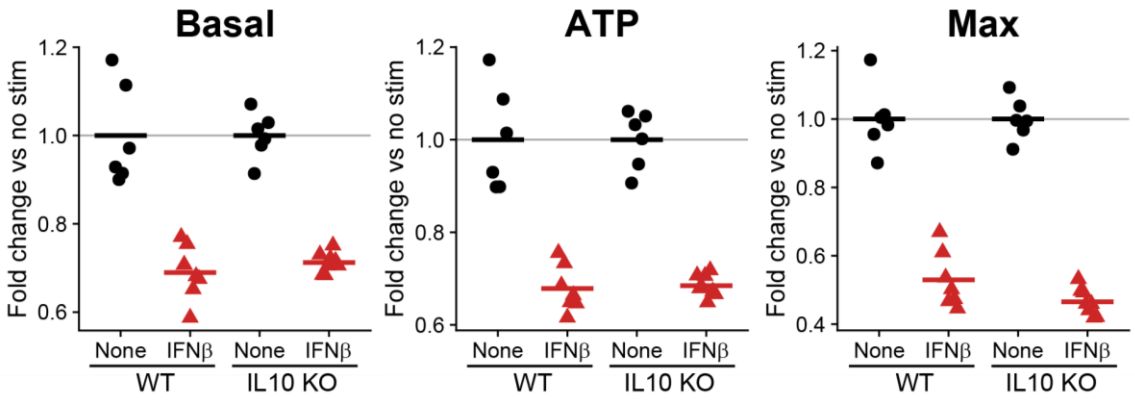


**Figure IV.11 Mitochondrial dysfunction downstream of IFNβ is independent of IL10**
Mitochondrial parameters in WT or IL10 KO BMDM either untreated or treated with 500 U/mL IFNβ for 24 hours. Each point is a single well and the bar is the mean from 6 wells across two independent experiments.

Interestingly, treatment of WT BMDM with both IFNβ and LPS together further suppresses mitochondrial respiration (Figure IV.10), suggesting that they might be impairing mitochondrial function through distinct mechanisms. Indeed, IFNβ and LPS change $\Delta\psi_m$ in opposite directions: LPS stimulation causes mitochondrial hyperpolarization (Mills et al., 2016), while IFNβ dissipates $\Delta\psi_m$ after 24 and 48 hours (Figure IV.12). Furthermore, IFNβ treatment at the same time as LPS stimulation restrains (in a dose-dependent manner) the mitochondrial membrane hyperpolarization induced by LPS alone (Figure IV.13).

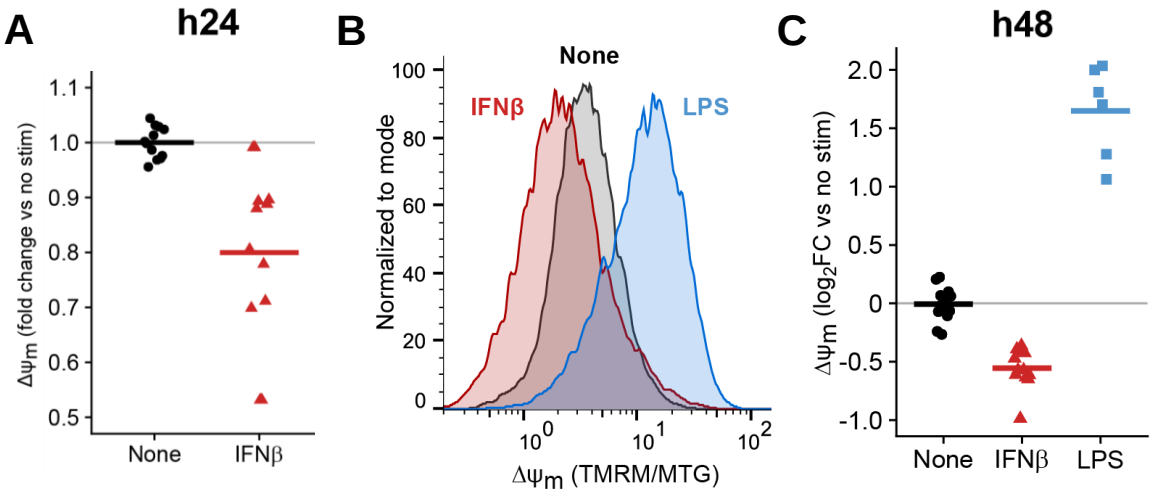


**Figure IV.12 IFNβ depolarizes the mitochondrial membrane potential of BMDM**
(A) Mitochondrial membrane potential ($\Delta\psi_m$) was calculated by normalizing TMRM to MitoTracker Green (MTG) fluorescence measured by flow cytometry at 24 hours of treatment with IFNβ. Each point is a single well and the bar is the mean across two independent experiments.
(B) Representative histograms of $\Delta\psi_m$ from BMDMs untreated or treated with 500 U/mL IFNβ or 10 ng/mL LPS for 48 hours.
(C) Quantification of $\Delta\psi_m$ derived from (B). The TMRM/MTG ratio was normalized to the mean of uninfected wells. Each point is a single well and the bar is the mean from three experiments.

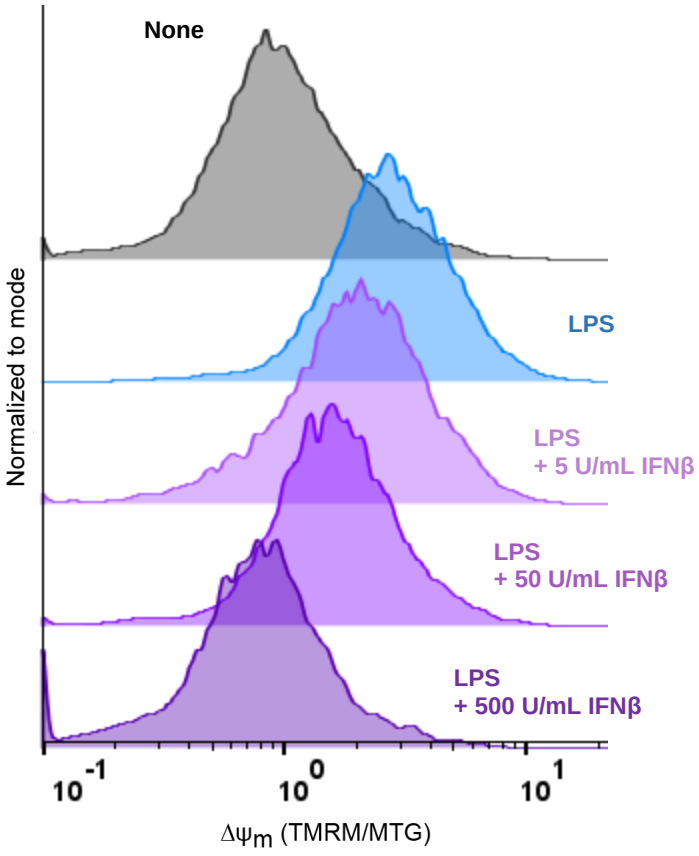


**Figure IV.13 IFNβ decreases LPS-driven mitochondrial hyperpolarization**
Representative histograms of $\Delta\psi_m$ from BMDMs untreated or treated with 10 ng/mL LPS by itself or with increasing doses of IFNβ. All treatments were for 48 hours. Representative histograms of two biological replicates from a single experiment (5 and 50 U/mL IFNβ) or from two experiments (500 U/mL IFNβ).

As mentioned above, the transcriptional response of BMDM to prolonged IFNβ treatment includes downregulation of many metabolic pathways (Figure III.11). The most downregulated genes in pathways related to OXPHOS include all 13 genes encoded proteins on mtDNA, which we validated for two genes by RT-qPCR (Figure IV.14).

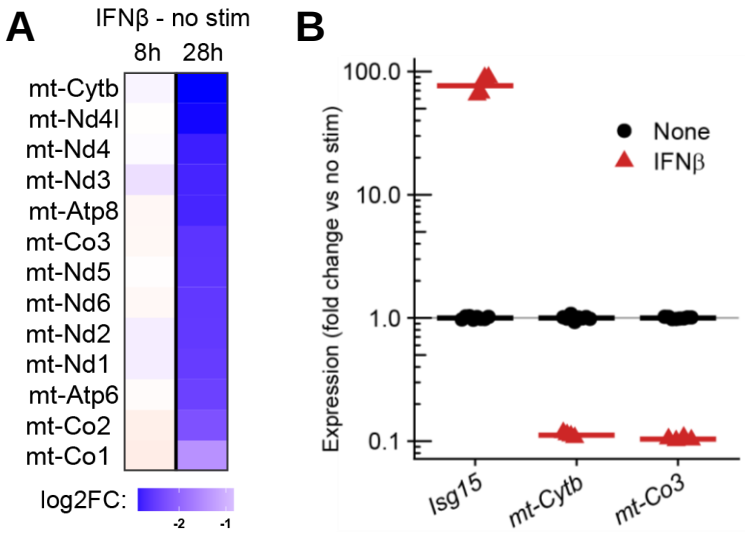


**Figure IV.14 IFNβ decreases transcription of mitochondrial genes**
(A) Log2FC in expression (RNA-seq) of the 13 protein coding genes encoded on mtDNA in WT BMDM treated with 500 U/mL IFNβ compared to untreated cells for the indicated time.
(B) Expression of *Isg15*, *mt-Cytb*, or *mt-Co3* was measured with RT-qPCR in WT BMDM either untreated (black circles) or treated with 500 U/mL IFNβ for 24 hours. Expression normalized to the housekeeping gene *Eef1a1*. Two independent experiments shown.

Since the changes described above suggested profound mitochondrial damage, we directly quantified one common outcome of such damage, the accumulation of mROS. IFNβ treatment of BMDM increases mROS at 24 and 48 hours by signaling through IFNAR (Figure IV.15). Taken together, the functional changes in the setting of single cell measurements of mitochondrial dysfunction supports the conclusion that IFNβ signaling through IFNAR leads to many hallmarks of mitochondrial damage in BMDM.

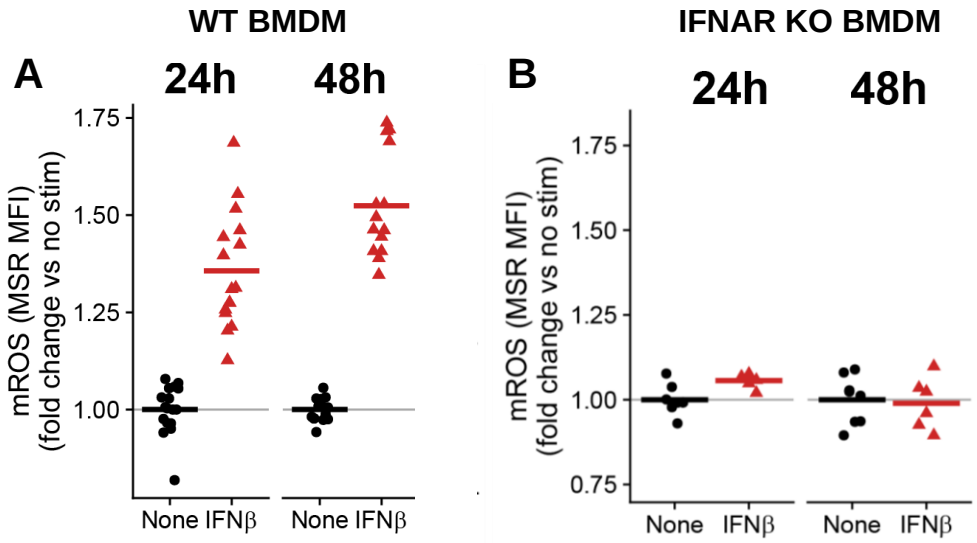


**Figure IV.15 IFNβ induces accumulation of mROS in BMDM by signaling through IFNAR**
(A,B) Quantification of mitochondrial reactive oxygen species (mROS) in WT BMDM (A) or IFNAR KO BMDM (B) untreated or treated with 500 U/mL IFNβ for indicated times. mROS measured with MitoSOX Red (MSR) MFI normalized to untreated controls at each timepoint. Each point represents a single well and the bar is the mean from five (A) or two (B) independent experiments.

## Discussion

Since the metabolic profile we observed during live Mtb infection (Chapter III) has not been reported previously as an outcome of type I IFN signaling in macrophages as far as we know, in this Chapter we characterized the metabolic alterations in macrophages after type I IFN treatment. We describe a metabolic response to type I IFN itself that mirrors that to live H37Rv; IFNβ treatment impairs mitochondrial function and restrains glycolysis.

The study of the modulation of metabolism by type I IFN is in its infancy, but it is clear that this cytokine family can have drastically different metabolic consequences in different cell types (Burke et al., 2014; Kissig et al., 2017; Pantel et al., 2014; Wu et al., 2016). The effects of type I IFN on macrophage energy metabolism have not been explored thoroughly, although intriguing interactions exist between type I IFN and macrophage cholesterol homeostasis (Blanc et al., 2011, 2013; York et al., 2015). Although a recent report showed that macrophages have divergent metabolic responses to different TLR ligands that are known to differentially induce

type I IFN, the authors did not explore the direct contributions of type I IFN (Ahmed et al., 2019). Recent studies implicate type I IFN in macrophage metabolic changes during intracellular bacterial infections (Hos et al., 2017; Howard et al., 2018), but rely on indirect evidence.

The characterization of IFNβ's effect on macrophage metabolism in this Chapter highlights two main conclusions: IFNβ itself induces a metabolic state that does not fit into the current immunometabolic dichotomy (LPS vs IL-4 stimulation) and it restrains the inflammatory glycolytic shift of macrophages stimulated with TLR ligands. We believe that these findings have wide-ranging implications, not only for understanding the roles of type I IFN and immunometabolism in Mtb pathogenesis, but more broadly in extending current immunometabolic models derived from studies with single purified stimuli to diseases that include robust type I IFN signaling (including COVID-19) (Ayres, 2020; Bastard et al., 2020; Zhang et al., 2020).

# Chapter V: Conclusions and perspectives

For a long time, immunologists focused on a relatively small subset of the interactions between humans and microbes: those between humans and the pathogens that actively cause disease. This focus led to an accumulation of evidence that supported the view of “Nature, red in tooth and claw” (Tennyson, 1850). Pathogenic virulence factors are pitted against “killer” cells wielding an impressive panoply of immunological weaponry. Although some of the first immune cells described were the innate immune macrophages, the T and B adaptive immune cells quickly dominated the research of 20$^{th}$ century immunologists. A key feature of the adaptive immune system—the discrimination between human (self) and microbial (non-self)—became a central tenet of the field of immunology.

This tenet motivated early efforts to understand innate immune cells and their interactions with adaptive immune cells. A massive research effort produced many examples that supported this view: the immune system employs numerous pattern-recognition receptors (PRRs) to recognize non-self molecular patterns (Janeway, 1989; Medzhitov, 2009). The original name given to these non-self molecular patterns (pathogen associated molecular patterns) highlights the singular focus on pathogens of early immunology.

More recent studies—especially in the emerging fields of the microbiome (Ayres, 2016; Thaiss et al., 2016) and immunological tolerance (Schneider and Ayres, 2008)—have added new perspectives to our understanding of the immune system. The relationships between humans and microbes are incredibly varied, extraordinarily complex, and highly dynamic. The human immune system is not just tasked with recognizing and destroying microbes but must perform the difficult job of protecting us from potential pathogens while also tolerating and even supporting the harmless or beneficial commensals that surround us. In order to understand our immune system (and indeed the many diseases that immune failure contributes to), we must study all facets of the biological relationship between humans and microbes.

Indeed, even the relationship between humans and one single bacterial species, *Mycobacterium tuberculosis* (Mtb), can span a wide spectrum (Esmail et al., 2014; Pai et al., 2016). Chapter II discusses a new mouse model that explores an understudied aspect of the relationship: how asymptomatic latent TB infection (LTBI) alters the biology of the host. We report that contained Mtb infection in the mouse can provide immunological benefits to the host, including protection against subsequent aerosol infection with Mtb and heterologous challenges with *Listeria* or melanoma. Although this is consistent with previous epidemiological studies (Andrews et al., 2012) and genetic analyses (Comas et al., 2013) in humans, current research has focused almost exclusively on the reactivation of LTBI into active disease. This focus has neglected the important questions of how LTBI itself shapes human biology. When we investigated the effects of LTBI in a cohort of humans who are infected with HIV, we observed evidence for similar beneficial effects as those described in Chapter II. Specifically, LTBI status is associated with a lower HIV viral load and decreased risk of opportunistic infections in this human cohort (Kusejko et al., 2020).

Many pressing questions remain about the CMTB model. Although we identified IFNγ signaling as important in the immune activation observed, direct interrogation of mechanistic connections to the protective phenotype is challenging in a full animal model. In particular, because the immune system contributes to containment of Mtb within the cervical lymph node, immunological interventions are limited to those that do not disrupt containment. Furthermore, our incomplete understanding of the signals involved in the macrophage response to Mtb limits the targeted hypotheses that can be tested in this setting. For example, investigating whether and how the immune system discriminates between “pathogenic” Mtb during fulminant pulmonary infection and “microbial” Mtb during containment requires that the fundamental interactions between macrophages and Mtb be better characterized.

The appreciation that the innate immune system must discriminate pathogens from harmless microbes has rejuvenated the search for signals beyond simple microbial pattern recognition that control immune activation (Vance et al., 2009). One promising avenue of research has been the metabolic pathways and metabolic stress signals that rewire the immune system in both protective and harmful ways (Buck et al., 2017; O'Neill and Pearce, 2016). In fact, mitochondria, the evolutionary end-product of microbial cooperation, integrate many metabolic pathways and canonical immune signaling.

Recent studies have made incredible progress towards untangling the molecular metabolic mechanisms downstream of immune receptor activation. However, most of these studies have only used purified immune stimuli (e.g. LPS) and translation to more complex host-microbial interactions has proven difficult (Russell et al., 2019). The restrictions required for working with the deadliest live pathogens has compounded the problem; the extrapolation of studies using inactivated pathogens—which indicate metabolic responses that conform to the aerobic glycolysis induced by LPS—has sown confusion (Cumming et al., 2020; Gleeson and Sheedy, 2016). The discrepancies between the metabolic responses to live pathogens and current models of immunometabolism are most often explained away without strong evidence by invoking pathogen virulence processes, which avoids the hard question: are we studying the receptors that actually control the metabolic response to pathogens?

Chapter III begins with the premise that identifying mechanisms underlying immunometabolism during Mtb infection would help the field focus on pathways more relevant to clinical infectious diseases. Surprisingly, we determined that type I interferon, a family of cytokines central to the pathophysiology of diverse diseases, controls macrophage metabolism during Mtb infection both *in vitro* and, importantly, *in vivo*.

Chapter IV strengthens the case for a causal role of type I IFN in macrophage metabolism by thoroughly characterizing the metabolic changes effected by IFNβ treatment

itself. IFNβ leads to a metabolic state that mirrors Mtb infection: hypopolarized, dysfunction mitochondria and decreased glycolytic flux. Future studies are needed to dissect the signaling events that connect IFNAR ligation with this profound metabolic reprogramming. Interestingly, IFNγ signaling in macrophages—which shares many molecular intermediates with IFNβ pathways—establishes very different metabolic programs (Cameron et al., 2019; van Teijlingen Bakker and Pearce, 2020). In addition, different immune cell subtypes display very different metabolic responses to type I IFNs (Everts et al., 2014; Wu et al., 2016). Comparative studies (across IFN families and cell subtypes) should be fruitful to unravel which of the hundreds of changes downstream of type I IFN drive the metabolic changes.

The seminal discovery that type I IFN is induced downstream of mitochondrial stress reinvigorated the study of interactions between immunity and metabolism (West et al., 2015). The findings presented in Chapters III and IV place type I IFN also upstream of mitochondrial stress. We used STING KO mice to directly test the predictions of this revised model with type I IFN and mitochondria forming a positive feedback loop in macrophages. We hope that this proposed feedback loop will inspire new avenues of research to understand IFN induction in macrophages across disease states.

In summary, this dissertation explores mouse models of *Mycobacterium tuberculosis* at both the organismal and molecular scales in order to better understand how mammalian immune systems interact with the vast microbial world. As always, exploration finds more questions than answers, but I am convinced that it is only in investigating all facets of the relationships between humans and microbes that we can fully understand ourselves.

# References


Aagaard, C., Hoang, T., Dietrich, J., Cardona, P.J., Izzo, A., Dolganov, G., Schoolnik, G.K., Cassidy, J.P., Billeskov, R., and Andersen, P. (2011). A multistage tuberculosis vaccine that confers efficient protection before and after exposure. Nat. Med. *17*, 189–195.

Abarca-Rojano, E., Rosas-Medina, P., Zamudio-Cortez, P., Mondragon-Flores, R., and Sanchez-Garcia, F.J. (2003). Mycobacterium tuberculosis Virulence Correlates with Mitochondrial Cytochrome c Release in Infected Macrophages. Scand. J. Immunol. *58*, 419–427.

Aderem, A.A., Scott, W.A., and Cohn, Z.A. (1986). Evidence for sequential signals in the induction of the arachidonic acid cascade in macrophages. J. Exp. Med. *163*.

Ahmed, D., Jaworski, A., Roy, D., Willmore, W., Golshani, A., and Cassol, E. (2018). Transcriptional profiling suggests extensive metabolic rewiring of human and mouse macrophages during early interferon alpha responses. Mediators Inflamm. *Jul 25*, doi:10.1155/2018/5906819.

Ahmed, D., Roy, D., Jaworski, A., Edwards, A., Abizaid, A., Kumar, A., Golshani, A., and Cassol, E. (2019). Differential remodeling of the electron transport chain is required to support TLR3 and TLR4 signaling and cytokine production in macrophages. Sci. Rep. *9*, 1–13.

Andersen, P., and Kaufmann, S.H.E. (2014). Novel Vaccination Strategies against Tuberculosis. Cold Spring Harb. Perspect. Med. *4*, a018523–a018523.

Andrews, J.R., Noubary, F., Walensky, R.P., Cerda, R., Losina, E., and Horsburgh, C.R. (2012). Risk of progression to active tuberculosis following reinfection with Mycobacterium tuberculosis. Clin. Infect. Dis. *54*, 784–791.

Antonelli, L.R.V., Rothfuchs, A.G., Gonçalves, R., Roffê, E., Cheever, A.W., Bafica, A., Salazar, A.M., Feng, C.G., and Sher, A. (2010). Intranasal poly-IC treatment exacerbates tuberculosis in mice through the pulmonary recruitment of a pathogen-permissive monocyte/macrophage population. J. Clin. Invest. *120*, 1674–1682.

Ayres, J.S. (2016). Cooperative microbial tolerance behaviors in host-microbiota mutualism. Cell *165*, 1323–1331.

Ayres, J.S. (2020). A metabolic handbook for the COVID-19 pandemic. Nat. Metab. *2*, 572–585.

Barry, C.E., Boshoff, H.I., Dartois, V., Dick, T., Ehrt, S., Flynn, J.A., Schnappinger, D., Wilkinson, R.J., and Young, D. (2009). The spectrum of latent tuberculosis: Rethinking the biology and intervention strategies. Nat. Rev. Microbiol. *7*, 845–855.

Bastard, P., Rosen, L.B., Zhang, Q., Michailidis, E., Hoffmann, H.H., Zhang, Y., Dorgham, K., Philippot, Q., Rosain, J., Béziat, V., et al. (2020). Autoantibodies against type I IFNs in patients with life-threatening COVID-19. Science (80-. ). *370*.

Behr, M.A., and Waters, W.R. (2014). Is tuberculosis a lymphatic disease with a pulmonary portal? Lancet Infect. Dis. *14*, 250–255.

Belkaid, Y., Piccirillo, C.A., Mendez, S., Shevach, E.M., and Sacks, D.L. (2002). CD4+CD25+ regulatory T cells control Leishmania major persistence and immunity. Nature *420*, 502–507.

Berry, M.P.R., Graham, C.M., McNab, F.W., Xu, Z., Bloch, S.A.A., Oni, T., Wilkinson, K.A., Banchereau, R., Skinner, J., Wilkinson, R.J., et al. (2010). An interferon-inducible neutrophil-

driven blood transcriptional signature in human tuberculosis. Nature *466*, 973–977.

Blanc, M., Hsieh, W.Y., Robertson, K.A., Watterson, S., Shui, G., Lacaze, P., Khondoker, M., Dickinson, P., Sing, G., Rodríguez-Martín, S., et al. (2011). Host defense against viral infection involves interferon mediated down-regulation of sterol biosynthesis. PLoS Biol. *9*, e1000598.

Blanc, M., Hsieh, W.Y., Robertson, K.A., Kropp, K.A., Forster, T., Shui, G., Lacaze, P., Watterson, S., Griffiths, S.J., Spann, N.J., et al. (2013). The Transcription Factor STAT-1 Couples Macrophage Synthesis of 25-Hydroxycholesterol to the Interferon Antiviral Response. Immunity *38*, 106–118.

Blaser, N., Zahnd, C., Hermans, S., Salazar-Vizcaya, L., Estill, J., Morrow, C., Egger, M., Keiser, O., and Wood, R. (2016). Tuberculosis in Cape Town: An age-structured transmission model. Epidemics *14*, 54–61.

Brown, S.P., and Grenfell, B.T. (2001). An unlikely partnership: Parasites, concomitant immunity and host defence. Proc. R. Soc. B Biol. Sci. *268*, 2543–2549.

Buck, M.D., Sowell, R.T., Kaech, S.M., and Pearce, E.L. (2017). Metabolic Instruction of Immunity. Cell *169*, 570–586.

Buenrostro, J.D., Wu, B., Chang, H.Y., and Greenleaf, W.J. (2015). ATAC-seq: A method for assaying chromatin accessibility genome-wide. Curr. Protoc. Mol. Biol. *2015*, 21.29.1-21.29.9.

Bulua, A.C., Simon, A., Maddipati, R., Pelletier, M., Park, H., Kim, K.-Y., Sack, M.N., Kastner, D.L., and Siegel, R.M. (2011). Mitochondrial reactive oxygen species promote production of proinflammatory cytokines and are elevated in TNFR1-associated periodic syndrome (TRAPS). J. Exp. Med. *208*, 519–533.

Burke, J.D., Platanias, L.C., and Fish, E.N. (2014). Beta Interferon Regulation of Glucose Metabolism Is PI3K/Akt Dependent and Important for Antiviral Activity against Coxsackievirus B3. J. Virol. *88*, 3485–3495.

Cadena, A.M., Hopkins, F.F., Maiello, P., Carey, A.F., Wong, E.A., Martin, C.J., Gideon, H.P., DiFazio, R.M., Andersen, P., Lin, P.L., et al. (2018). Concurrent infection with Mycobacterium tuberculosis confers robust protection against secondary infection in macaques. PLoS Pathog. *14*, e1007305.

Cadieux, N., Parra, M., Cohen, H., Maric, D., Morris, S.L., and Brennan, M.J. (2011). Induction of cell death after localization to the host cell mitochondria by the Mycobacterium tuberculosis PE_PGRS33 protein. Microbiology *157*, 793–804.

Cameron, A.M., Castoldi, A., Sanin, D.E., Flachsmann, L.J., Field, C.S., Puleston, D.J., Kyle, R.L., Patterson, A.E., Hässler, F., Buescher, J.M., et al. (2019). Inflammatory macrophage dependence on NAD + salvage is a consequence of reactive oxygen species–mediated DNA damage. Nat. Immunol. *20*, 420–432.

Chandel, N.S., Schumacker, P.T., and Arch, R.H. (2001). Reactive Oxygen Species Are Downstream Products of TRAF-mediated Signal Transduction. J. Biol. Chem. *276*, 42728–42736.

Chen, M., Gan, H., and Remold, H.G. (2006a). A mechanism of virulence: virulent Mycobacterium tuberculosis strain H37Rv, but not attenuated H37Ra, causes significant mitochondrial inner membrane disruption in macrophages leading to necrosis. J. Immunol. *176*, 3707–3716.

Chen, M., Gan, H., and Remold, H.G. (2006b). A Mechanism of Virulence: Virulent Mycobacterium tuberculosis Strain H37Rv, but Not Attenuated H37Ra, Causes Significant Mitochondrial Inner Membrane Disruption in Macrophages Leading to Necrosis. J. Immunol. *176*, 3707–3716.

Chen, X., Shen, Y., Draper, W., Buenrostro, J.D., Litzenburger, U., Cho, S.W., Satpathy, A.T., Carter, A.C., Ghosh, R.P., East-Seletsky, A., et al. (2016). ATAC-see reveals the accessible genome by transposase-mediated imaging and sequencing. Nat. Methods *13*, 1013–1020.

Cheng, Y., and Schorey, J.S. (2018). Mycobacterium tuberculosis –induced IFN-β production requires cytosolic DNA and RNA sensing pathways. J. Exp. Med. *215*, 2919–2935.

Cheng, S.C., Quintin, J., Cramer, R.A., Shepardson, K.M., Saeed, S., Kumar, V., Giamarellos-Bourboulis, E.J., Martens, J.H.A., Rao, N.A., Aghajanirefah, A., et al. (2014). mTOR- and HIF-1α-mediated aerobic glycolysis as metabolic basis for trained immunity. Science *345*.

Cohen, S.B., Gern, B.H., Delahaye, J.L., Adams, K.N., Plumlee, C.R., Winkler, J.K., Sherman, D.R., Gerner, M.Y., and Urdahl, K.B. (2018). Alveolar Macrophages Provide an Early Mycobacterium tuberculosis Niche and Initiate Dissemination. Cell Host Microbe *24*, 439-446.e4.

Cohn, Z.A. (1981). The macrophage--versatile element of inflammation. Harvey Lect. *77*, 63–80.

Collins, A.C., Cai, H., Li, T., Franco, L.H., Li, X.D., Nair, V.R., Scharn, C.R., Stamm, C.E., Levine, B., Chen, Z.J., et al. (2015). Cyclic GMP-AMP Synthase Is an Innate Immune DNA Sensor for Mycobacterium tuberculosis. Cell Host Microbe *17*, 820–828.

Comas, I., Coscolla, M., Luo, T., Borrell, S., Holt, K.E., Kato-Maeda, M., Parkhill, J., Malla, B., Berg, S., Thwaites, G., et al. (2013). Out-of-Africa migration and Neolithic coexpansion of Mycobacterium tuberculosis with modern humans. Nat. Genet. *45*, 1176–1182.

Cooper, A.M., Dalton, D.K., Stewart, T.A., Griffin, J.P., Russell, D.G., and Orme, I.M. (1993). Disseminated tuberculosis in interferon γ Gene-disrupted mice. J. Exp. Med. *178*, 2243–2247.

Cooper, A.M., Magram, J., Ferrante, J., and Orme, I.M. (1997). Interleukin 12 (IL-12) is crucial to the development of protective immunity in mice intravenously infected with mycobacterium tuberculosis. J. Exp. Med. *186*, 39–45.

Cumming, B.M., Rahman, M.A., Lamprecht, D.A., Rohde, K.H., Saini, V., Adamson, J.H., Russell, D.G., and Steyn, A.J.C. (2017). Mycobacterium tuberculosis arrests host cycle at the G1/S transition to establish long term infection. PLoS Pathog. *13*, e1006389.

Cumming, B.M., Addicott, K.W., Adamson, J.H., and Steyn, A.J.C. (2018). Mycobacterium tuberculosis induces decelerated bioenergetic metabolism in human macrophages. Elife *7*.

Cumming, B.M., Pacl, H.T., and Steyn, A.J.C. (2020). Relevance of the Warburg Effect in Tuberculosis for Host-Directed Therapy. Front. Cell. Infect. Microbiol. *10*, 1–13.

Decker, T., Müller, M., and Stockinger, S. (2005). The Yin and Yang of type I interferon activity in bacterial infection. Nat. Rev. Immunol. *5*, 675–687.

Deffert, C., Cachat, J., and Krause, K.-H. (2014). Phagocyte NADPH oxidase, chronic granulomatous disease and mycobacterial infections. Cell. Microbiol. *16*, 1168–1178.

Delahaye, J.L., Gern, B.H., Cohen, S.B., Plumlee, C.R., Shafiani, S., Gerner, M.Y., and Urdahl, K.B. (2019). Cutting Edge: Bacillus Calmette–Guérin–Induced T Cells Shape Mycobacterium

tuberculosis Infection before Reducing the Bacterial Burden. J. Immunol. *203*, 807–812.

Diamond, M.S., and Farzan, M. (2013). The broad-spectrum antiviral functions of IFIT and IFITM proteins. Nat. Rev. Immunol. *13*, 46–57.

Doolan, D.L., Dobaño, C., and Baird, J.K. (2009). Acquired immunity to Malaria. Clin. Microbiol. Rev. *22*, 13–36.

Dorhoi, A., Yeremeev, V., Nouailles, G., Weiner, J., Jörg, S., Heinemann, E., Oberbeck-Müller, D., Knaul, J.K., Vogelzang, A., Reece, S.T., et al. (2014). Type I IFN signaling triggers immunopathology in tuberculosis-susceptible mice by modulating lung phagocyte dynamics. Eur. J. Immunol. *44*, 2380–2393.

Duan, L., Yi, M., Chen, J., Li, S., and Chen, W. (2016). Mycobacterium tuberculosis EIS gene inhibits macrophage autophagy through up-regulation of IL-10 by increasing the acetylation of histone H3. Biochem. Biophys. Res. Commun. *473*, 1229–1234.

Dunham, I., Kundaje, A., Aldred, S.F., Collins, P.J., Davis, C. a., Doyle, F., Epstein, C.B., Frietze, S., Harrow, J., Kaul, R., et al. (2012). An integrated encyclopedia of DNA elements in the human genome. Nature *489*, 57–74.

Dutta, N.K., and Karakousis, P.C. (2014). Latent Tuberculosis Infection: Myths, Models, and Molecular Mechanisms. Microbiol. Mol. Biol. Rev. *78*, 343–371.

Eisenreich, W., Rudel, T., Heesemann, J., and Goebel, W. (2019). How viral and intracellular bacterial pathogens reprogram the metabolism of host cells to allow their intracellular replication. Front. Cell. Infect. Microbiol. *9*, 42.

Esmail, H., Barry, C.E., Young, D.B., and Wilkinson, R.J. (2014). The ongoing challenge of latent tuberculosis. Philos. Trans. R. Soc. B Biol. Sci. *369*, 20130437.

Everts, B., Amiel, E., Huang, S.C.C., Smith, A.M., Chang, C.H., Lam, W.Y., Redmann, V., Freitas, T.C., Blagih, J., Van Der Windt, G.J.W., et al. (2014). TLR-driven early glycolytic reprogramming via the kinases TBK1-IKKε supports the anabolic demands of dendritic cell activation. Nat. Immunol. *15*, 323–332.

Federico, A., and Monti, S. (2020). HypeR: An R package for geneset enrichment workflows. Bioinformatics *36*, 1307–1308.

Flynn, J.A.L., Chan, J., Triebold, K.J., Dalton, D.K., Stewart, T.A., and Bloom, B.R. (1993). An essential role for interferon γ in resistance to mycobacterium tuberculosis infection. J. Exp. Med. *178*, 2249–2254.

Flynn, J.A.L., Goldstein, M.M., Chan, J., Triebold, K.J., Pfeffer, K., Lowenstein, C.J., Schrelber, R., Mak, T.W., and Bloom, B.R. (1995). Tumor necrosis factor-α is required in the protective immune response against mycobacterium tuberculosis in mice. Immunity *2*, 561–572.

Fortin, A., Abel, L., Casanova, J.L., and Gros, P. (2007). Host genetics of mycobacterial diseases in mice and men: Forward genetic studies of BCG-osis and tuberculosis. Annu. Rev. Genomics Hum. Genet. *8*, 163–192.

Furin, J., Cox, H., and Pai, M. (2019). Tuberculosis. Lancet *393*, 1642–1656.

Ganchua, S.K.C., Cadena, A.M., Maiello, P., Gideon, H.P., Myers, A.J., Junecko, B.F., Klein, E.C., Lin, P.L., Mattila, J.T., and Flynn, J.L. (2018). Lymph nodes are sites of prolonged bacterial persistence during Mycobacterium tuberculosis infection in macaques. PLOS Pathog.

*14*, e1007337.

Garaude, J., Acin-Perez, R., Martínez-Cano, S., Enamorado, M., Ugolini, M., Nistal-Villán, E., Hervás-Stubbs, S., Pelegrín, P., Sander, L., Enríquez, J.A., et al. (2016). Mitochondrial respiratory-chain adaptations in macrophages contribute to antibacterial host defense. Nat. Immunol. *17*, 1037–1045.

Geng, J., Sun, X., Wang, P., Zhang, S., Wang, X., Wu, H., Hong, L., Xie, C., Li, X., Zhao, H., et al. (2015). Kinases Mst1 and Mst2 positively regulate phagocytic induction of reactive oxygen species and bactericidal activity. Nat. Immunol. *16*, 1142–1152.

Giacomini, E., Remoli, M.E., Gafa, V., Pardini, M., Fattorini, L., and Coccia, E.M. (2009). IFN-β improves BCG immunogenicity by acting on DC maturation. J. Leukoc. Biol. *85*, 462–468.

Ginhoux, F., and Guilliams, M. (2016). Tissue-Resident Macrophage Ontogeny and Homeostasis. Immunity *44*, 439–449.

Giosuè, S., Casarini, M., Alemanno, L., Galluccio, G., Mattia, P., Pedicelli, G., Rebek, L., Bisetti, A., and Ameglio, F. (1998). Effects of aerosolized interferon-α in patients with pulmonary tuberculosis. Am. J. Respir. Crit. Care Med. *158*, 1156–1162.

Gleeson, L.E., and Sheedy, F.J. (2016). Metabolic reprogramming & inflammation: Fuelling the host response to pathogens. Semin. Immunol. *28*, 450–468.

Gleeson, L.E., Sheedy, F.J., Palsson-McDermott, E.M., Triglia, D., O'Leary, S.M., O'Sullivan, M.P., O'Neill, L.A.J., and Keane, J. (2016). Cutting Edge: Mycobacterium tuberculosis Induces Aerobic Glycolysis in Human Alveolar Macrophages That Is Required for Control of Intracellular Bacillary Replication. J. Immunol. *196*, 2444–2449.

Goodridge, H.S., Ahmed, S.S., Curtis, N., Kollmann, T.R., Levy, O., Netea, M.G., Pollard, A.J., van Crevel, R., and Wilson, C.B. (2016). Harnessing the beneficial heterologous effects of vaccination. Nat. Rev. Immunol. *16*, 392–400.

Gordon, S., and Cohn, Z.A. (1973). The Macrophage. Int. Rev. Cytol. *36*, 171–214.

Grode, L., Seiler, P., Baumann, S., Hess, J., Brinkmann, V., Eddine, A.N., Mann, P., Goosmann, C., Bandermann, S., Smith, D., et al. (2005). Increased vaccine efficacy against tuberculosis of recombinant Mycobacterium bovis bacille Calmette-Guérin mutants that secrete listeriolysin. J. Clin. Invest. *115*, 2472–2479.

Gröschel, M.I., Sayes, F., Shin, S.J., Frigui, W., Pawlik, A., Orgeur, M., Canetti, R., Honoré, N., Simeone, R., van der Werf, T.S., et al. (2017). Recombinant BCG Expressing ESX-1 of Mycobacterium marinum Combines Low Virulence with Cytosolic Immune Signaling and Improved TB Protection. Cell Rep. *18*, 2752–2765.

Hackett, E.E., Charles-Messance, H., O'Leary, S.M., Gleeson, L.E., Muñoz-Wolf, N., Case, S., Wedderburn, A., Johnston, D.G.W., Williams, M.A., Smyth, A., et al. (2020). Mycobacterium tuberculosis Limits Host Glycolysis and IL-1β by Restriction of PFK-M via MicroRNA-21. Cell Rep. *30*, 124-136.e4.

Hartigan, J.A., and Wong, M.A. (1979). Algorithm AS 136 : A K-Means Clustering Algorithm. Appl. Stat. *28*, 100–108.

Harty, J.T., and Bevan, M.J. (1995). Specific immunity to listeria monocytogenes in the absence of IFNγ. Immunity *3*, 109–117.

Hawn, T.R., Matheson, A.I., Maley, S.N., and Vandal, O. (2013). Host-Directed Therapeutics for Tuberculosis: Can We Harness the Host? Microbiol. Mol. Biol. Rev. *77*, 608–627.

Hernández-Pando, R., Jeyanathan, M., Mengistu, G., Aguilar, D., Orozco, H., Harboe, M., Rook, G.A.W., and Bjune, G. (2000). Persistence of DNA from Mycobacterium tuberculosis in superficially normal lung tissue during latent infection. Lancet *356*, 2133–2138.

Higgins, J.P.T., Soares-Weiser, K., López-López, J.A., Kakourou, A., Chaplin, K., Christensen, H., Martin, N.K., Sterne, J.A.C., and Reingold, A.L. (2016). Association of BCG, DTP, and measles containing vaccines with childhood mortality: systematic review. BMJ *355*, i5170.

Hopfner, K.P., and Hornung, V. (2020). Molecular mechanisms and cellular functions of cGAS–STING signalling. Nat. Rev. Mol. Cell Biol. *21*, 501–521.

Hos, N.J., Ganesan, R., Gutiérrez, S., Hos, D., Klimek, J., Abdullah, Z., Krönke, M., and Robinson, N. (2017). Type I interferon enhances necroptosis of Salmonella Typhimurium-infected macrophages by impairing antioxidative stress responses. J. Cell Biol. *216*, 4107–4121.

Houben, R.M.G.J., and Dodd, P.J. (2016). The Global Burden of Latent Tuberculosis Infection: A Re-estimation Using Mathematical Modelling. PLOS Med. *13*, e1002152.

Howard, N.C., and Khader, S.A. (2020). Immunometabolism during Mycobacterium tuberculosis Infection. Trends Microbiol. *28*, 832–850.

Howard, N.C., Marin, N.D., Ahmed, M., Rosa, B.A., Martin, J., Bambouskova, M., Sergushichev, A., Loginicheva, E., Kurepina, N., Rangel-Moreno, J., et al. (2018). Mycobacterium tuberculosis carrying a rifampicin drug resistance mutation reprograms macrophage metabolism through cell wall lipid changes. Nat. Microbiol. *3*, 1099–1108.

Huaman, M.A., Deepe, Jr., G.S., and Fichtenbaum, C.J. (2016). Elevated Circulating Concentrations of Interferon-Gamma in Latent Tuberculosis Infection. Pathog. Immun. *1*, 291.

Huang, L., Nazarova, E. V, Tan, S., Liu, Y., and Russell, D.G. (2018). Growth of Mycobacterium tuberculosis in vivo segregates with host macrophage metabolism and ontogeny. J. Exp. Med. *215*, 1135–1152.

Ip, W.K.E., Hoshi, N., Shouval, D.S., Snapper, S., and Medzhitov, R. (2017). Anti-inflammatory effect of IL-10 mediated by metabolic reprogramming of macrophages. Science *356*, 513–519.

Jamwal, S., Midha, M.K., Verma, H.N., Basu, A., Rao, K.V.S., and Manivel, V. (2013). Characterizing virulence-specific perturbations in the mitochondrial function of macrophages infected with Mycobacterium tuberculosis. Sci. Rep. *3*, 1328.

Janeway, C.A. (1989). Approaching the Asymptote? Evolution and Revolution in Immunology. Cold Spring Harb. Symp. Quant. Biol. *54*, 1–13.

Jensen, K.J., Larsen, N., Sørensen, S.B., Andersen, A., Eriksen, H.B., Monteiro, I., Hougaard, D., Aaby, P., Netea, M.G., Flanagan, K.L., et al. (2015). Heterologous immunological effects of early BCG vaccination in low-birth-weight infants in guinea-bissau: A randomized-controlled trial. J. Infect. Dis. *211*, 956–967.

Jin, Z., Wei, W., Yang, M., Du, Y., and Wan, Y. (2014). Mitochondrial complex I activity suppresses inflammation and enhances bone resorption by shifting macrophage-osteoclast polarization. Cell Metab. *20*, 483–498.

Jouanguy, E., Lamhamedi-Cherradi, S., Lammas, D., Dorman, S.E., Fondanèche, M.C., Dupuis,

S., Döffinger, R., Altare, F., Girdlestone, J., Emile, J.F., et al. (1999). A human IFNGR1 small deletion hotspot associated with dominant susceptibility to mycobacterial infection. Nat. Genet. *21*, 370–378.

Kaufmann, E., Sanz, J., Dunn, J.L., Khan, N., Mendonça, L.E., Pacis, A., Tzelepis, F., Pernet, E., Dumaine, A., Grenier, J.C., et al. (2018). BCG Educates Hematopoietic Stem Cells to Generate Protective Innate Immunity against Tuberculosis. Cell *172*, 176-190.e19.

Kaufmann, S.H.E., Lange, C., Rao, M., Balaji, K.N., Lotze, M., Schito, M., Zumla, A.I., and Maeurer, M. (2014). Progress in tuberculosis vaccine development and host-directed therapies-a state of the art review. Lancet Respir. Med. *2*, 301–320.

Khan, N., Downey, J., Sanz, J., Kaufmann, E., Blankenhaus, B., Pacis, A., Pernet, E., Ahmed, E., Cardoso, S., Nijnik, A., et al. (2020). M. tuberculosis Reprograms Hematopoietic Stem Cells to Limit Myelopoiesis and Impair Trained Immunity. Cell *183*, 752-770.e22.

Khare, A., Raundhal, M., Chakraborty, K., Das, S., Corey, C., Kamga, C.K., Quesnelle, K., St. Croix, C., Watkins, S.C., Morse, C., et al. (2016). Mitochondrial H2O2in Lung Antigen-Presenting Cells Blocks NF-κB Activation to Prevent Unwarranted Immune Activation. Cell Rep. *15*, 1700–1714.

Kissig, M., Ishibashi, J., Harms, M.J., Lim, H.-W., Stine, R.R., Won, K.-J., and Seale, P. (2017). PRDM16 represses the type I interferon response in adipocytes to promote mitochondrial and thermogenic programing. EMBO J. *36*, 1528–1542.

Kupz, A., Zedler, U., Stäber, M., Kaufmann, S.H.E., Raupach, B., and Enders, J. (2016). A Mouse Model of Latent Tuberculosis Infection to Study Intervention Strategies to Prevent Reactivation. PLoS One *11*, e0158849.

Kusejko, K., Gunthard, H.F., Olson, G.S., Zens, K., Darling, K., Khanna, N., Furrer, H., Vetter, P., Bernasconi, E., Vernazza, P., et al. (2020). Diagnosis of latent tuberculosis infection is associated with reduced HIV viral load and lower risk for opportunistic infections in people living with HIV. PLoS Biol. *18*.

Lachmandas, E., Boutens, L., Ratter, J.M., Hijmans, A., Hooiveld, G.J., Joosten, L.A.B., Rodenburg, R.J., Fransen, J.A.M., Houtkooper, R.H., Van Crevel, R., et al. (2016a). Microbial stimulation of different Toll-like receptor signalling pathways induces diverse metabolic programmes in human monocytes. Nat. Microbiol. *2*, 16246.

Lachmandas, E., Beigier-Bompadre, M., Cheng, S.C., Kumar, V., van Laarhoven, A., Wang, X., Ammerdorffer, A., Boutens, L., de Jong, D., Kanneganti, T.D., et al. (2016b). Rewiring cellular metabolism via the AKT/mTOR pathway contributes to host defence against Mycobacterium tuberculosis in human and murine cells. Eur. J. Immunol. *46*, 2574–2586.

Lavin, Y., Winter, D., Blecher-Gonen, R., David, E., Keren-Shaul, H., Merad, M., Jung, S., and Amit, I. (2014). Tissue-resident macrophage enhancer landscapes are shaped by the local microenvironment. Cell *159*, 1312–1326.

Leber, J.H., Crimmins, G.T., Raghavan, S., Meyer-Morse, N.P., Cox, J.S., and Portnoy, D.A. (2008). Distinct TLR- and NLR-mediated transcriptional responses to an intracellular pathogen. PLoS Pathog. *4*, 0084–0095.

Lemaitre, B., Nicolas, E., Michaut, L., Reichhart, J.M., and Hoffmann, J.A. (1996). The dorsoventral regulatory gene cassette spatzle/Toll/Cactus controls the potent antifungal response in Drosophila adults. Cell *86*, 973–983.

Liao, Y., Smyth, G.K., and Shi, W. (2014). FeatureCounts: An efficient general purpose program for assigning sequence reads to genomic features. Bioinformatics *30*, 923–930.

Liberzon, A., Birger, C., Thorvaldsdóttir, H., Ghandi, M., Mesirov, J.P., and Tamayo, P. (2015). The Molecular Signatures Database Hallmark Gene Set Collection. Cell Syst. *1*, 417–425.

Lillebaek, T., Dirksen, A., Baess, I., Strunge, B., Thomsen, V., and Andersen, Å.B. (2002). Molecular evidence of endogenous reactivation of Mycobacterium tuberculosis after 33 years of latent infection. J. Infect. Dis. *185*, 401–404.

Lobet, E., Letesson, J.-J., and Arnould, T. (2015). Mitochondria: A target for bacteria. Biochem. Pharmacol. *94*, 173–185.

Loftus, R.M., and Finlay, D.K. (2016). Immunometabolism: Cellular metabolism turns immune regulator. J. Biol. Chem. *291*, 1–10.

Luo, W., and Brouwer, C. (2013). Pathview: An R/Bioconductor package for pathway-based data integration and visualization. Bioinformatics *29*, 1830–1831.

Manzanillo, P.S., Shiloh, M.U., Portnoy, D.A., and Cox, J.S. (2012). Mycobacterium tuberculosis activates the DNA-dependent cytosolic surveillance pathway within macrophages. Cell Host Microbe *11*, 469–480.

Marquis, J.-F., LaCourse, R., Ryan, L., North, R.J., and Gros, P. (2009). Disseminated and Rapidly Fatal Tuberculosis in Mice Bearing a Defective Allele at IFN Regulatory Factor 8. J. Immunol. *182*, 3008–3015.

McCarthy, D.J., Chen, Y., and Smyth, G.K. (2012). Differential expression analysis of multifactor RNA-Seq experiments with respect to biological variation. Nucleic Acids Res. *40*, 4288–4297.

McQuin, C., Goodman, A., Chernyshev, V., Kamentsky, L., Cimini, B.A., Karhohs, K.W., Doan, M., Ding, L., Rafelski, S.M., Thirstrup, D., et al. (2018). CellProfiler 3.0: Next-generation image processing for biology. PLoS Biol. *16*, e2005970.

Medzhitov, R. (2009). Approaching the Asymptote: 20 Years Later. Immunity *30*, 766–775.

Medzhitov, R., Preston-Hurlburt, P., and Janeway, C.A. (1997). A human homologue of the Drosophila toll protein signals activation of adaptive immunity. Nature *388*, 394–397.

Metchnikoff, E. (1893). Lectures in the Comparative Pathology of Inflammation.

Mills, E.L., Kelly, B., Logan, A., Costa, A.S.H., Varma, M., Bryant, C.E., Tourlomousis, P., Däbritz, J.H.M., Gottlieb, E., Latorre, I., et al. (2016). Succinate Dehydrogenase Supports Metabolic Repurposing of Mitochondria to Drive Inflammatory Macrophages. Cell *167*, 457-470.e13.

Mills, E.L., Kelly, B., and O'Neill, L.A.J. (2017). Mitochondria are the powerhouses of immunity. Nat. Immunol. *18*, 488–498.

Misharin, A. V., Morales-Nebreda, L., Mutlu, G.M., Budinger, G.R.S., and Perlman, H. (2013). Flow Cytometric Analysis of Macrophages and Dendritic Cell Subsets in the Mouse Lung. Am. J. Respir. Cell Mol. Biol. *49*, 503–510.

Moguche, A.O., Shafiani, S., Clemons, C., Larson, R.P., Dinh, C., Higdon, L.E., Cambier, C.J., Sissons, J.R., Gallegos, A.M., Fink, P.J., et al. (2015). ICOS and Bcl6-dependent pathways maintain a CD4 T cell population with memory-like properties during tuberculosis. J. Exp. Med. *212*, 715–728.

Moreira-Teixeira, L., Mayer-Barber, K., Sher, A., and O'Garra, A. (2018). Type I interferons in tuberculosis: Foe and occasionally friend. J. Exp. Med. *215*, 1273–1285.

Moreno-Altamirano, M.M.B., Paredes-González, I.S., Espitia, C., Santiago-Maldonado, M., Hernández-Pando, R., and Sánchez-García, F.J. (2012). Bioinformatic identification of Mycobacterium tuberculosis proteins likely to target host cell mitochondria: virulence factors? Microb. Inform. Exp. *2*, 9.

Mortaz, E., Adcock, I.M., Tabarsi, P., Masjedi, M.R., Mansouri, D., Velayati, A.A., Casanova, J.L., and Barnes, P.J. (2015). Interaction of Pattern Recognition Receptors with Mycobacterium Tuberculosis. J. Clin. Immunol. *35*, 1–10.

Nathan, C., and Cunningham-Bussel, A. (2013). Beyond oxidative stress: an immunologist's guide to reactive oxygen species. Nat. Rev. Immunol. *13*, 349–361.

Nemeth, J., Olson, G.S., Rothchild, A.C., Jahn, A.N., Mai, D., Duffy, F.J., Delahaye, J.L., Srivatsan, S., Plumlee, C.R., Urdahl, K.B., et al. (2020). Contained mycobacterium tuberculosis infection induces concomitant and heterologous protection. PLoS Pathog. *16*, e1008655.

Netea, M.G., Joosten, L.A.B., Latz, E., Mills, K.H.G., Natoli, G., Stunnenberg, H.G., O'Neill, L.A.J., Xavier, R.J., Medzhitov, R., Janeway, C., et al. (2016). Trained immunity: A program of innate immune memory in health and disease. Science *352*, aaf1098.

Newport, M.J., Huxley, C.M., Huston, S., Hawrylwicz, C.M., Oostra, B.A., Williamson, R., and Levin, M. (1996). A mutation in the interferon-γ-receptor gene and susceptibility to mycobacterial infection. N. Engl. J. Med. *335*, 1941–1949.

Neyrolles, O., Hernández-Pando, R., Pietri-Rouxel, F., Fornès, P., Tailleux, L., Payán, J.A.B., Pivert, E., Bordat, Y., Aguilar, D., Prévost, M.-C., et al. (2006). Is Adipose Tissue a Place for Mycobacterium tuberculosis Persistence? PLoS One *1*, e43.

North, R.J., and Jung, Y.-J. (2004). Immunity to Tuberculosis. Annu. Rev. Immunol. *22*, 599–623.

North, R.J., and Kirstein, D.P. (1977). T-cell-mediated concomitant immunity to syngeneic tumors. I. Activated macrophages as the expressors of nonspecific immunity to unrelated tumors and bacterial parasites. J. Exp. Med. *145*, 275–292.

O'Neill, L.A.J., and Pearce, E.J. (2016). Immunometabolism governs dendritic cell and macrophage function. J. Exp. Med. *213*, 15–23.

O'Neill, L.A.J., Kishton, R.J., and Rathmell, J. (2016). A guide to immunometabolism for immunologists. Nat. Rev. Immunol. *16*, 553–565.

Orme, I.M. (1988). Characteristics and specificity of acquired immunologic memory to Mycobacterium tuberculosis infection. J. Immunol. *140*, 3589–3593.

Overwijk, W.W., and Restifo, N.P. (2000). B16 as a Mouse Model for Human Melanoma. Curr. Protoc. Immunol. *39*, 20.1.1-20.1.29.

Pai, M., Behr, M.A., Dowdy, D., Dheda, K., Divangahi, M., Boehme, C.C., Ginsberg, A., Swaminathan, S., Spigelman, M., Getahun, H., et al. (2016). Tuberculosis. Nat. Rev. Dis. Prim. *2*, 16076.

Palmero, D.J., Eiguchi, K., Rendo, P., Castro Zorrilla, L., Abbate, E., and González Montaner, L.J. (1999). Phase II trial of recombinant interferon-α2b in patients with advanced intractable

multidrug-resistant pulmonary tuberculosis: Long-term follow-up. Int. J. Tuberc. Lung Dis. *3*, 214–218.

Pandey, A.K., Yang, Y., Jiang, Z., Fortune, S.M., Coulombe, F., Behr, M.A., Fitzgerald, K.A., Sassetti, C.M., and Kelliher, M.A. (2009). Nod2, Rip2 and Irf5 play a critical role in the type I interferon response to Mycobacterium tuberculosis. PLoS Pathog. *5*, 1000500.

Pantel, A., Teixeira, A., Haddad, E., Wood, E.G., Steinman, R.M., and Longhi, M.P. (2014). Direct Type I IFN but Not MDA5/TLR3 Activation of Dendritic Cells Is Required for Maturation and Metabolic Shift to Glycolysis after Poly IC Stimulation. PLoS Biol. *12*, e1001759.

Pearce, E.L., and Pearce, E.J. (2013). Metabolic pathways in immune cell activation and quiescence. Immunity *38*, 633–643.

Pisu, D., Huang, L., Grenier, J.K., and Russell, D.G. (2020). Dual RNA-Seq of Mtb-Infected Macrophages In Vivo Reveals Ontologically Distinct Host-Pathogen Interactions. Cell Rep. *30*, 335-350.e4.

Plumlee, C.R., Duffy, F.J., Gern, B.H., Delahaye, J.L., Cohen, S.B., Stoltzfus, C.R., Rustad, T.R., Hansen, S.G., Axthelm, M.K., Picker, L.J., et al. (2020). Ultra-low Dose Aerosol Infection of Mice with Mycobacterium tuberculosis More Closely Models Human Tuberculosis. Cell Host Microbe.

Poltorak, A., He, X., Smirnova, I., Liu, M.Y., Van Huffel, C., Du, X., Birdwell, D., Alejos, E., Silva, M., Galanos, C., et al. (1998). Defective LPS signaling in C3H/HeJ and C57BL/10ScCr mice: Mutations in Tlr4 gene. Science (80-. ). *282*, 2085–2088.

Rahman, M.A., Cumming, B.M., Addicott, K.W., Pacl, H.T., Russell, S.L., Nargan, K., Naidoo, T., Ramdial, P.K., Adamson, J.H., Wang, R., et al. (2020). Hydrogen sulfide dysregulates the immune response by suppressing central carbon metabolism to promote tuberculosis. Proc. Natl. Acad. Sci. U. S. A. *117*, 6663–6674.

Ravetch, J., and Aderem, A. (2007). Phagocytic cells. Immunol. Rev. *219*, 5–7.

Robinson, K.M., Janes, M.S., Pehar, M., Monette, J.S., Ross, M.F., Hagen, T.M., Murphy, M.P., and Beckman, J.S. (2006). Selective fluorescent imaging of superoxide in vivo using ethidium-based probes. Proc. Natl. Acad. Sci. U. S. A. *103*, 15038–15043.

Robinson, M.D., McCarthy, D.J., and Smyth, G.K. (2009). edgeR: A Bioconductor package for differential expression analysis of digital gene expression data. Bioinformatics *26*, 139–140.

Roca, F.J., and Ramakrishnan, L. (2013). TNF dually mediates resistance and susceptibility to mycobacteria via mitochondrial reactive oxygen species. Cell *153*, 521–534.

Roca, F.J., Whitworth, L.J., Redmond, S., and Jones, A.A. (2019). TNF Induces Pathogenic Programmed Macrophage Necrosis in Tuberculosis through a Mitochondrial-Lysosomal-Endoplasmic Reticulum Circuit. Cell *178*.

Rose, S., Misharin, A., and Perlman, H. (2012). A novel Ly6C/Ly6G-based strategy to analyze the mouse splenic myeloid compartment. Cytom. Part A *81A*, 343–350.

Ross-Innes, C.S., Stark, R., Teschendorff, A.E., Holmes, K.A., Ali, H.R., Dunning, M.J., Brown, G.D., Gojis, O., Ellis, I.O., Green, A.R., et al. (2012). Differential oestrogen receptor binding is associated with clinical outcome in breast cancer. Nature *481*, 389–393.

Rothchild, A., Mai, D., Aderem, A., and Diercks, A. (2020). Flow Cytometry Analysis and

Fluorescence-activated Cell Sorting of Myeloid Cells from Lung and Bronchoalveolar Lavage Samples from Mycobacterium tuberculosis-infected Mice. BIO-PROTOCOL *10*.

Rothchild, A.C., Olson, G.S., Nemeth, J., Amon, L.M., Mai, D., Gold, E.S., Diercks, A.H., and Aderem, A. (2019). Alveolar macrophages generate a noncanonical NRF2-driven transcriptional response to Mycobacterium tuberculosis in vivo. Sci. Immunol. *4*.

Russell, D.G., Huang, L., and VanderVen, B.C. (2019). Immunometabolism at the interface between macrophages and pathogens. Nat. Rev. Immunol. *19*, 291–304.

Saljoughian, N., Taheri, T., and Rafati, S. (2014). Live vaccination tactics: Possible approaches for controlling visceral leishmaniasis. Front. Immunol. *5*, 134.

Sanlorenzo, M., Vujic, I., Carnevale-Schianca, F., Quaglino, P., Gammaitoni, L., Fierro, M.T., Aglietta, M., and Sangiolo, D. (2017). Role of interferon in melanoma: old hopes and new perspectives. Expert Opin. Biol. Ther. *17*, 475–483.

Sathkumara, H.D., Pai, S., De Jesús Aceves-Sánchez, M., Ketheesan, N., Flores-Valdez, M.A., and Kupz, A. (2019). BCG vaccination prevents reactivation of latent lymphatic murine tuberculosis independently of CD4+ T cells. Front. Immunol. *10*, 532.

Schindelin, J., Arganda-Carreras, I., Frise, E., Kaynig, V., Longair, M., Pietzsch, T., Preibisch, S., Rueden, C., Saalfeld, S., Schmid, B., et al. (2012). Fiji: An open-source platform for biological-image analysis. Nat. Methods *9*, 676–682.

Schneider, D.S., and Ayres, J.S. (2008). Two ways to survive infection: what resistance and tolerance can teach us about treating infectious diseases. Nat. Rev. Immunol. *8*, 889–895.

Sena, L.A., and Chandel, N.S. (2012). Physiological Roles of Mitochondrial Reactive Oxygen Species. Mol. Cell *48*, 158–167.

Shadel, G.S., and Horvath, T.L. (2015). Mitochondrial ROS Signaling in Organismal Homeostasis. Cell *163*, 560–569.

Shafiani, S., Tucker-Heard, G., Kariyone, A., Takatsu, K., and Urdahl, K.B. (2010). Pathogen-specific regulatory T cells delay the arrival of effector T cells in the lung during early tuberculosis. J. Exp. Med. *207*, 1409–1420.

Sheedy, F.J., and Divangahi, M. (2020). Targeting immunometabolism in host defence against Mycobacterium tuberculosis. Immunology *Oct 6 2020*, doi: 10.1111/imm.13276.

Shi, C., and Pamer, E.G. (2011). Monocyte recruitment during infection and inflammation. Nat. Rev. Immunol. *11*, 762–774.

Shin, D.M., Jeon, B.Y., Lee, H.M., Jin, H.S., Yuk, J.M., Song, C.H., Lee, S.H., Lee, Z.W., Cho, S.N., Kim, J.M., et al. (2010). Mycobacterium tuberculosis eis regulates autophagy, inflammation, and cell death through redox-dependent signaling. PLoS Pathog. *6*, e1001230.

Sohn, H., Kim, J.S., Shin, S.J., Kim, K., Won, C.J., Kim, W.S., Min, K.N., Choi, H.G., Lee, J.C., Park, J.K., et al. (2011). Targeting of Mycobacterium tuberculosis heparin-binding hemagglutinin to mitochondria in macrophages. PLoS Pathog. *7*, e1002435.

Soto, M.J., Domínguez-Ferreras, A., Pérez-Mendoza, D., Sanjuán, J., and Olivares, J. (2009). Mutualism versus pathogenesis: The give-and-take in plant-bacteria interactions. Cell. Microbiol. *11*, 381–388.

Subramanian, A., Tamayo, P., Mootha, V.K., Mukherjee, S., Ebert, B.L., Gillette, M.A.,

Paulovich, A., Pomeroy, S.L., Golub, T.R., Lander, E.S., et al. (2005). Gene set enrichment analysis: A knowledge-based approach for interpreting genome-wide expression profiles. Proc. Natl. Acad. Sci. U. S. A. *102*, 15545–15550.

van Teijlingen Bakker, N., and Pearce, E.J. (2020). Cell-intrinsic metabolic regulation of mononuclear phagocyte activation: Findings from the tip of the iceberg. Immunol. Rev. *295*, 54–67.

Thaiss, C.A., Zmora, N., Levy, M., and Elinav, E. (2016). The microbiome and innate immunity. Nature *535*, 65–74.

Tornack, J., Reece, S.T., Bauer, W.M., Vogelzang, A., Bandermann, S., Zedler, U., Stingl, G., Kaufmann, S.H.E., and Melchers, F. (2017). Human and mouse hematopoietic stem cells are a depot for dormant mycobacterium tuberculosis. PLoS One *12*, e0169119.

Troegeler, A., Mercier, I., Cougoule, C., Pietretti, D., Colom, A., Duval, C., Vu Manh, T.-P., Capilla, F., Poincloux, R., Pingris, K., et al. (2017). C-type lectin receptor DCIR modulates immunity to tuberculosis by sustaining type I interferon signaling in dendritic cells. Proc. Natl. Acad. Sci. *114*, E540–E549.

Usher, N.T., Chang, S., Howard, R.S., Martinez, A., Harrison, L.H., Santosham, M., and Aronson, N.E. (2019). Association of BCG Vaccination in Childhood With Subsequent Cancer Diagnoses: A 60-Year Follow-up of a Clinical Trial. JAMA Netw. Open *2*, e1912014.

Vance, R.E., Isberg, R.R., and Portnoy, D.A. (2009). Patterns of Pathogenesis: Discrimination of Pathogenic and Nonpathogenic Microbes by the Innate Immune System. Cell Host Microbe *6*, 10–21.

Vankayalapati, R., Wizel, B., Weis, S.E., Klucar, P., Shams, H., Samten, B., and Barnes, P.F. (2003). Serum cytokine concentrations do not parallel Mycobacterium tuberculosis - Induced cytokine production in patients with tuberculosis. Clin. Infect. Dis. *36*, 24–28.

Wang, C. (1916). An experimental study of latent Tuberculosis. Lancet *188*, 417–419.

Wassermann, R., Gulen, M.F., Sala, C., Perin, S.G., Lou, Y., Rybniker, J., Schmid-Burgk, J.L., Schmidt, T., Hornung, V., Cole, S.T., et al. (2015). Mycobacterium tuberculosis Differentially Activates cGAS- and Inflammasome-Dependent Intracellular Immune Responses through ESX-1. Cell Host Microbe *17*, 799–810.

Watson, R.O., Bell, S.L., MacDuff, D.A., Kimmey, J.M., Diner, E.J., Olivas, J., Vance, R.E., Stallings, C.L., Virgin, H.W., and Cox, J.S. (2015). The Cytosolic Sensor cGAS Detects Mycobacterium tuberculosis DNA to Induce Type I Interferons and Activate Autophagy. Cell Host Microbe *17*, 811–819.

Weinberg, S.E., Sena, L.A., and Chandel, N.S. (2015). Mitochondria in the regulation of innate and adaptive immunity. Immunity *42*, 406–417.

Weindel, C.G., Bell, S.L., Vail, K.J., West, K.O., Patrick, K.L., and Watson, R.O. (2020). LRRK2 maintains mitochondrial homeostasis and regulates innate immune responses to Mycobacterium tuberculosis. Elife *9*.

West, A.P., Brodsky, I.E., Rahner, C., Woo, D.K., Erdjument-Bromage, H., Tempst, P., Walsh, M.C., Choi, Y., Shadel, G.S., and Ghosh, S. (2011). TLR signalling augments macrophage bactericidal activity through mitochondrial ROS. Nature *472*, 476–480.

West, A.P., Khoury-Hanold, W., Staron, M., Tal, M.C., Pineda, C.M., Lang, S.M., Bestwick, M.,

Duguay, B.A., Raimundo, N., MacDuff, D.A., et al. (2015). Mitochondrial DNA stress primes the antiviral innate immune response. Nature *520*, 553–557.

Wiens, K.E., and Ernst, J.D. (2016). The Mechanism for Type I Interferon Induction by Mycobacterium tuberculosis is Bacterial Strain-Dependent. PLoS Pathog. *12*, e1005809.

Wilson, L.G. (2005). Commentary: Medicine, population, and tuberculosis. Int. J. Epidemiol. *34*, 521–524.

World Health Organization (2020). Global Tuberculosis Report 2020 (Geneva).

Wu, T.D., and Nacu, S. (2010). Fast and SNP-tolerant detection of complex variants and splicing in short reads. Bioinformatics *26*, 873–881.

Wu, T.D., and Watanabe, C.K. (2005). GMAP: A genomic mapping and alignment program for mRNA and EST sequences. Bioinformatics *21*, 1859–1875.

Wu, D., Lim, E., Vaillant, F., Asselin-Labat, M.L., Visvader, J.E., and Smyth, G.K. (2010). ROAST: Rotation gene set tests for complex microarray experiments. Bioinformatics *26*, 2176–2182.

Wu, D., Sanin, D.E., Everts, B., Chen, Q., Qiu, J., Buck, M.D., Patterson, A., Smith, A.M., Chang, C.H., Liu, Z., et al. (2016). Type 1 Interferons Induce Changes in Core Metabolism that Are Critical for Immune Function. Immunity *44*, 1325–1336.

York, A.G., Williams, K.J., Argus, J.P., Zhou, Q.D., Brar, G., Vergnes, L., Gray, E.E., Zhen, A., Wu, N.C., Yamada, D.H., et al. (2015). Limiting Cholesterol Biosynthetic Flux Spontaneously Engages Type I IFN Signaling. Cell *163*, 1716–1729.

Zak, D.E., Penn-Nicholson, A., Scriba, T.J., Thompson, E., Suliman, S., Amon, L.M., Mahomed, H., Erasmus, M., Whatney, W., Hussey, G.D., et al. (2016). A blood RNA signature for tuberculosis disease risk: a prospective cohort study. Lancet *387*, 2312–2322.

Zhang, L., Jiang, X., Pfau, D., Ling, Y., and Nathan, C.F. (2021). Type I interferon signaling mediates Mycobacterium tuberculosis-induced macrophage death. J. Exp. Med. *218*.

Zhang, Q., Liu, Z., Moncada-Velez, M., Chen, J., Ogishi, M., Bigio, B., Yang, R., Arias, A.A., Zhou, Q., Han, J.E., et al. (2020). Inborn errors of type I IFN immunity in patients with life-threatening COVID-19. Science (80-. ). *370*.

Zhang, Y., Liu, T., Meyer, C.A., Eeckhoute, J., Johnson, D.S., Bernstein, B.E., Nussbaum, C., Myers, R.M., Brown, M., Li, W., et al. (2008). Model-based analysis of ChIP-Seq (MACS). Genome Biol. *9*, R137.

Zhou, R., Yazdi, A., Menu, P., and Tschopp, J. (2011). A role for mitochondria in NLRP3 inflammasome activation. Nature *469*, 221–225.

Zug, R., and Hammerstein, P. (2015). Wolbachia and the insect immune system: What reactive oxygen species can tell us about the mechanisms of Wolbachia-host interactions. Front. Microbiol. *6*, 1–16.